Okinawa Institute of Science and Technology

Graduate University

Thesis submitted for the degree

Doctor of Philosophy

Two-Photon Voltage Imaging of Supragranular

Barrel Cortex in Mice: Oscillations and Responses

by

Neil Dalphin

Supervisor **Professor Bernd Kuhn**

Submitted **September 2019**

I, Neil Dalphin, declare that this thesis entitled "Two-Photon Voltage Imaging of Supragranular Barrel Cortex in Mice: Oscillations and Responses" and the data presented in it are original and my own work.

I confirm that:

- No part of this work has previously been submitted for a degree at this or any other university.

- References to the work of others have been clearly acknowledged. Quotations from the work of others have been clearly indicate, and attributed to them.

- In cases where others have contributed to part of this work, such contribution has been clearly acknowledged and distinguished from my own work.

- None of this work has been previously published elsewhere.

Signature:

Date: 18/09/2019

Abstract

The supragranular layers of cortex are key information integration and computation areas with dominant cortico-cortical connections. While layers 2 and 3 are densely packed with somata, layer 1 is almost free of somata. The absence of somata makes the analysis of layer 1 difficult. Electrical recording from small processes within layer 1 are not possible and electric field recordings are difficult due to the low seal resistance. Imaging processes of layer 1 remains difficult as cells project into it from many distant areas and due to the dense and intermingled packing.

Here, I record sensory signals in supragranular layers, including layer 1 through a combination of voltage sensitive dye imaging, and an intracellular calcium indicator. Optical sectioning with two-photon microscopy allowed resolution in depth, showing changes in the sensory signal within layer 1. Additionally, cortical oscillations were detected with the voltage-sensitive dye in the delta, theta, and beta bands, and, for the first time with voltage imaging, also in the slow-gamma (35 Hz) band, *in vivo*. Delta, theta, and gamma oscillations were modulated by sensory stimuli.

As very little is known about membrane voltage oscillations in layer 1 and to optimize optical voltage recordings in layer 1, I developed a novel surgery to apply voltage dye primarily to layer 1, without removing the dura or injecting dye within the brain. I also applied a new voltage-sensitive dye optimized for tissue diffusion with this surgery. I imaged cortical membrane potential oscillations with two-photon microscopy depth-resolved (25 to 100 μm below dura) in anesthetized and awake mice. Again, I found delta (0.5-4 Hz), theta (4-10 Hz), low beta (10-20 Hz), and low gamma (30-40 Hz) oscillations. All oscillation bands were stronger in awake animals. While the power of delta, theta, and low beta oscillations increased with depth, the power of low gamma was more constant throughout layer 1. These findings identify layer 1 as an important coordination hub for the dynamic binding process of neurons mediated by oscillations.

Acknowledgments

I would like to acknowledge the following people and groups for the help they provided me in creating and completing this thesis.

Professor Bernd Kuhn for supervising this work, providing the equipment that all the data was collected with, and helping to design all the research within. None of this would have been possible without this guidance and help. Also the other members of my thesis committee, Professors Erik De Schutter and Gordon Arbuthnott for their time taken to provide feedback on this work. Dr. Claudia Cecchetto and Dr. Kazuo Mori both read and proofed earlier versions of this thesis, and their time and effort was very much appreciated.

For work provided, Dr. Eugene Khaskin for synthesizing di1-ANNINE-6plus, a new voltage dye perfect for layer 1 imaging. Soumen Jana for growing cells and for taking the time to record them with me. It was tedious, but it worked eventually. Finally, Dr. Kazuo Mori, for keeping me well stocked in micropipettes. I used a lot of them, but he always kept up.

The OIST graduate school, and graduate school staff for supporting me through my studies. This journey here would have been impossible for me without the support provided by dedicated workers within the graduate school. Finally, the Japanese government and Japanese taxpayers for providing me with funding and facilities to work in.

As a last acknowledgement, I would like to thank the friends, family, and lab members who have supported me while I complete my studies. It is difficult for me to put into words how much so many of you have meant to me –anything I write here feels inadequate. Please know, you, and your support mean a great deal to me.

List of Abbreviations

AMPA   - α-animo-3-hydroxy-5-methyl-4-isoxazolepionic acid receptor

EPSP   - Excitatory post-synaptic potential

GABA   - gamma-aminobutyric acid

HEK   - Human embryonic kidney cells

Hz   - Hertz

LFP   - Local field potential

mV   - millivolts

NMDA   - N-methyl-D-aspartate receptor

PBS   - Phosphate buffer solution

PoM   - Posteromedial complex of the thalamus

S1   - Primary somatosensory area of the cortex

VPM   - Ventral posteromedial nucleus of the thalamus

VSD   - Voltage sensitive dye

Table of Contents   **Page**

List of Figures

Tables

General Introduction

The mammalian cortex is a highly developed structure in the brain. It performs complex massively simultaneous tasks involving all senses, motion control, and the integration of them with internally generated states. Modern neuroscience aims (among other things) to understand and unwind the complexity of cortical processing. In order to do so, we must work with the known anatomy, and physiology, to create a unified theory of cortical function. Of particular interest to me is the theorized integration zone of the cortex – cortical layer 1. Here, various parts of local and distant cortex meet, combining signals, and generating new outputs. However, in studying cortical layer 1, and the supragranular areas in general, we are limited not just in the complexity of the cortex as a whole, but also in the techniques which we use to probe it. Slices, both acute and fixed, have their places in neurophysiology, but are dealing with a fundamentally

Figure 1.1. Canonical microcircuit diagram, taken from da Costa and Martin, 2010 (da Costa and Martin, 2010), figure 5 (creative commons license). Arrows indicate excitatory connections and ball ends indicate inhibitory connections. L stands for layer (Layer 1 is not included in their model), Thal for thalamus, and sub for sub-cortical nuclei.

changed system from what occurs in an intact brain. Studying an integration area like cortical layer 1 in slices means missing some of the integrated input. We face the problem that the brain activity we wish to understand and record, arises from behaviors being undertaken, and the world being experienced. As such, the closer to non-invasive measurements we can get, the more accurate our measurements will become. It is with this in mind, that I undertook

this project, to investigate in high resolution, supragranular cortical activity, especially of cortical layer 1, in intact, alive, and healthy brains.

Cortical Anatomy

To understand cortical function it is important to review cortical anatomy. Much research focuses on a particular region of cortex, but in terms of anatomy it is appropriate to some extent to generalize from one region to another (da Costa and Martin, 2010).

Although there is some debate as to whether the cortex should be thought of as forming vertical columns of connectivity and functionality, there is no doubt that in the mammalian nervous systems the cortex is organized functionally and anatomically into layers (da Costa and Martin, 2010). Rodents do not feature the cortical columnar structure found in cats and primates, however mice and rats do form vertically organized 'barrels' in an area of the somatosensory cortex, (Woolsey and Van der Loos, 1970; Lubke and Feldmeyer, 2007; da Costa and Martin, 2010). Barrels are appealing because they create local circuits anatomically and physiologically constrained, and also resemble in some ways the cortical columns found in larger mammalian brains.

da Costa and Martin (da Costa and Martin, 2010) present the canonical microcircuit (an older idea in neuroscience (Douglas et al., 1989)) of the cortex as organized in layers of increasing depth (layers 1 to 6 respectively). In the canonical microcircuit, neurons make column like structures, with generalized inputs from the thalamus and other cortical areas. Horizontal connections are included so that one stack can be connected to adjacent stacks (proposed circuit shown in Fig. 1.1). This model is beneficial to the brain because anatomical wiring during neural growth becomes much easier if there is a generalized wiring, rather than a complex and unique wiring for each brain region.

Looking at the cellular distribution of neurons within a sensory cortex can shed some insight onto the function of the layers. Gabbot and Somogyi in 1986 (Gabbott and Somogyi, 1986) performed a thorough investigation of cell soma location in cat visual cortex. Using immuno-labeling for glutamate decarboxylase, an enzyme found primarily in neurons signaling with GABA (gamma-aminobutyric acid), combined with toluidine blue labeling (staining all
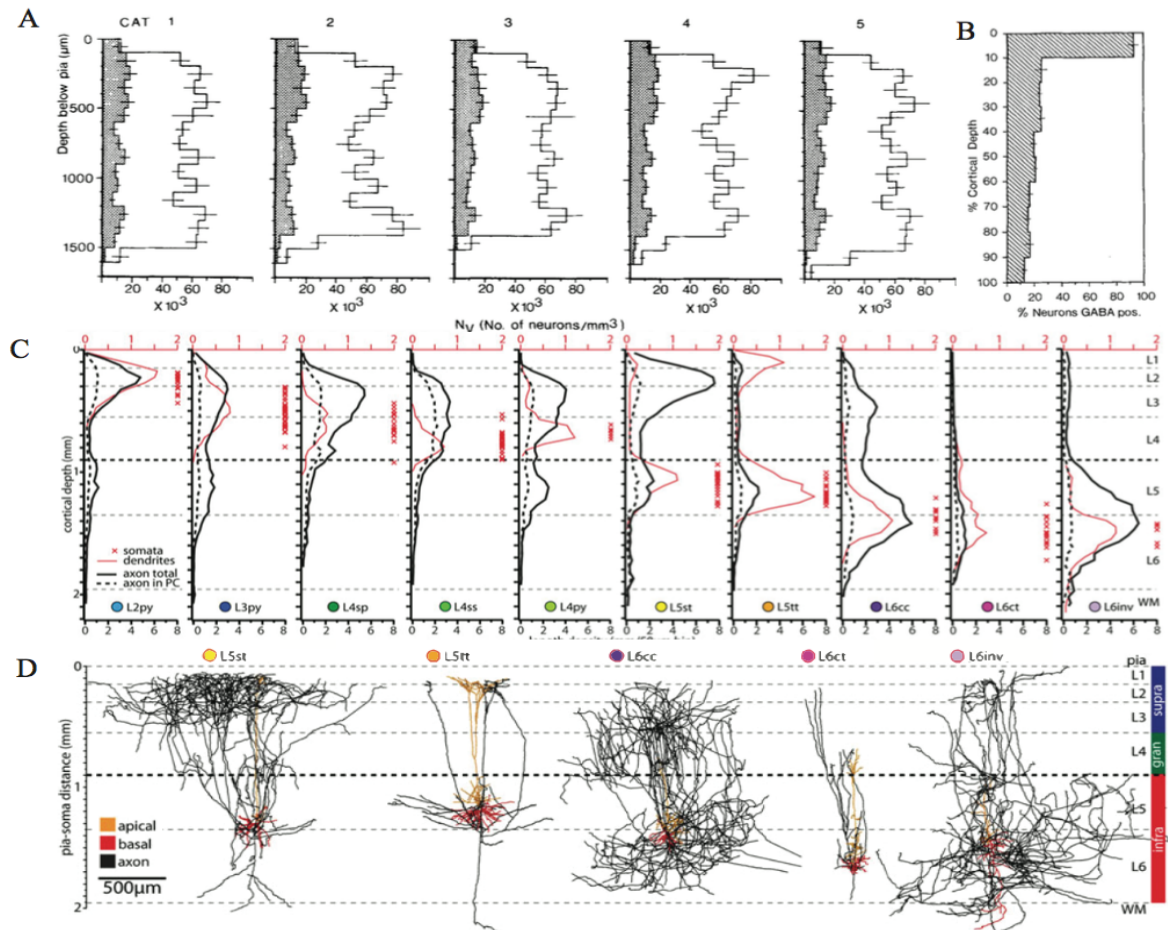
Figure 1.2. **A** and **B** Neuron densities at various layers in the cat visual cortex. Figures adapted from (Gabbott and Somogyi, 1986), figure 4 and figure 5 (reprinted with permission, Springer Nature). **C** and **D** excitatory neuron projections at various depths in rat barrel cortex, figures adapted from (Narayanan et al., 2015), figures 3 and 4 (reprinted with permission, Oxford University Press). **A** Cell counts in one cat's visual cortex for each 100μm of depth (cortex in cats going from 0 to approximately 1500μm). Dark color refers to GABAergic cells and uncolored refers to non-GABAergic cells. Numbers of each cell type are presented. **B** Average percentage of neurons stained GABAergic, of the total population of neurons at each cortical depth (expressed as a percentage of cortical depth, with 0 being the upper surface and 100% being the deep edge of the cortex). **C** Average density of axonal (black), axon in principle barrel column (dashed black) and dendrites (red) for each excitatory cell type, for each cortical depth. Red crosses designate where the cell soma was found. Layers are expressed on the right, with L. **D** Exemplary cell morphologies for excitatory cell types below layer IV. Axons are drawn in black, apical dendrites in orange and basal dendrites in red. Abbreviations as follow: L refers to layer, py - pyramidal cell, sp - star-pyramidal cell, ss – spiny stellate cell, st – slender tufted pyramidal cell, tt – thick tufted pyramidal cell, ct – corticothalamic pyramidal cell, cc – corticocortical pyramidal cell, inv – inverted pyramidal cell.

neuron cell bodies) they stereologically counted the number of cells in each layer of their chosen sections, and the number of those cells that were GABAergic.

 These numbers were used to come up with a density of cells in each layer and the proportion of which are GABAergic. During this, the cell body shape and size were catalogued, thoroughly characterizing the cells bodies of this cortex. They found that cell body size increases with depth, especially the GABAergic cells. Non-GABAergic cells were almost certainly glutamatergic, and the largest of these were found in layer 5. The cell morphology showed non-GABAergic cells were pyramidal in shape in layers 2, 3 and 5 – following

previous anatomical work describing cells in the cortex (Elston, 2003). The GABAergic cells found were more circular with radial dendritic trees, and were found to be the minority of cells, with about one GABAergic cell to four non-GABAergic cells.

Layer 1 has the highest percentage of cells labeled GABAergic (shown in Fig. 1.2b). Although the total number of GABAergic cells present is lower than other cortical layers, the almost complete lack of non-GABAergic cells greatly raises the proportion of GABAergic cells from the total number of cells. Delving deeper into the cortical GABAergic neurons, Rudy et al (Rudy et al., 2011) studied their genetic breakdown. Three broad groups were created – parvalbumin expressing, somatostain expressing, and vasoactive intestinal peptide expressing (as a subset of 5HT3a receptor expressing), with seemingly no overlap between them. These populations changed with cortical depth, something confirmed by Jiang et al (Jiang et al., 2015), with genetically targeted cell patching and filling. Together these pieces of research show no fast-spiking parvalbumin interneurons in layer 1, but then in each layer deeper between ¼ and ½ of all GABAergic cells were fast-spiking parvalbumin expressing interneurons. The interneurons of layer 1 fell into two morphologies – the horizontally projecting elongated neuroglioform cells, and the single-bouquet like cells, with axons reaching into layer 2/3, as well as some occasional layer 2 connecting dendrites. Other interneurons from deeper layers connected strongly into layer 1, notably the Marionotti cells of layer 5 and 2/3, the bi-tufted cells of layer 2/3, bi-polar cells from layer 2/3, and the double-bouquet cells from layer 2/3. None of these were believed to be fast-spiking parvalbumin expressing interneurons. All the fast-spiking parvalbumin expressing interneurons focused mainly within their cortical layer, although some basket cells appear to project into layer 1.

Completing the cyto-architecture of the cortex, Narayanan et al (Narayanan et al., 2015) filled and 3D reconstructed excitatory cells from all layers of barrel cortex in rats. Their work consisted of 153 neurons reconstructed and studied, with focus on their axonal and dendritic projections. The primary findings were that each cell type has a characteristic branching across layers (Fig. 1.2c) and even across barrels. Axons of layer 4 stellate cells in particular often left their principle barrel and were found to touch sometimes more than 10 neighboring barrels, in an asymmetric pattern. Some characteristic cell morphologies are shown in figure. 1.2d, showing the distribution of axons and dendrites over cortical depth, for the layer 5 and 6 cells. This impressive work also characterized the axonal and dendritic spread at various cortical depths for each excitatory neuronal subtype (Fig. 1.2c).

Barrel Cortex
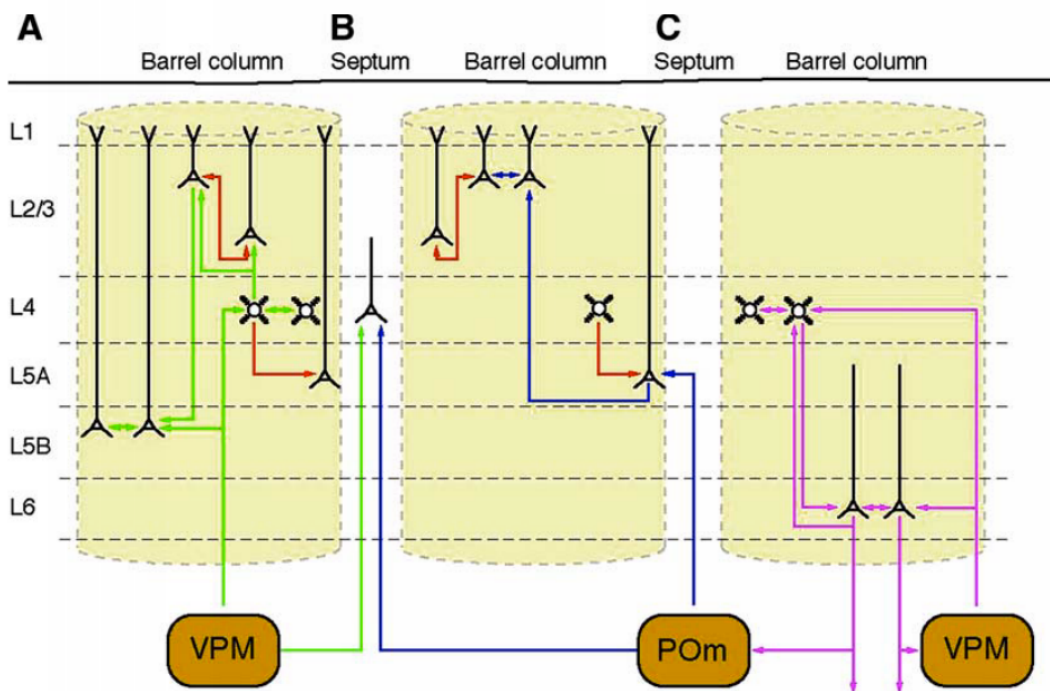
Figure 1.3. Lemniscal and paralemniscal pathway wiring diagram. Cells are shown in black, green projections show the lemniscal pathway, red shows intracortical circuits between the lemniscal and paralemniscal routes, blue shows the paralemniscal path and magenta is the thalamocortical loop. **A** shows the direct pathway from primary thalamus. **B** The secondary thalamus provides paralemniscal input into barrel cortex. **C** Describes the corticothalamic loop. Image taken from (Lubke and Feldmeyer, 2007), figure 8 (with permission, Springer Nature).

The barrel cortex is the primary sensory area for whisker touch in whisking rodents (Woolsey and Van der Loos, 1970; Lubke and Feldmeyer, 2007; Fox, 2008). The barrels that categorize this region are anatomical features of cortical layer 4 stellate cells, forming columns. Each barrel responds preferentially to a particular whisker on the animal's face. These barrels are organized in a topographic manner across this cortical area. The neurons are mainly excitatory neurons, made up of pyramidal and stellate cells, with the rest of the neurons being GABAergic interneurons (Narayanan et al., 2017). Also in barrel cortex six layers of cyto-architecture are defined, with Layer 1 being mostly neuropil, pyramidal neurons are primarily found in layer 2/3, 5 and 6, and spiny stellate cells in Layer 4. Pyramidal cells are the primary output of the cortex in general and barrel cortex is no exception.

Input to Barrel Cortex

Information of whisker touch originates in pressure sensing nerve endings in the whisker follicles. It passes to the trigeminal nuclei in the brainstem where it crosses over to the contralateral side of the brain, and then finds the thalamus (Diamond et al., 2008). The direct inputs to the barrel cortex are these thalamic nuclei. Starting from the whisker follicle, information is already split into three pathways that remain somewhat separate, all the way to the cortex. These are the lemniscal, and extralemniscal paths going through the ventral posterior nucleus of the thalamus (VPM) and the paralemniscal path going through the posteromedial complex of the thalamus (PoM), into the barrel cortex. The VPM connects most strongly to spiny stellate cells in layer 4, but also sends efferents to layers 3 and part of 5 and 6. These connections to Layer 4 are numerous but particularly weak (Bruno and Sakmann, 2006). Despite this they are still the main driving force behind Layer 4 excitation. This suggests that input to Layer 4 must be synchronous and massive, which is what would be expected when a whisker is manipulated. The PoM meanwhile projects mainly to layer 5, but in a separate part from where the VPM connects, plus has some additional connections to layer 1, where it connects to many cell types, including layer 2/3 pyramidal cells (Casas-Torremocha et al., 2019). Looking the opposite way and staining cells retrogradely from the primary somatosensory cortex, layer 1, it was found that PoM and primary motor cortex were the most significant contributors of input (Herkenham, 1980). Layer 4 stellate cells tend to project upwards to layer 2/3 where they excite the pyramidal cells, and unlike the rest of the

cortex, this connection seems to be one-directional. A simplified diagram of wiring in the lemniscal and paralemniscal pathway is shown in Figure. 1.3. This diagram certainly does not cover the entire pathway, as outputs from the cortex go to many places in the brain, but this sketch shows concise connections between cells in various layers and nuclei, and importantly how neighboring barrels interact.

Figure 1.4. **A** Thalamo-cortical projection neurons and the thalamic nuclei they originate from. RT refers to reticular thalamus and the numbers on the right of the image are cortical layers. **B** Typical morphology of an M-type thalamocortical cell. **C** Distribution of cell types (IL, M multiareal, M focal and C type), in the various thalamic nuclei. Nuclei names mentioned elsewhere in this text: VPM, ventroposterior medial thalamic nucleus, and Po, posterior thalamus (I refer to PoM, or posterior medial nucleus thalamus) Figure taken from (Clascá et al., 2012), figure 1 (with permission, John Wiley and Sons).

There have been suggestions that paralemniscal vs lemniscal paths divide the cortex into two functional microcircuits, although reciprocal wiring keeps both pathways intimately connected. The cortex forms many loops of connectivity and thus the thalamus excites the barrel cortex and the cortex feeds back to the thalamus through Layer 6 pyramidal neurons (shown in Fig. 1.3) - (Shepherd, 2003; Lubke and Feldmeyer, 2007).

Barrel Cortex Physiology

Work by Constantinople and Bruno (Constantinople and Bruno, 2013) has shown that the connections from the thalamus to the barrel cortex are not as simple as previously thought. At the time of the review by Lübke and Feldmeyer (Lubke and Feldmeyer, 2007), it was believed that the lemniscal input projected only to layer 4, which in turn excited layer 2/3 and then moved to Layer 5

and 6, in serial order. By comparing latencies of whisker responses, paired recordings of thalamic and neurons of layers 5 and 6, and drug inactivation of layer 4, Constantinople and Bruno (Constantinople and Bruno, 2013) were able to conclusively show that whisker evoked responses do not go in a serial path. It seems that Layer 5 and 6 receive their own input from the thalamus, as shown by paired recordings where thalamic stimulation excited about a quarter of the Layer 5 neurons they found, but only one percent of the Layer 6 cells. Excitation of Layer 5 from whisker stimulation arrives either slightly earlier, or perhaps simultaneously with the input to layer 4, while Layer 6 is excited simultaneously with layer 2/3. The Layer 4 signal still travels to layer 2/3, which does synapse with layers 5 and 6, but this connection seems not to be for bottom-up signaling, but more for a comparison between the signals. To investigate the spread of thalamic projections to the cortex Rubio-Garrido et al (Rubio-Garrido et al., 2009) laid fast-blue dye (a retrograde tracer) over Layer 1 of rat somatosensory cortices including adjacent areas. Cells were traced back to Layer 5 and 6, but more interestingly, a huge amount of cells were traced back to many nuclei of the thalamus. Even when reducing the tracer amount and restricting its spread to a small region, the tracing still showed multiple nuclei, from a vast range of functions. Motor and sensory nuclei project and converge in narrow areas of the somatosensory cortex, seemingly on the apical tufts of the Layer 5 neurons. Figure. 1.4 shows the known classes of thalamo-cortical projecting neurons, from the thalamic nuclei they depart from and the cortical layers they arrive in. This emphasizes how important direct thalamic input is to many cortical areas, through layer 1 inputs.

While Layer 5 neurons are considered the primary output of all cortical areas and Layer 6 form the corticothalamic feedback loop (Lubke and Feldmeyer, 2007; da Costa and Martin, 2010; Constantinople and Bruno, 2013) Layer 5 neurons also show massive interconnectivity with the rest of the cortical layers, through layer 1. Cauller, Clancy and Connors (Cauller et al., 1998) performed cell tracing from Layer 1 of the primary barrel cortex. They found huge horizontal fibers coursing through the neuropil for longer than 1 mm, which is a very long distance in the rat brain. Known targets for cells in the primary somatosensory cortex are the secondary somatosensory cortex and the primary motor cortex, but they also found long axons projecting backwards to the Layer 1 neuropil from these regions. Also shown was the massive extent to which Layer 1 receives input from layer 5. It has even been estimated that

cortico-cortical connections are the main form of cortical input, making up between 99% and 99.9% of all fibers connecting to the cortex (Shepherd, 2003). Together their results illustrate the interconnectedness of the neocortex, with its canonical microcircuits.

This is interesting given the findings of Larkum, Senn and Lüscher (Larkum et al., 2004) who performed patch clamp experiments on Layer 5 pyramidal cells, looking at their responses based on excitation from Layer 1 input (to their distal tufts). What they found was input to the tuft is very weak, as expected and modeled by a passive conductance going from the very fine and distant distal tufts and transmitting to the deep cell body.

If the apical dendrite brings the cell above threshold and it fires an action potential, it also generates a back propagating action potential, which travels up the distal dendrite and depolarizes the tuft. While the tuft is depolarized (time window of about 20-30 ms), input to the tuft is reliably translated into action potentials, and especially into bursts of action potentials. This is a different mode of activity for these neurons, which under other stimulation procedures tend not to burst. Given the inputs found by Rubio-Garrido et al (Rubio-Garrido et al., 2009), this could represent a convergence of information on the Layer 5 neuron, but only when the neuron has just fired from bottom-up stimulation (for example, whisker stimulation). Coincidence detection like this, in pyramidal neurons is believed to be a key computation these cells perform. Previous research showed that N-methyl-D-aspartate-receptor (NMDA) receptors in dendritic tufts work in concert with α-animo-3-hydroxy-5-methly-4-isoxazolepropionic acid (AMPA) receptors to produce large scale calcium spikes in the neuron. Simple excitation of the dendrite by glutamate produces small calcium events, by triggering voltage gated calcium channels, after triggering AMPA receptors. When an action-potential is triggered within the cell however, and glutamate also released, then NMDA channels open, generating the large calcium spike (Schiller et al., 1998). A large NMDA triggered somatic spike massively amplifies the somatic voltage response, and these NMDA spikes can be triggered by repetitive, concurrent AMPA triggered spikelets (Schiller et al., 2000). Together, these studies point to pyramidal cells preferentially amplifying signals where coincidence between inputs has been detected, and paints a picture of the cortex performing signal integration across all its layers.

Recent work from Zhang and Bruno (Zhang and Bruno, 2019) suggests that cortical inputs to barrel cortex are weaker than the secondary thalamic inputs from the POm. Channel-rhodopsin was expressed in primary motor cortex, secondary somatosensory cortex, and the POm, so stimulation could be done *in vivo*. Whole-cell electrical recordings were made on layer 2/3 pyramidal cells, while excitation light for the channel rhodopsin shone through the cranial window, exciting fibers in the area of the electrical recording. While the animals were under general anesthesia, POm fiber activation resulted in a much larger response than fiber activation from either cortical source. Additionally, when combined with simultaneous whisker stimulation, the POm fiber activation produced supra-linear potentials in the layer 2/3 cell, while whisker stimulation combined with cortical fiber input did not. This large depolarization due to POm stimulation seemed to stay intact during wakefulness, as recorded by an LFP recorded in layer 2/3. There were some differences between wakefulness and general anesthesia however, as the wakefulness produced persistent depolarization, which was not seen under general anesthesia. This does not seem to be a general dampening of the neural activity though, as sedation with fentanyl also produced persistent depolarization with POm activation in layer 2/3 cells, so something about isoflurane as an anesthetic reduces the persistent depolarization of layer 2/3 cells. Recordings of extra-cellular potentials in the POm also showed a massive decrease in firing during isoflurane anesthesia, compared with fentanyl sedation, suggesting the change occurs due to thalamic activity.

In a review of cortical function and anatomy, Cauller (Cauller, 1995) hypothesized the function of Layer 1 to be an integration zone for top-down and bottom-up signals. Bottom-up signaling has to an extent already been covered in this review (Lubke and Feldmeyer, 2007; da Costa and Martin, 2010; Constantinople and Bruno, 2013), where whisker stimulation is reliably transferred from touch to a graded neural response in the cortex, especially in layers 4 and 5. Top-down on the other hand focuses on the conscious attention to sensation, sometimes termed perception. Cauller (Cauller, 1995) cites work studying the difference in touch signaling in monkeys, where the touch response can be broken into two parts, the positive initial response (P1) and the negative initial response (N1). Both are termed by the neural network response to touch, with P1 occurring just before N1. P1 remains during anesthesia, while N1 is abolished. P1 is graded by how strong the stimulus was, but N1 is not present in monkeys reporting a false negative touch, but is present when they report a false

positive (where P1 is not present). This has lead researchers to suggest N1 is a conscious component of touch relating to attention and thought, while P1 is unconscious and is the pure touch signal built from sensation. For some, these responses are perfect analogs for top-down and bottom-up processing respectively. When looking for the maximum of both these responses in the cortex, P1 is at its peak in the middle layers of the cortex, around where the lemniscal pathway synapses. N1 was found higher, seemingly in layers 2 or 1. Unfortunately electrode recordings of these type that characterize these responses cannot resolve the distance between layers 1 and 2.

An alternate approach to separating top-down and bottom-up signals, is to use an odd-ball behavioral paradigm. Sensory stimulation is given in a train of habituation inducing stimuli, all very similar and spaced evenly apart. After habituation has occurred, a break in the chain is given with an unevenly placed, and slightly different 'oddball' stimulus. In this way, the sensory paradigm gives individual stimuli which can be measured, habituation which can be measured, and a surprise stimulus which can be measured. Bottom-up processing grades responses by the strength of the inputs, with no habituation or surprise, as it is creating responses based purely on the sensory inputs. Top-down processing gives habituation and can show surprise with an extra-large response. Using such an oddball paradigm with whisker stimulation, (Musall et al., 2015), and recording cortical activity with a current-source density electrode through all cortical layers, top-down and bottom-up responses were separated. Layers 2/3, and 5/6 all showed habituation and large responses to the oddball stimulus, indicating surprise. Layer 4 however had no habituation and showed no additional response to the oddball, until 400ms following its presentation. This is likely feedback from layer 2/3 or 5 and 6, indicating layer 4 produces no top-down information of its own. This feeds into the theory separating cortical layers into bottom-up areas, top-down areas, and areas where these two paths converge (Larkum, 2013).

Given the anatomy of the region, layer 1 would be the ideal region to integrate top-down with bottom-up processing. . The many convergent thalamic inputs to Layer 1 (Rubio-Garrido et al., 2009), and the feedback loop to Layer 1 resulting in bursting of Layer 5 neurons (Larkum et al., 2004). The massive horizontal fibers travelling across Layer 1 to distant cortical regions where it can integrate multiple inputs (Cauller et al., 1998), as well as the regular looping of

Layer 5 to Layer 1 and Layer 4 to layer 2/3, which in turn excites layers 5 and 6. All together, these suggest integration of multiple sources, all converging in layer 1.

The zona incerta of the thalamus is very important for cortical layer 1 function, despite the two areas not being directly connected. This nucleus is inhibitory and connects directly with the POm, which is a major source of excitation for layer 1 (Zhang and Bruno, 2019). The zona incerta is also very arousal dependent and seems to be turned on and off by cholinergic neurons of the brain stem (Masri et al., 2006), which are known to be on during wakefulness and arousal and dampened during sleep and unconsciousness (such as under anesthesia) (Trageser et al., 2006; Masri et al., 2009). Under this interaction, POm neurons fire at reduced rates during anesthesia compared with wakefulness (Masri et al., 2008) so it is to be expected that Layer 1 receives much more sensory input during wakefulness than during unconsciousness. This aligns with Cauller's theory of top-down, bottom-up integration in Layer 1 (Cauller, 1995). Some evidence for this exists in Cauller and Kulics' study (Cauller and Kulics, 1988), where a monkey falling to sleep showed a changed N1 response, as recorded by a local field electrode. As the N1 response is believed to occur in Layer 1 and modulation of it during sleep is in agreement with the work from Trageser et al (Trageser et al., 2006).

The role the primary thalamus plays, compared with the secondary thalamus, on cortical activation has been examined. These studies demonstrate the difference between bottom-up processing and top-down, and the effect is has on cortical activity. Llinas, Leznik, and Urbano (Llinás et al., 2002) used acute thalamocortical slices to examine the effect of stimulation in the thalamus, on cortical activity, around the somatosensory pathways. The slices were bathed in a voltage sensitive dye (VSD), so activity in the entire cortical slice, and thalamus could be recorded, during and following the stimulation (via electrode). Stimulation in the ventrobasal thalamus (including VPM), as expected, produced large depolarization in cortical layer 4 of the somatosensory cortex (S1), with less activity triggered in cortical layers 5 and 2/3. Stimulating the centrolateral thalamus (including POm) lead to all cortical layers in S1 being activated. When stimulating both thalamic areas simultaneously, a massive cortical depolarization occurred, especially in S1 layer 5 neurons. This depolarization was greater than the sum of just centrolateral and ventrobasal stimulation

on their own, pointing to coincidence detection between the pathways, and non-linear summation, in line with theories of coincidence detection in pyramidal cells (Schiller and Schiller, 2001; Larkum et al., 2004). Supra-linear summation of inputs was also shown when the centrolateral thalamus was stimulated with gamma-frequency pulses, resulting is a growing depolarization in S1 and particularly layer 5 neurons. This did not occur with ventrobasal thalamic stimulation at gamma frequencies. Finally, to reinforce the idea of coincidence detection, a small incision was made in the cortical slice, severing horizontal connections through the cortex, except for layer 1. Stimulation on layer 1 showed that activity did not spread beyond this incision. Combining the layer 1 stimulation with ventrobasal stimulation however restored the massive depolarization across the cortex even beyond the incision, suggesting layer 1 carries the coincidence detection between primary and secondary thalamic inputs into S1.

Looking further into barrel cortex and physiological differences between cortical layers, Lacefield et al (Lacefield et al., 2019) recorded barrel cortex neuron responses during a reinforcement learning task. When the mouse detected a pole with its whisker, it could press a lever and a water reward was delivered. In this way, they could record the cellular activity in response to the pole touch, and to the reward delivery (or expected reward). Activity was recorded using two-photon imaging of GCaMP expressed in specific subsets of cortical neurons (layer 5 pyramidal cell apical dendritic tufts, layer 4 spiny-stellate cell soma, layer 2/3 pyramidal cell soma and apical dendritic tufts) through a cranial window. Layer 5 pyramidal cell dendritic tufts responded strongly to both random water rewards, and pole detection, but preferred the pole detection. Layer 2/3 apical dendritic tufts, and soma also showed responses to both pole detection, however the soma showed a larger response to the pole detection while the dendrites preferred the random rewards. In contrast, layer 4 spiny-stellate cell soma showed only a small response to pole detection, and no response to the random rewards. This demonstrates the differences between top-down (layers 2/3, 5, 6) and

bottom up (layer 4) processing, and lines up with work from Musall et al (Musall et al., 2015) in their oddball paradigm.

Cortical Oscillations

Cortical oscillations occur when certain configurations of neuron networks oscillate their membrane voltage, in phase with each other. This seems to be an emergent property of the network (Buzsáki and Draguhn, 2004; Bartos et al., 2007; Buzsáki, 2009; Buzsáki and Wang, 2012; Dumont et al., 2017; Dumont and Gutkin, 2018), where given the correct initial conditions, oscillations will occur out of noisy input signals to the network. These oscillations are classified by their frequency and power. Bands of frequency are grouped together, as we see characteristic frequencies in a range appear under certain conditions and in specific brain regions (Buzsáki, 2009). Slower oscillations tend to have larger power in the brain, with a decreasing power following a log scale with the increasing frequency (Buzsáki and Draguhn, 2004). The primary oscillation bands are split into delta (0-4 Hz), theta (4-10Hz), beta $(10 - 30Hz)$, and gamma (30+ Hz), in rodents (Buzsáki, 2009). These bands are slightly different in primates, but the same names are used as they are thought to relate to specific neural features, rather than an arbitrary frequency band.

The slower oscillations (delta, theta, beta), in cortex tend to be less studied than gamma. These larger oscillations are less local, and also can be very large in power (Buzsáki and Draguhn, 2004). It is thought that some arise from looping circuits connecting the cortex and thalamus (Buzsáki, 2009). This is especially thought for the cortical theta rhythms, which would make them more an analog of human alpha rhythms than the hippocampal theta rhythms which can also be found. Sun and Dan (Sun and Dan, 2009) found a difference in slower rhythms in the rat visual cortex, separated by layer, with a large peak around 2Hz, in layer 2, while layer 5 had a lot of beta activity and no 2Hz peak. These oscillations, and especially the beta rhythms were activity dependent, so reflected the local activity in some way.

Gamma oscillations in cortex and hippocampus are probably the most studied form of neural rhythm. Partly this is because they tend to be local (Buzsáki, 2009), making the study of any area with them easier, but also we have a better idea of how they arise than other oscillations. It has been known for some time that inhibition is key to synchronized neural activity (Skinner et al., 1994; Van Vreeswijk et al., 1994), and that is particularly true for gamma oscillations. Computational models can create neural networks with spontaneously generated gamma oscillations, either with purely fast-spiking interneurons (Dumont et al., 2017;

Dumont and Gutkin, 2018), or with a mix of fast-spiking interneurons and excitatory pyramidal cells (Bartos et al., 2007; Dumont et al., 2017; Dumont and Gutkin, 2018). Experimentally, the mechanism of gamma has been probed (Buzsáki and Wang, 2012), perhaps most conclusively using optogenetics to drive or inhibit gamma rhythms in networks (Sohal, 2012). Optogenetic drivers could create gamma rhythms reliably when driving fast-spiking interneurons, but not when driving pyramidal cells in the same network. Other rhythms could not be generated this way. This suggests that fast-spiking interneurons (parvalbumin expressing) lead the gamma generation in cortex, and then entrain the pyramidal cells to the same rhythm. Similarly, using an optogenetic inhibitor on fast-spiking inhibitory cells, gamma could be decreased (not all cells were transfected with the optogenetic inhibitor, so a complete stop was not expected). Additionally, while gamma was occurring in the network, signals coinciding with the gamma peaks were enhanced, and those that did not were inhibited. This suggests that gamma plays an important role in shaping cortical signaling. This is in line with theoretical work by Dumont and Gutkin (Dumont et al., 2017; Dumont and Gutkin, 2018). Using somewhat realistic cortical neural networks made of pyramidal cells and fast-spiking interneurons, they studied how signal transduction within a network and between two networks is affected by gamma oscillations. Their work shows how the timing of signals within a gamma oscillating circuit can be enhanced by occurring to coincide with the peak of the oscillation.

Bieler et al (Bieler et al., 2018) studied multisensory integration, between whisker and visual pathways, *in vivo*. Recordings were made in the primary thalamic nuclei VPM for whiskers, and lateral geniculate nucleus for vision. Additional recordings were also made in S1, and primary visual cortex. Simultaneous whisker and visual stimulation lead to greater activation of both thalamic nuclei, but also a binding of beta and gamma oscillations between them. Further, whisker stimulation alone could induce gamma oscillations in S1, but simultaneous whisker and visual stimulation increased the binding of gamma oscillations in S1 with beta oscillations in the thalamus.

All together these studies tie into the communication through coherence theory (Fries, 2005; Bastos et al., 2015). The basis of this theory is that neural networks are held by a relatively inflexible network architecture (cell connections can change, but not on the millisecond to

second time scale), but brain regions need to communicate with various areas, depending on the task at hand. If they were to communicate with all areas they were connected to, all the time, it could lead to an excess of noise over signals in the brain. This theory posits that oscillations allow brain areas to communicate selectively, by synchronizing oscillations with the region it is targeting, and desynchronizing with unintended target areas. In this way, the network architecture can stay static, but by simply tuning the frequency and phase of activity, like a radio, the intended area can be dialed into.

VSD imaging has been successful for recording neural oscillations. As bulk loaded VSD reports average membrane potential, the main signal captured is from synchronized neural activity (Antic et al., 2016). Synchronized activity is a requirement of neural propagating waves (Wu et al., 2007) and oscillations, so it is no large jump to record neural oscillations and waves with VSDs. The synthetic voltage dye RH414 successfully recorded oscillations up to 15Hz in turtle olfactory bulb, during odor sensing (Lam et al., 2000). The dye RH1692 captured slow-wave oscillations covering massive areas of the cortex in awake mice (Mohajerani et al., 2010). Acute slices with VSDs and genetically encoded voltage sensitive fluorescent proteins have been useful for probing oscillatory networks (Wu et al., 1999; Leznik et al., 2002; Bao and Wu, 2003; Bai et al., 2006; Akemann et al., 2012; Yoshimura et al., 2016). Derdikman et al (Derdikman et al., 2003) used RH-1691, 1692, and 1838 to image urethane anesthetized rat barrel cortex, during whisker deflection. Here, a large 16Hz oscillation was detected in the cortex following whisker stimulation, but it could not be depth resolved. Faster oscillation peaks were not found. This has been characteristic of oscillation detection using voltage dyes – fast and small oscillations can be detected *in vitro*, where slices and ultra-fast cameras can access the cortical networks more specifically. *In vivo* however, fast oscillations have been difficult to detect, although oscillations have been found (Antic et al., 2016).
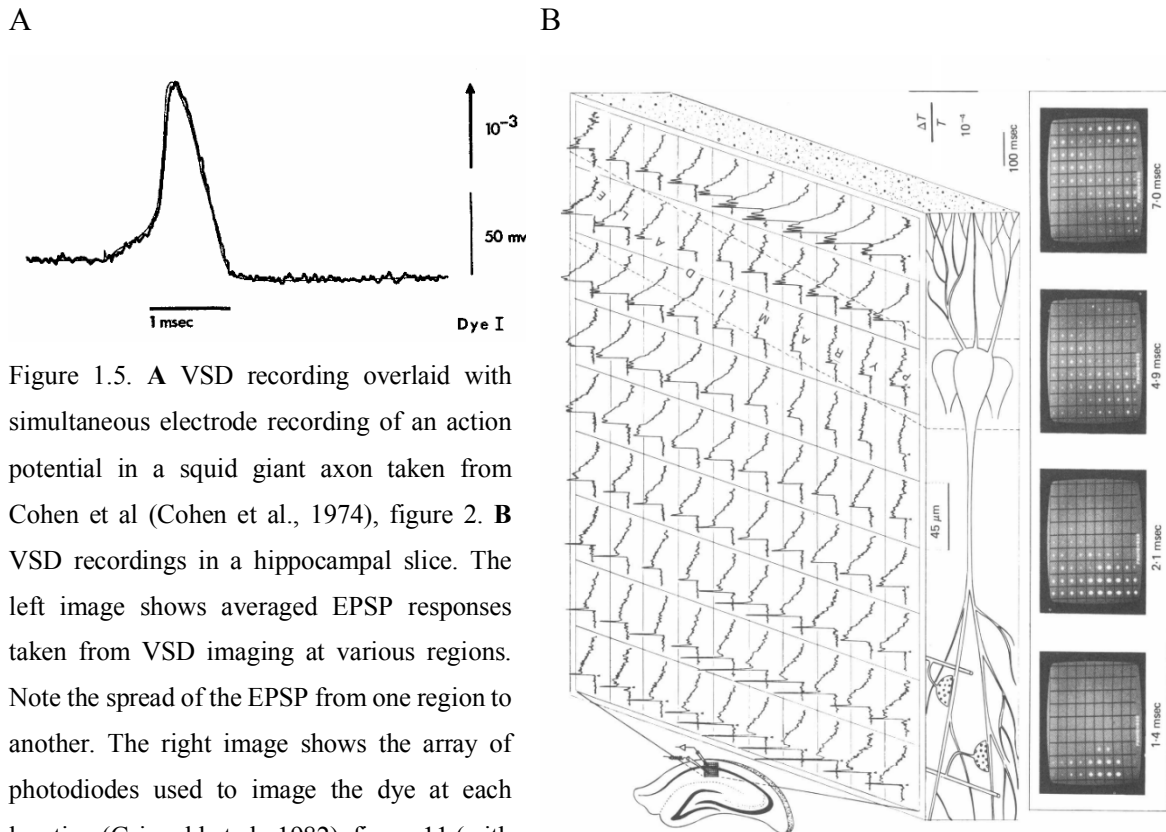
Voltage Imaging of Network Activity

A

B

Figure 1.5. **A** VSD recording overlaid with simultaneous electrode recording of an action potential in a squid giant axon taken from Cohen et al (Cohen et al., 1974), figure 2. **B** VSD recordings in a hippocampal slice. The left image shows averaged EPSP responses taken from VSD imaging at various regions. Note the spread of the EPSP from one region to another. The right image shows the array of photodiodes used to image the dye at each location (Grinvald et al., 1982), figure 11 (with permission, John Wiley and Sons).

The main advantage of VSD imaging of neural activity in single neurons or networks is that imaging gives spatial scale in a way that electrodes and other techniques cannot hope to match (Grinvald and Hildesheim, 2004; Shafeghat et al., 2016). Although the temporal resolution is often not as good as in electrodes (limited by the read out of a camera sensor, or scanning speed of a microscope), the ability to place functional changes to a specific area and look at the neuronal morphology simultaneously can be very valuable. Synthetic voltage dyes work by embedding themselves in cell membranes and as an electric field passes across the membrane it alters the fluorescence of the dye (Kuhn and Fromherz, 2003).

The first application of a voltage dye in a biological tissue was by Tasaki et al (Tasaki et al., 1968), who were looking for ways to optically measure functional changes in neurons. They identified action potentials in dissected crustacean nerves using the dye 8-anilononapthalene-1sulfonic acid. The signal they achieved from these recordings was 0.002% change in fluorescence for an action potential. Cohen et al (Cohen et al., 1974) continued the voltage dye route of investigation and screened hundreds of compounds to find a series of voltage

dyes (cyanine family of dyes) that produced the best signal. As shown in Figure 1.5a, the optical signal achieved in these recordings, although small in terms of absolute change, follows the electrical recording very well. This demonstrates the appeal of VSDs, as it is possible to achieve optical recordings that match electrical recordings almost exactly, except that optics can be expanded to also collect spatial information. Grinvald, Manker and Segal (Grinvald et al., 1982) recorded network voltage activity using a VSD in acute hippocampal brain slices. Because VSD signals are generally small (typically $0.1 - 1\%$ change in fluorescence in physiological conditions), all trials they performed required averaging in order to come up with significant voltage signals. Still they recorded paired pulse voltage spread, with paired pulses of excitation from stimulating electrodes and a rising excitatory post-synaptic potential (EPSP) in response to the second stimulation. They also identified the dendrites as the primary source of signal for VSD imaging, because the action potentials are very brief depolarizations and then repolarizations in membrane potential. These average out to no change in fluorescence unless captured under extremely high resolution. The only way to image action potentials is if a large number of them in a nearby region synchronously fire, so that the fluorescence change is so large that it will be visible in a very small time window. This is unlikely in many brain regions. Dendrites on the other hand produce extended periods of depolarization, with no following hyperpolarization, making them much easier to detect. There is also a secondary phase of depolarization produced by glial cells, although this works on a much longer time scale (seconds, rather than tens of milliseconds for dendritic EPSPs) (Konnerth and Orkand, 1986; Lev-Ram and Grinvald, 1986). An example of VSD recordings (Grinvald et al., 1982) in response to hippocampal stimulation is shown in Figure 1.5b, illustrating the spatial resolution possible with VSD recording. The spatial resolution of these signals, as well as the signal-to-noise ratio have increased greatly since 1981, to a point where no averages are required to detect certain neural signals. For example, Shafeghat et al (Shafeghat et al., 2016), and Roome and Kuhn (Roome and Kuhn, 2018), who achieved single action potential detection in neurons stained with a VSD, and fluorescence changes of greater than 20%.

Network activity recordings of the barrel cortex have been taken using VSD imaging over the last three decades in several ways (Orbach et al., 1985; Kleinfeld and Delaney, 1996; Petersen et al., 2003; Berger et al., 2007; Kuhn et al., 2008). Orbach, Cohen and Grinvald

(Orbach et al., 1985) simply poured their dye over the pia-mater and allowed it to seep into the neurons on the surface of the brain. This targeting of the upper layers allowed field investigations that were not possible with electrodes. Because the VSD preferentially translates dendritic potentials rather than action potentials, unlike the single unit recording electrodes, this study showed a unique signal in the upper barrel cortex to whisker stimulation in terms of neural response over time and cortical area.

Kleinfeld and Delaney (Kleinfeld and Delaney, 1996) used dye in a similar manner, imaging cortical spread of whisker excitation over time. The dye was shown to only spread to layers 1, 2 and 3 in any meaningful concentration, while their microscope could only effectively pick up signals from the upper 200μm, limiting their signals to a mix of layers 2 and 1. They effectively showed stimulation spreading over approximately 1mm in the course of about 13 seconds. In the excellent research by Petersen, Grinvald and Sakmann (Petersen et al., 2003), a VSD was again diffused through the upper layers of barrel cortex, but was accompanied by whole cell electrode recordings and optical neural reconstructions. Through this they were able to identify the network dendritic signal, combined with single cell spiking activity. Membrane potentials of layer 2/3 pyramidal neurons were very well correlated with the local VSD response, especially following whisker deflection. In this way, VSD recordings at least in cortical layer 2/3 can be interpreted as a good analog of the membrane activity of the pyramidal cells there. It is unknown how strong this relationship is in layer 1, or deeper layers however. In terms of calibrating and verifying VSDs, they showed neurons without dye had the same electrical responses as those with dye, and neurons without electrodes had the same VSD signal response as those with electrodes attached. Additionally with the combination of whole cell recording and a VSD around the same neuron, changes in the whole recording could be used to calibrate the dye, showing that the dye is accurate to within 2.0 mV rms (Dye RH1681). Their results showed early responses to the whisker stimulation confined to a single barrel column, about 13 ms after the whisker was touched. This then spread to the
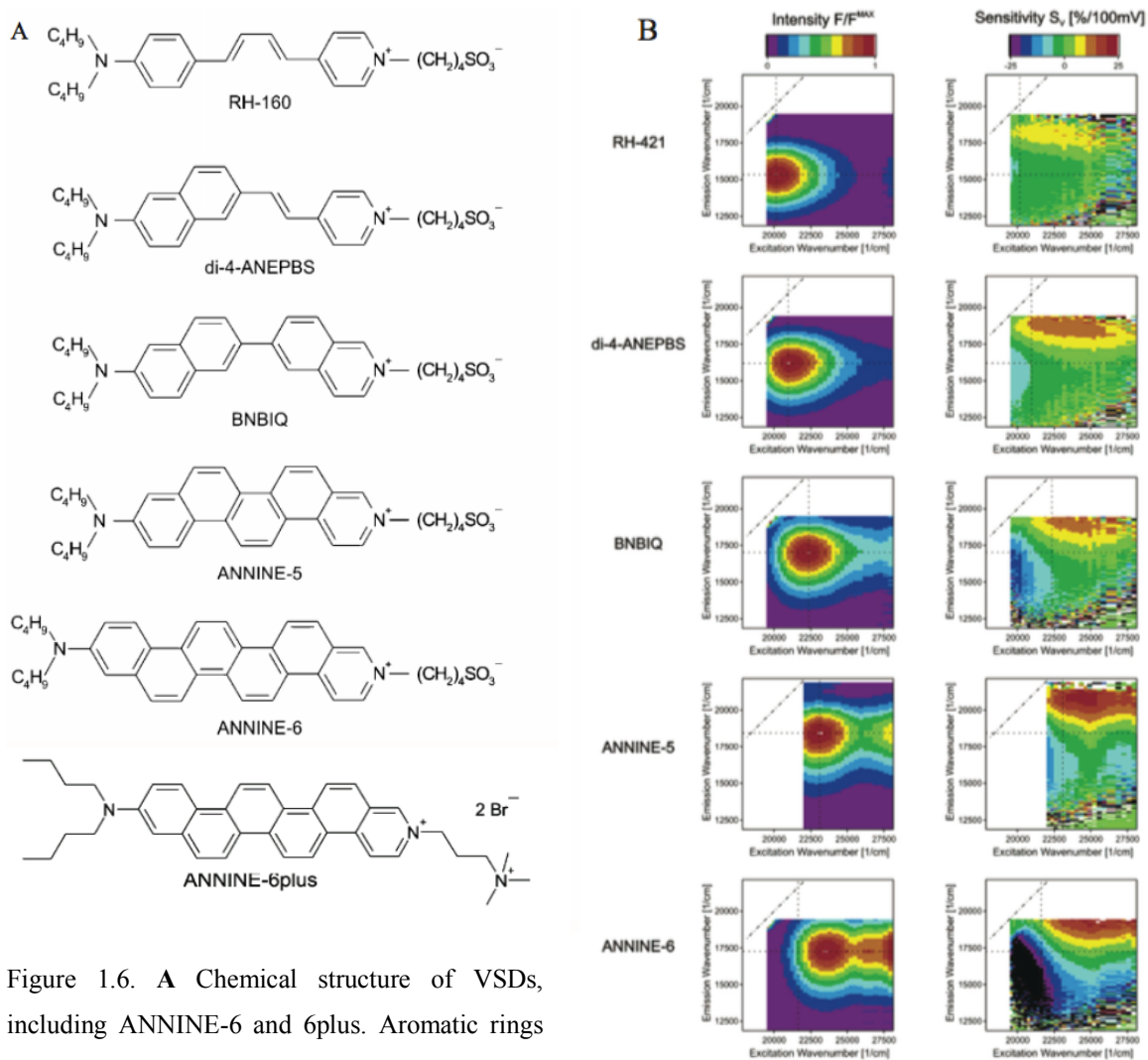
Figure 1.6. **A** Chemical structure of VSDs, including ANNINE-6 and 6plus. Aromatic rings incorporated into the ANNINE dyes, preventing any twisting or turning. Figure adapted from (Kuhn and Fromherz, 2003), figure 1 (with permission, American Chemical Society), and (Fromherz et al., 2008), figure 1 (open license). **B** 2D fluorescence spectra are shown for excitation/emission and 2D sensitivity to voltage change. Figure from (Kuhn and Fromherz, 2003), figure 3 (with permission. **C** Sensitivity to various excitation wavelengths in the two-photon excitation regime. Sensitivity obviously increases with longer wavelength, as the excitation moves further along the excitation spectral edge. Figure adapted from (Kuhn et al., 2004), figure 5 (with permission, Elsevier).

neighboring barrels in about 20 ms and greatly increased intensity from about 50 to 100 ms, before dying down by the 200 ms mark. This spread was Gaussian in shape and graded in intensity and area, based on the strength of the original whisker stimulation. In a similar area of research Berger et al (Berger et al., 2007) using combined VSD (RH1691) and calcium dye labeling (Oregon Green 488) to look at the same whisker responses in barrel cortex. The calcium dye showed action potential bursts, as action potential bursts in cortical pyramidal produce a large calcium ion influx into the cytosol on a longer time scale than the membrane voltage.

Blocking glutamate transmission, just as Petersen, Grinvald and Sakmann did (Petersen et al., 2003), blocked VSD signals, but only reduced the calcium signal by half. This suggests the calcium dye shows a mix of pre and post-synaptic actions, but the VSD primarily picks up post-synaptic potentials, in line with previous studies linking VSD signals to dendritic activity. The time scales and spread of excitation found was very similar to the work of Petersen, Grinvald and Sakmann (Petersen et al., 2003).

The VSDs used in our lab are from the ANNINE family of dyes (Hübener et al., 2003; Kuhn and Fromherz, 2003; Kuhn et al., 2004; Fromherz et al., 2008). ANNINE-6 was designed from the family of hemicyanine dyes, to be more stable and have higher voltage sensitivity. ANNINE-6 has six aromatic carbon rings bridging its aniline and pyridinium groups (Fig. 1.6a), and while ANNINE-3, 4, 5, 6 and 7 were synthesized, ANNINE-6 was found to be the best for voltage imaging in cell membranes (Hübener et al., 2003; Kuhn and Fromherz, 2003; Kuhn et al., 2004). The aromatic rings of the ANNINE family dyes prevent twisting around the flexible bonds found in the other styryl dyes, which makes the voltage sensing process of ANNINE much more controlled and predictable. Additionally, with more aromatic rings the solvatochromism, or shift of excitation and emission wavelength due to the polarity of the solvent, of the dyes increased and always stayed symmetrical. This indicates a larger charge shift within the chromophore, so if a dye molecule is embedded in a lipid bilayer it can change its fluorescence with small changes in the membrane position caused by solvatochromism, or from an interaction of the molecular charge shift with an external electric field over the membrane (electrochromism). ANNINE-6 and ANNINE-6plus were found to be purely electrochromic (Kuhn and Fromherz, 2003). A larger charge shift linearly correlated with a

larger spectral shift and thus a larger voltage signal (2D fluorescence spectra are shown in Fig. 1.6b). The positive trend of increasing charge shift is countered by the increasing hydrophobicity with increasing length, making ANNINE-7 insoluble under biocompatible conditions.

ANNINE-6plus is very similar to ANNINE-6, but the negative headgroup of neutrally charged ANNINE-6 is replaced by a positively charged headgroup so that ANNINE-6plus has two positive charges in solution (Fig. 1.6b). ANNINE-6plus shows the same spectral characteristics as ANNINE-6, and has similar membrane binding properties, but has the advantage of being much less hydrophobic. This means staining procedures using ANNINE-6plus do not have to use surfactants such as Pluronic F-127 in DMSO, which may alter cell function (Tsvyetlynska et al., 2005; Hanslick et al., 2009). Also ANNINE-6plus can stain cells intracellularly, while intracellular up-take of ANNINE-6 is near impossible (Fromherz et al., 2008). Additionally ANNINE-6plus and ANNINE-6 were found to be some of the least neuro-active VSDs available (Mennerick et al., 2010). Only under extreme photon exposure was there any detected hyperpolarization with ANNINE-6plus staining, but under its normal two-photon use, there should be little to no hyperpolarizing currents associated with ANNINE-6 and ANNINE-6plus staining.

To further increase the sensitivity of ANNINE-6 (and ANNINE-6plus), Kuhn, Fromherz and Denk (Kuhn et al., 2004) demonstrated that exciting the dyes not at the spectral flank, but at the spectral edge produces a typically five-times larger voltage sensitivity (intensity change per photon per mV). This also dramatically reduces photo damage to the cells and bleaching of the dye, because fewer photons deliver more information. The increased voltage signal on the far spectral edge comes about because a pure spectral shift (as expected from a pure electrochromic dye) results in no relative change at the peak, but a theoretical infinite relative change at the very spectral edge. The random noise of the measurement primarily comes from shot noise of photon detection (rare and uncorrelated events), so Poisson statistics can be applied. Relative noise is given by $N = \sqrt{(n)}/n$, where n is total number of detected photons. This means gain in sensitivity at the spectral edge more than offsets the increase in noise from reducing the total fluorescence. The largest sensitivity measured for ANNINE-6 was 0.35%/mV for one photon excitation and 0.52%/mV using two-photon excitation. Two-

photon excitation occurs when two photons of half the typical excitation energy (that is twice the wavelength) simultaneously reach a chromaphore and add up their energy to excite an electron of the chromaphore which then in turn can emit a photon (Denk et al., 1990). Using two-photon microscopy reduces background noise, overcomes some of scattering of light in the brain, and allows for sectioning. Also two-photon microscopy was shown to increase the sensitivity of ANNINE-6 by about 20%, compared to one photon excitation (Kuhn et al., 2004).

Introduction to Thesis Work

Using ANNINE-6 and two-photon microscopy, Kuhn, Denk and Bruno (Kuhn et al., 2008) imaged activity in mice barrel cortices during anesthesia and waking. Spontaneous and whisker evoked neural activity was collected with an electro-encephalogram (EEG), which was compared with the voltage dye response, in layers 2 and 1. Most recordings were made using a line-scan where the focal spot of excitation moves only in a line, rather than scanning a plane. This creates a very rapid image, recorded around 1 kHz, but contains only one-dimensional spatial information. The combination of this scanning with a two-photon microscope allowed them to take average membrane voltage recordings of the upper cortical layers in much finer precision than previous VSD applications to the barrel cortex (in terms of z-plane resolution). For the first time Layer 1 field recordings were isolated. The size fluctuations in fluorescence were even converted to changes in electric field, given an assumed density of dendrites in Layer 1 (-1.1% change in fluorescence translates to a 10mV fluctuation).

Cross-correlations showed recorded voltage diverged from the EEG recordings in Layer 1 during waking but increased in layer 2. This is attributed to the inhibition of the zona-incerta (Trageser et al., 2006), which allows Layer 1 to begin integrating signals from multiple sensory pathways, resulting in a less synchronized signal and a departure from the overall cortical field activity picked up by the EEGs. Layer 2 at the same time focuses its activity and becomes more synchronized with the EEG. It is speculated that this might be from dendritic tufts from Layer 1 that only signal through Layer 2 with successive strong inputs. Layer 1 may receive all the noisy and small inputs, but only those integrated over a large

number of dendritic branches will spread down the dendritic tree, so the signals measured in Layer 2 will only be the strong and somewhat synchronous signals present in layer 1.

My project comes from the groundwork set by Kuhn, Denk and Bruno (Kuhn et al., 2008), taking advantage several technical advances that have occurred since 2008. Firstly, chronic window implantations for long term, non-invasive, non-traumatic imaging have become a widely established technique. In a collaborative paper (Holtmaat et al., 2009), the various labs performing chronic window surgeries describe the techniques used to create and implant a cranial window and image fluorescent molecules in the brain, as deep as 1.3mm through the cortex. The technique involves gently removing a small section of skull without damaging the dura mater below, and gluing a think glass window in its place. While fluorescent molecules originally had to be placed in the brain either before the window was in place, or through a separate access port, a recent advance demonstrates how a small silicone access port can be placed in the glass window and injections and electrical recordings can be taken through it (Roome and Kuhn, 2014). Together these advances allow easy application of ANNINE-6 and ANNINE-6plus to the cortex and deeper structures, and imaging of neural activity, especially in the upper cortical layers. Additionally, by combining two-photon microscopy with VSD imaging, recording neural oscillations at higher fidelity than previously recorded, using optical *in vivo* methods was possible. With two-photon microscopy's optical sectioning, investigations into layer 1 of the cortex become feasible, so gaining access to sensory responses in and around cortical layer 1, and recording any neural oscillations is the goal of this research.

Chapter 2

Simultaneous Voltage and Calcium Recording, in Barrel Cortex, *in Vivo*: Whisker Stimulation Responses

Brief Outline

In this work I recorded in anesthetized and awake mice, using VSD and GCaMP6f, with two-photon microscopy. I aimed to capture whisker stimulation responses in various cortical depths in the supra-granular layers, and compare the GCaMP6f activity with the VSD, over depths and cortical states. An LFP was also used as a reference to ensure barrel responses were captured and to compare the VSD signal to. Major differences were found between the LFP, VSD, and GCaMP6f signals, due in part to the cortical anatomy that they preferentially report activity from. The VSD showed a bi-phasic depolarization with a fast and slow peak, and potentially larger depolarization during anesthesia. GCaMP6f showed a massive increase in activity while the mice were awake, most likely due to thalamic afferents to layer 1 turning off during anesthesia. Cortical oscillations were also detected with the VSD, even at the upper edge of layer 1. These oscillations showed changes due to whisker stimulation, and in particular gamma had a very large response.

Introduction

Study of the super-granular cortex has historically focused on layers 2/3. With its large pyramidal cell bodies, and wide array of interneurons, it provides plenty of targets for electrodes and various types of imaging (Petersen et al., 2003; Stosiek et al., 2003; Berger et al., 2007; Au - Golshani and Au - Portera-Cailliau, 2008; Jouhanneau et al., 2015). This leaves layer 1 somewhat neglected. Electrical signals in layer 1 are often masked by the larger signals in layers 2/3, and synthetic dyes applied to the cortical surface generally sink down beyond 100µm, preferentially staining deeper layers (Orbach et al., 1985; Kleinfeld and Delaney, 1996; Petersen et al., 2003). Genetic targeting of protein sensors into dendritic tufts (Lacefield et al., 2019), or clever use of optogenetic drivers (Zhang and Bruno, 2019) provide good insight into some layer 1 functions, but do so in a very cell by cell basis.

Overall layer 1 activity is much harder to capture, and so far the best approach has been from (Kuhn et al., 2008). Loading a very lipophilic voltage sensitive dye (VSD) into the super-granular cortex meant dye stuck to membranes in layers 1, 2, and 3, and using two-photon microscopy to achieve optical sectioning meant all signals voltage recorded were present only in the optical plane being measured. Together this allowed recordings of average membrane voltage from within layer 1, without contamination from larger electrical signals in deeper layers. Using a VSD is particularly interesting in layer 1 study, as VSDs preferentially report dendritic activity (Petersen et al., 2003). Cortical layer 1 has a massive confluence of axons from distant cortical, thalamic, and deeper areas, with dendritic tufts from nearby cortical neurons. A VSD loaded into layer 1 thus primarily reports the average dendritic activity of the nearby neurons, with some influence from distant areas (Zhang and Bruno, 2019), as well as back-propagating activity from the cell body and deeper areas.

One area particularly lacking from layer 1 research is neural oscillations. Generally, oscillations are recorded using some form of electrode, or electrical field sensor (Traub et al., 1999). These approaches lead to extremely high temporal resolution and very low noise, but cannot separate smaller signal in areas like layer 1, from stronger signals in neighboring areas. In some cases, VSDs and fluorescent proteins have been used to see travelling waves, and neural rhythms in the brain (Lam et al., 2000; Zochowski et al., 2000; Akemann et al., 2012), but these are more often done in acute slice preparations (Iijima et al., 1996;

Pedroarena and Llinás, 1997; Tominaga et al., 2000; Zochowski et al., 2000; Jin et al., 2002; Kajiwara et al., 2007; Yoshimura et al., 2016; Kajiwara et al., 2019). This, to my knowledge, has never been used with two-photon microscopy however, except recently by our group, where optical sectioning would allow investigation of neural oscillations within layer 1. It is difficult to hypothesize what the network oscillations in layer 1 would comprise of. Pyramidal cells in deeper areas show a range of oscillations, including theta (6-10Hz, thought to be created from thalamocortical loops – (Buzsáki, 2009)), and gamma (30+ Hz, thought to be created by pyramidal, fast-spiking interneuron connections – (Bartos et al., 2007; Buzsáki and Wang, 2012)). However, how much of these frequencies are coherent across layers, enough to be detected within layer 1, where there is a mixing of dendrites from all cortical layers, is difficult to predict.

In this research, I recorded mouse barrel cortex using a VSD, in combination with GCaMP6f, loaded into layer 2/3 cells, in layers 1, 2, and 3, in lightly anesthetized and awake conditions, as well as during whisker stimulation. I show differences between the VSD signal, and calcium activity, as well as changes in both going through cortical depths and brain state. Additionally, using just the VSD, neural oscillations were captured in all cortical layers, as shallow as 25µm below the dura. These oscillations also show some changes during whisker stimulation.

Methods

Animals and Surgery

All animal experiments were performed in accordance with guidelines approved by the Okinawa Institute of Science and Technology Graduate University Institutional Animal Care and Use Committee (IACUC) in an Association for Assessment and Accreditation of Laboratory Animal Care (AAALAC International) accredited facility.

Male, Black6 mice, between 5 and 8 weeks old were chosen for chronic window surgery, following the protocol laid out by (Roome and Kuhn, 2014), inspired by (Holtmaat et al., 2009). In total, 15 mice were used, but some were excluded due to poor cranial windows, or not meeting the criteria for sufficient whisker response. This lead to 10 recording sessions, from 6 mice being used in the final data analysis.

The window surgery was performed over barrel cortex, and ensuring that the silicone window port, in the cranial window glass, was consistently slightly rostral of the target area. This was so that a micropipette entering the brain coming from the rostral direction, through this port, would land in the target barrel, around 200-400µm into the cortex.

Before starting the surgery, the window glass and silicone port were prepared, as described by (Roome and Kuhn, 2014). Using gentle clamping on the glass (circular glass coverslip, 5mm diameter, 170µm thick), a 1-1.5mm hole was drilled with a grinding bit, through the glass. This hole was then cleaned and filled with a liquid silicone solution, and hardening catalyst (Sylgard), and was then placed on the top of a heating sterilizer, to harden the silicone, for the duration of the surgery.

For the surgery, the mice were deeply anesthetized throughout, with gaseous isoflurane (2% to begin with, reducing as the surgery went on). Their heads were fixed in a stereotaxic frame, and they were given drugs to reduce pain and inflammation (Buprenorphine 0.1µg/g, Carprofen 5µg/g both delivered sub-cutaneous, and Dexamethasone 2µg/g delivered intra-muscularly into the thigh). The hair on the scalp was removed roughly at first with an electric shaver, and then more finely with hair removal cream. Eye ointment was also applied to protect the eyes during the surgery.

Once the hair was removed and the mouse fully anesthetized, the scalp was numbed with lignocaine gel, and a triangular flap of the scalp was removed, with a scalpel and surgical scissors. This exposed the skull from beyond bregma, to just below lambda, and all the way over the edge of the parietal bone on the left, and slightly less laterally on the right. The cut skin and exposed bone were then treated with lidocaine. The bone was also scrubbed clean with dry cotton swabs, exposing anatomical markers. These markers were further drawn out by drying the bone with compressed air. The area where the cranial window was to be opened was marked out (centered at -1.5 AP, 3mm Lateral on the left, with edges 2-2.5mm away). The areas around the marked window were lowered and smoothed using a diamond tip grinding drill bit. A channel around the window site develops during this process, and is then enhanced using a fine tip grinding drill bit. Once the bone over the window area is able to move freely from the rest of the skull, a toothpick was glued wide end down, onto the floating bone. While this was drying, a reference electrode was put onto the skull on the opposite side

of the skull. Silver wire (0.404mm thick, cut to 2-3cm long), with one end flattened by hammering or pinching strongly with pliers, was used as the electrode. A groove was ground into the skull where the electrode was then glued into, making sure the flat end of the electrode laid flat into the groove, so the wire did not raise much above the surface of the skull, and the end of the wire followed out over the back of the skull, where it curved upwards.

Once the reference electrode was completed, the floating bone above the window could be removed. Using the toothpick as a handle, the bone can be very carefully removed in a controlled fashion. Begin by gently rocking the bone back and forwards, cracking all the edges, and then moving in slightly larger motions, until the bone lifts up from the cranial surface, at which point it can be completely lifted off. At this point, the brain in cranial window was entirely exposed. If any blood was present, it was cleaned up with gelfoam soaked in saline and carprofen. Next, the glass window with silicone port were placed carefully over the cranial window. The silicone port needed to be placed on the rostral edge of the window, so some careful movements were necessary. Once in place, it was glued down using thin superglue. The exposed skull was then covered with dental acrylic, which then provided a flat platform to anchor a metal headplate to. This headplate had a hole in the center, keeping the cranial window visible, and had longer edges which could be connected to the microscope stage, so the mouse could be headfixed while imaging was going on. Once the headplate was firmly anchored with dental acrylic, and a water-tight well surrounded the cranial window, the surgery was complete.

Barrel Finding, and GCaMP6f Inoculation

Allowing several days for recovery from surgery, whisker barrel finding could begin with intrinsic imaging. Through trial and error, the A row whiskers were found to be closest accessible whisker to where the window port was placed. The mouse was head-fixed under the microscope, with a 2.5x objective (Zeiss A-Plan 2.5x/0.06), and a heating pad was placed under the mouse, with a rectal temperature probe also inserted, to maintain an internal temperature of 36.5 – 37 ℃. 0.2ml of Xylazine was given sub-cutaneously, plus gaseous isoflurane (approximately 1%), to maintain a constant, but light anesthesia. A piezo

controlled stick was placed on a single whisker in the A row for stimulation. Before intrinsic imaging began, a reference image of the cranial window was taken using white light, and collected through a green filter (leaving blood vessels dark), focused on the cranial surface. The microscope was then focused 200-300µm deeper, and the collecting filter was removed. An LED excitation light was tuned to 618-655nm and the white light was removed. The camera (PCO.edge 4.2 backside illuminated) was set to record at 100fps, with exposures close to 10ms long. The exposure time, and positioning of the LED red light were adjusted to give an optimal exposure, with very little clipped highlights or shadows, as well as even light across the cranial window. For any file recorded, 500 frames were taken (5 seconds), and the piezo stick was activated at frame 101 (1 second), giving a train of movements pulses for 10ms (delivered at 50Hz). After each file was recorded, there were 5 minutes wait with no stimulation, and minimal noise, so the brain activity could reduce again and the blood flow would return to baseline. 12-14 files were recorded for each session, and were then analyzed offline using a plugin to imageJ (IO and VSD Signal Processor). If a barrel was identified in an area of the cranial window, reachable from the window port, the whisker was recorded and the mouse was sent further into the protocol. If the barrel found was not clearly defined, or was not reachable, the mouse went to a new session of intrinsic imaging.

Local field potential (LFP) probing was used through the window port to further confirm a barrel could be reached through the port. This step was done with mice where the barrel found with intrinsic imaging was uncertain, or potentially too distant from the port.

Once a barrel location was identified and reachable, a micropipette (20µm tip, 300µm bore) loaded with a viral mixture of viruses (AAV1 GCaMP6f flex WPRE syn, and AAV1 CRE WPRE SV40 hsyn, diluted 1:1000) and fluorescein solution, so the pipette would be visible under two-photon imaging. Once the pipette was 300-400µm deep, centered in the area believed to be the target barrel, 70-140nl of viral mixture and fluorescein were injected by applying positive pressure to the micropipette. The micropipette was left in place while the solution diffused upwards, for 30-45 minutes, before removing the pipette.
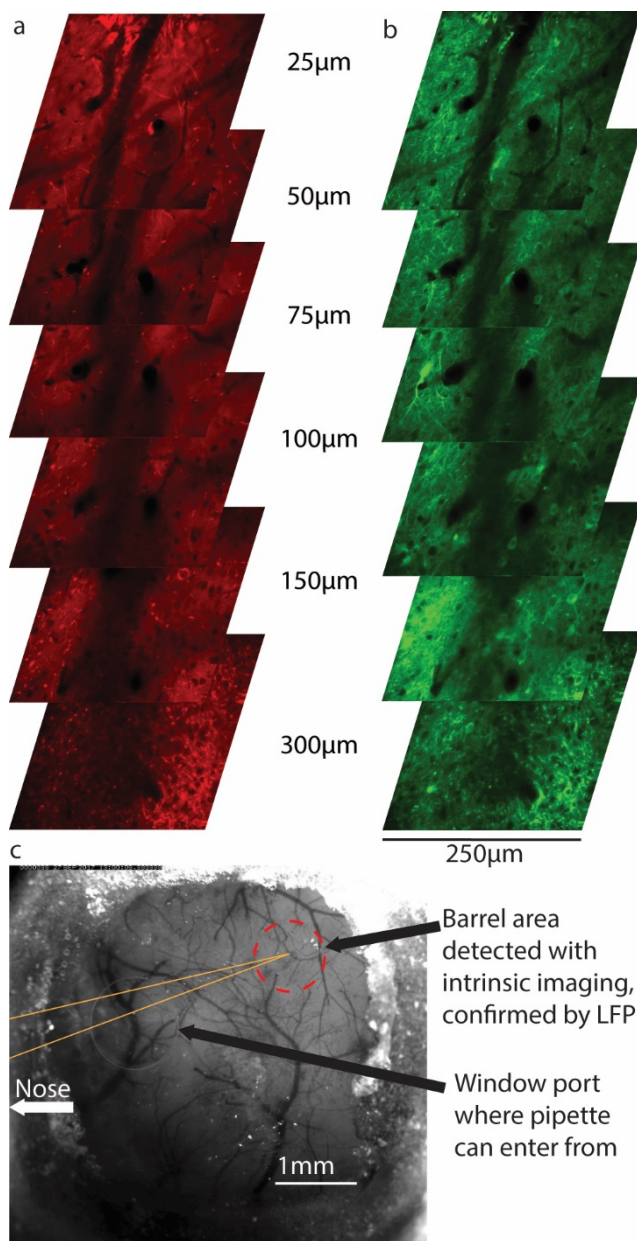
Figure 2.1. VSD (a) and GCaMP6f (b) through cortex, in areas that were later imaged. VSD and GCaMP6f images are separated by spectral filter into separate PMTs. Numbers indicate cortical depth, measured from the dura. Example cranial window (c), imaged before intrinsic imaging. The red circle indicates the intrinsic signal detected after stimulating an A-row whisker.

The virus needed at least 10 days to express to a level where imaging was possible, so in that time the mouse was introduced to the imaging setup, to reduce its eventual anxiety during imaging. This was done over at least two sessions on two separate days, for at least one hour. The mouse was anesthetized briefly with gaseous isoflurane and then headfixed into the microscope stage, with a moveable wheel under its feet. The lights were turned out, and the mouse was allowed to wake up and slowly familiarize itself with being headfixed and running on the wheel.

ANNINE-6 Delivery

Once GCaMP expression was visible in the target barrel (10 days to 3 weeks post inoculation), the mouse was deemed ready for imaging. On the morning of imaging, the mouse was anesthetized with gaseous isoflurane, and was temperature controlled with a heating pad and rectal temperature probe. A micropipette (20µm tip, 300µm bore) was loaded with up to 1µl of ANNINE-6 in solution (ANNINE-6 stock made up to 400mM in 20% pluronic f-127 in DMSO, then dissolved to 4-10% in saline, depending on desired brightness). The pipette was slowly delivered into the

target barrel, making sure to also co-localize with GCaMP expressing cells and fibers. This targeting was done under two-photon microscopy, with the pipette entering the window port at 27º to the window, with the beveled pipette tip down, cutting into the silicone and making a clean track towards the target area. Once in place (target barrel, 300-400μm below the dura), positive pressure into the pipette pushed the ANNINE-6 solution into the brain. The dye delivery was performed slowly and carefully, aiming for 500-800nl of dye to be delivered over 45 minutes. Once dye delivery was completed, the pipette was left in place while the dye diffused, for an additional hour. At that point the pipette was removed, the mouse woke up, and returned to its home cage. As DMSO can influence neural activity (Tsvyetlynska et al., 2005; Hanslick et al., 2009), I waited 7-8 hours after completing the injection, before functional imaging could begin.

During this waiting period, the excitation laser (pulsed Ti:sapphire laser, Coherent Chameleon Vision II) was left on and tuned to 1020nm, to ensure the laser would be warmed up and stable during functional imaging.

Combined Voltage and Calcium Imaging

After 7-8 hours of ANNINE-6 being in the target area, the mouse was returned to the imaging stage, under anesthesia. A heating pad and rectal probe again kept the mouse's body temperature between 36.5 and 37 ºC. The target area was investigated for an area with good GCaMP6f and ANNINE-6 labelling, going from 0-300μm deep (measured from dura, marked with second harmonic generation under two-photon imaging). Once a suitable imaging section was identified, a local field potential electrode (LFP) was moved into the target area (made from micropipette with extended tip - 20μm opening 300μm bore, 8-15 MΩ, with tip being 2-3cm long. The pipette was filled with fluorescein solution, contacting the silver wire electrode). The reference electrode implanted onto the skull during anesthesia was used as a reference against the LFP. Recordings were made of voltage changes after a 50x pre-amp and recorded with a HEKA Patchmaster amplifier. Next, an image stack for further reference was taken. Imaging planes were then chosen within this area for functional imaging. Generally six depths were chosen (depths chosen out of 25, 50, 75, 100, 150, 200, and 300μm below the dura), as more lead to too long an imaging session which might stress the mouse out too much.

Functional imaging started at either the deepest, or shallowest imaging plane. First, a reference image was taken under the same magnification as the functional linescan was taken (microscope objective Olympus XLPlan N 25x/1.05 W MP, microscope zoom 2x). This image was 512x512 pixels, relating to approximately 250μm by 250μm. The linescan would be taken across the middle of this image (in the horizontal plane). Imaging was then set to linescan, (512 pixels by 1 pixel, 2 kHz recording speed) and the laser power was stabilized (control of laser power was given to an oscilloscope, the laser dehumidifier was turned off, and power optimization hunting was turned off). 30 files, 12 seconds long (the first second is removed during data analysis) were taken at each imaging depth, with two air puffs delivered at set times (3 seconds and 8 seconds), to the contralateral whisker-pad (air coming from the caudal, lateral direction, ensuring it moves most whiskers on the whisker-pad and especially the A row, but does not hit the eye or move too much fur). Collected light was filtered through a dichroic mirror and additional filters (SEMROCK FF01 520/60nm, FF01 650/200nm), into two photomultiplier tubes PMTs (GaAsP photomultiplier tube. Hamamatsu), meaning one PMT captured green, or GCaMP6f signals, and the other PMT captured red, or ANNINE-6 signals.

After 30 files were recorded, this process was repeated at the remaining depths, and then the mouse was woken up (heating pad and probe removed, isoflurane turned off, and tube delivering anesthesia was moved away, plus the mouse was allowed 30-45 minutes to wake up fully). The recordings were then repeated again, in the same order of depths that they were taken during anesthesia. Recordings at this time were of the two imaging channels, the LFP signal synced with the imaging, and any movement of the wheel the mouse was sitting on (relating to running behavior). After all the depths were captured, the mouse was returned to its home cage.

Data Collection and Analysis

Some techniques used in the following data acquisition and analysis section are common to all the experiments. I present it once here, but it is used in all further data handling.

Data Acquisition

Data were collected through three separate computers, and synchronized with a trigger signal, originating from the microscope controlling computer, running ScanImage. The microscope scans a line in the brain, and emitted light is collected, then separated by a dichroic mirror and filters, before converting to electrical current through two separate photo-multiplier tubes – one for each color channel (red and green). Scan View records the amplified current from the PMTs, creating a brightness value for each pixel, in the red, and the green channels. These are arrayed into a line, representing the line being scanned in the brain. These are represented in the output tiff file in the horizontal direction. Each new line scanned is added below the previous line. These are represented in the vertical direction in the output tiff files (down being forwards in time). 1000 lines create an image frame, and these are stacked on top of each other, for ease of writing to disk. The final output tiff file is 512 pixels across, 1000 lines down, and 48 (in the usual recording scheme, as two channels are recorded and interleaved, so 12 seconds creates 24 frames for each channel) frames deep. Green and red channel frames are interleaved through the tiff file.

Data import

Analog files, in a Matlab data format (.mat), from Patchmaster, are imported to Matlab. A custom built script runs to separate each recorded session into its constituent parts, saving each as an individual Matlab data file (.mat). This means every recorded session, each corresponding to a single ScanView Tiff stack, is separated into four files – the local field recording, the stimulation triggering the air puff, a treadmill motor activity, and either the corresponding treadmill motor activity, or an ECoG recording.

Line Scan Handling

All line scan stacks (512 pixels, by 1000 pixels, 48 frames) were initially treated the same way. First the green and red channels (PMT 1 and 2) were de-interleaved, resulting in two stacks, 24 frames deep. These frames were then sequentially stitched together, making a single image, 512 pixels across showing the spatial scale of the line scan, and 24,000 pixels down showing the time course of the scan.

For measurements of fluorescence change over time, the scan was then averaged spatially, giving a single average pixel brightness across time. At this point, the first second of

recording was removed, to avoid any warming artifacts generated from the imaging system. To generate a ∆F/F measurement from this, sections of time with no stimulation were taken and averaged to generate a baseline fluorescence. This was subtracted from the fluorescence signal at each time point, and the result was the divided by this baseline again, creating a normalized fluorescence signal over time.

For frequency analysis, line scan frames 24,000 pixels long, 512 wide were first trimmed of their first second. Then the first four pixels in the spatial dimension were averaged over time, and a fast-Fourier transform was calculated on them. The output of this was saved, and the next four pixels were selected, by sliding the averaged section over by one pixel. This overlap helps smooth outlying frequencies. Once all pixels had been analyzed, the output of all the fast-Fourier transforms were averaged, creating one frequency spectrum for the line scan. This spectrum was limited to 1 kHz at the higher end. The lower end was limited to 0.09 Hz, if the entire scan time was used. In some cases with stimulation given during the scan, it was broken up into smaller time blocks, creating frequency spectra for each smaller time block.

For this set of experiments, all data were imported into Matlab (Mathworks), as described above, where custom in-house scripts were used to process them. Imaging data were split into separate channels, relating to each PMT, and were normalized for percentage change in baseline fluorescence (expressed as ∆F/F). These normalized traces were averaged across all 30 files recorded for a given depth, and around each air-puff delivery, resulting in 60 total averages making a single trace. If both the VSD and GCaMP6f showed a transient, and the VSD showed depolarization (GCaMP6f often shows no response during anesthesia, which is normal), the files were selected to continue for further analysis. This selection was performed for each depth and state recording for each animal, so that if files from one depth were too cross-contaminated, the other depth recordings may still be used.

Files selected for further analysis were averaged with other recordings from the same cortical depth and brain state (anesthetized vs awake), around the air-puffs. These averaged traces were then compared for cortical depth, and brain state (Fig. 2.2). For awake trials, files when running was detected during the air-puff delivery were also removed from the averages, because movement artifacts could not be corrected for in linescans.

These same files were then used to calculate frequency spectra. Each individual file was analyzed, before normalizing the recording. Each VSD file was filtered in 4pixel sliding average blocks, reducing the 512 pixel width to 509 pixels.

Each pixel then was used to calculate a frequency spectrum for baseline periods, and another for air-puff periods (1.5 second blocks for three baseline spectra, and 0.25 seconds before and 1.25 seconds following each air-puff) , with the fast-Fourier function in Matlab (Mathworks). These spectra were averaged across all pixels, and then across all files in that depth for that animal, and eventually across animals as well, creating average frequency spectra for stimulation, and for baseline periods, for cortical depth, and brain state. Comparisons between air-puff (stimulation) and baseline periods were made within each recording. Comparison between awake and anesthetized conditions, as well as cortical depth were made between animals, because not all mice were used in each specific condition.

Results

Looking at the averaged responses to whisker stimulation (Fig. 2.2), some immediate differences are visible. First, GCaMP6f responses are very large during wakefulness, but nearly non-existent during anesthesia. Additionally, in the GCaMP6f traces during wakefulness, there is a separation between the traces taken at 150 - 300µm deep, and those in layer 1. The deeper responses are sharper and show a much larger change in fluorescence. The overall change may be due to extra fluorescent structures being present in deeper areas (thicker dendritic shafts, soma being present), but that does not explain the change in response shape. Looking at the VSD responses, there are also obvious changes between awake and anesthetized conditions, but they are different than the changes recorded in GCaMP6f. Anesthetized recordings with the VSD result in a larger overall depolarization, however the response shape shows two defined peaks, and the early but smaller peak is larger in the awake conditions.
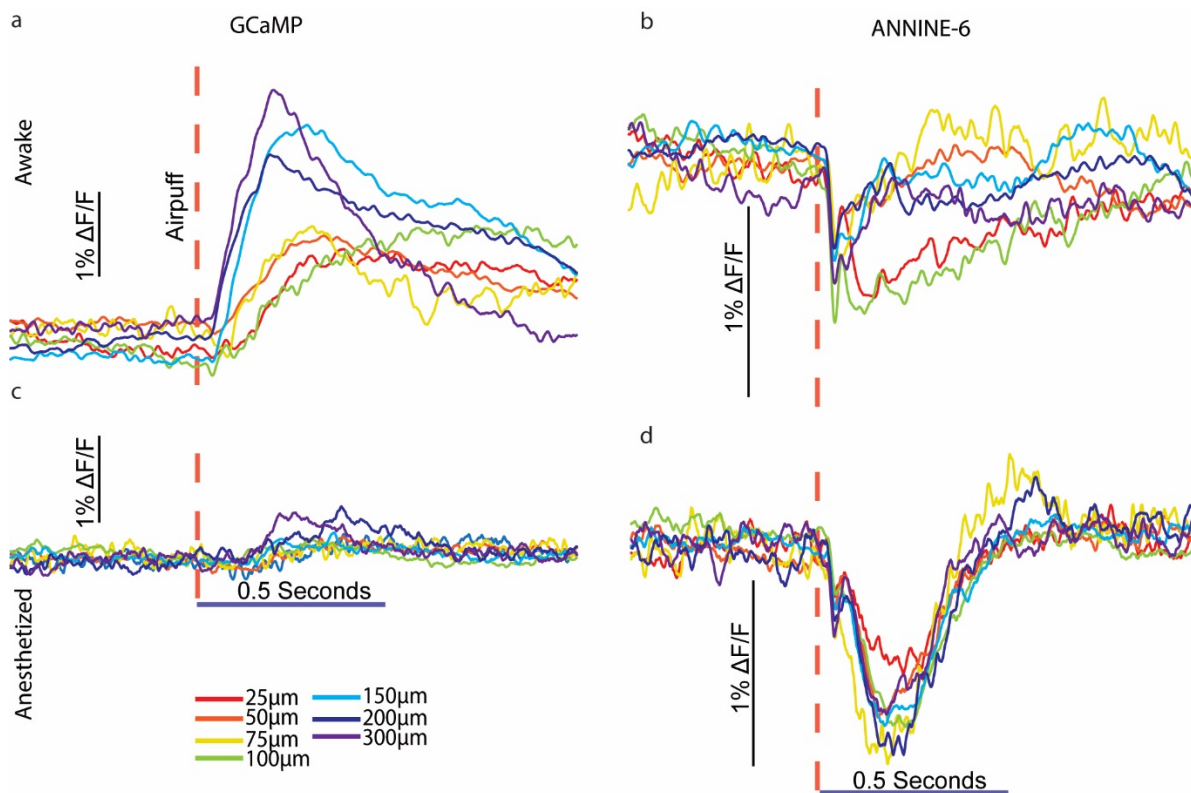
Figure 2.2. Averaged response traces for GCaMP6f (**a**, and **c**), and VSD (**b**, and **d**). Awake responses are shown above (**a**, and **b**), and anesthetized responses are shown below (**c**, and **d**). All traces are averaged around the air-puff delivery, marked by the dashed pink line. This line is placed by the electrical onset of the air-puff, but an additional 20-30ms of travel time between the valve opening and the air hitting the whiskers is needed to take into consideration. All traces show depolarization (ANNINE-6 when extracellular has a negative fluorescence change during depolarization), and are separated by cortical depth (indicated by color). The VSD traces (**b**, and **d**) show a biphasic peak, with a fast component being very sharp, and larger in the awake condition. The late peak is larger in the anesthetized condition. GCaMP6f (**a**, and **c**) show a single peak, which is nearly non-existent under anesthesia, but very prominent during wakefulness. Some separation can be seen between depths in the GCaMP6f awake traces.

At a glance, it is difficult to say if there is an effect that cortical depth has on VSD response size, although the early peak in both awake and anesthetized does suggest there might again be larger responses in deeper areas. Looking further into these early response peaks, a significant difference was found (tested at 95% confidence, two-tailed t-test, paired for depths, $p = 0.047$) between the awake and anesthetized peaks, with awake being larger. Differences in depth across a cortical state (awake, anesthetized) could not be confirmed. The early peak detected in the VSD was calculated to have a latency of approximately 10 to 20ms, after correcting for the travel time of the air in the air-puff delivery tube. This is in line with

previous findings in barrel cortex (Constantinople and Bruno, 2013), although slightly on the long side.

Early Peak Response in VSD
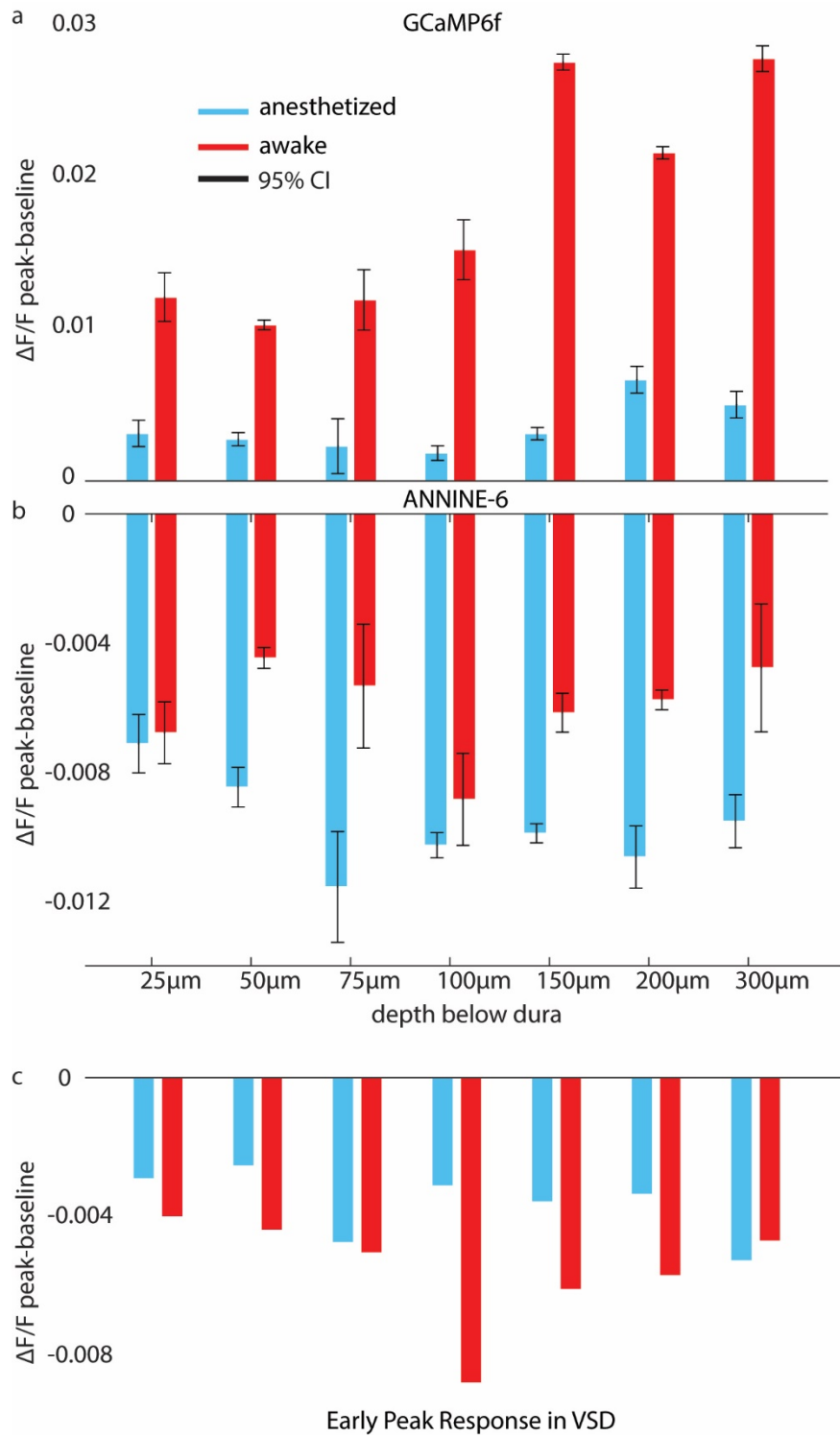
Figure 2.3 (previous page). Maximum depolarization for GCaMP6f (a) and VSD (b) averaged recordings. The black error-bars indicate 95% confidence intervals. GCaMP responses show a significant difference between anesthetized and awake recordings. VSD responses also show some difference between the two conditions, but are less pronounced. GCaMP also has a significant increase in peak in 150, 200, and 300μm depths, during wakefulness. The early peak in the VSD recordings are also quantified (c), calculated in the same way as (b), but limited to the first 55ms after the stimulation is triggered

Figure 2.3 shows the greatest extent of each peak in Figure 2.2, for both GCaMP6f and VSD responses. Here it is possible to see the significant difference between every awake GCaMP6f response and the response in the same depth during anesthesia. Additionally, there is no significant difference between GCaMP6f awake responses in 25, 50, 75, and 100μm, but 150, 200, and 300μm are significantly larger than them. In voltage, anesthetized responses are either significantly larger (50, 75, 150, 200, 300μm) or showed no significant difference (25, 100μm) with their awake counterpart. There seems to be a trend of increasing voltage response in anesthetized conditions in the first few depths recorded, with 25, and 50μm showing significantly smaller depolarization. This trend does not seem to keep with the awake responses.

Averaged LFP During Stimulation

ΔI/I = 3%

0.5 seconds
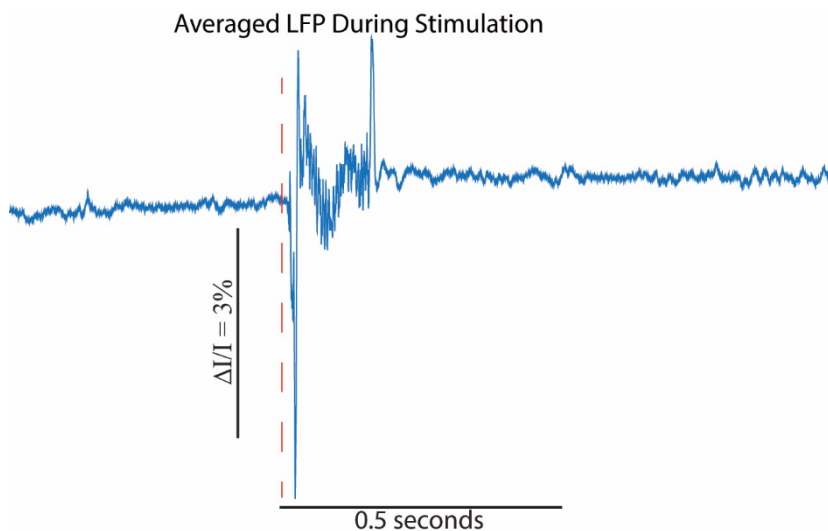
Figure 2.4. Averaged LFP during stimulation period, (indicated by dashed red line), in one animal (540 averaged trials, two stimulations per trial). The stimulation is triggered at time 0, but takes some time to reach the mouse, making an eventual latency of response of approximately 10ms. The LFP was placed between 350 and 450μm below the dura. Units are expressed as change in current/baseline current. LFP currents were recorded between 10 and 200 pA, converting to 0.1-2 mV with a 10 MΩ tip resistance.

I also created an average LFP recording from a single animal's recordings, to compare with the averaged VSD and GCaMP6f recordings (Fig. 2.4). The LFP shows a short latency negative current, and then a longer, slower positive current. Differences between this and the VSD are in line with previous research (Jin

et al., 2002). Artifacts may be present in the LFP signal as the air-puff turns on and off, creating sharp edges to the average signal. Between the sharp edges however, a bi-phasic signal, similar in shape to those showing N1 and P1 signals (Cauller, 1995). As the LFP shows changes in current, this is effectively the first derivative of average membrane potential, and in this way relate well to the recorded VSD signals.

Next I looked into whether any cortical oscillations could be detected in our data from the VSD. Resulting frequency spectra were calculated for each depth recorded, and in the same cortical states (Fig. 2.5). From these, it is immediately obvious that several peaks are present, and that these peaks change with cortical state very dramatically. A theta (4 - 10Hz) peak is very pronounced during the light anesthesia, in all cortical depths, although especially around 200μm.

 Smaller peaks were also seen occasionally in the lower beta rhythms (beta going from 10 – 30Hz), and a gamma peak was seen in both awake and low-anesthesia (gamma is 30 Hz and up). This gamma peak appears much larger in awake conditions than anesthetized (indicated
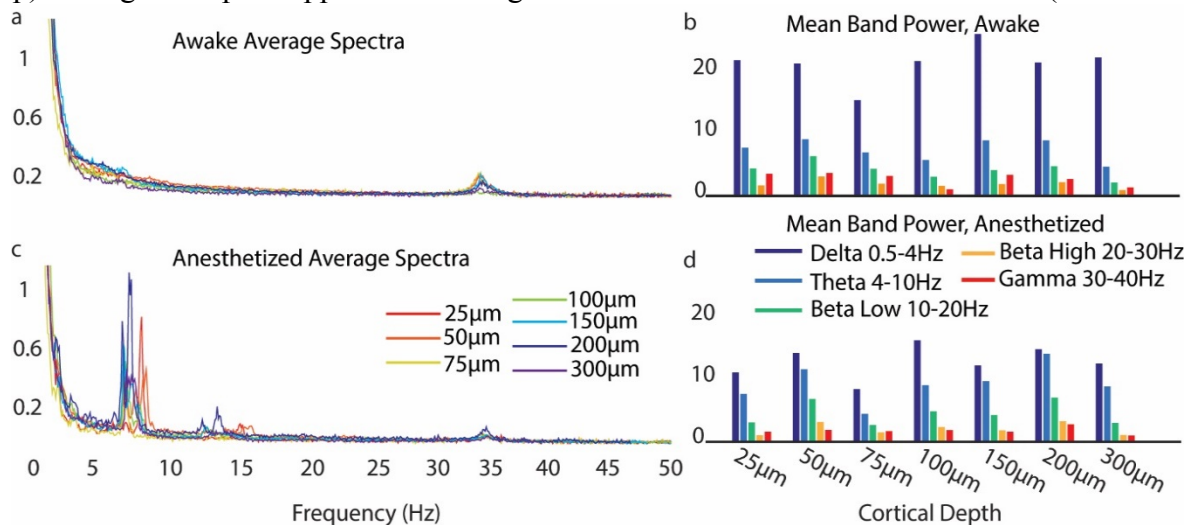
Figure 2.5. Full time course average spectra (a, and c), with corresponding bar graphs (b, and d) of power for each defined frequency band (bands defined by color. Dark blue – 0.5 to 4Hz, light blue – 4 to 10Hz, green – 10 to 20Hz, yellow – 20 to 30Hz, and red – 30 to 40Hz). Awake recordings are above (a, and b), while anesthetized recordings are below (c, and d). Data were generated with 2kHz recording rate, and 11 seconds recording time. The awake spectra (a) show marked differences to the anesthetized (c). The awake spectra show a defined 35Hz peak, larger than the same peak in the anesthetized recording. Theta peaks (4 – 10Hz) exist to a much greater extent under anesthesia than during wakefulness.

by 'Gamma, in Fig. 2.5 b and d). In this data, there doesn't appear to be a strong trend in any frequency band, relating to cortical depth.
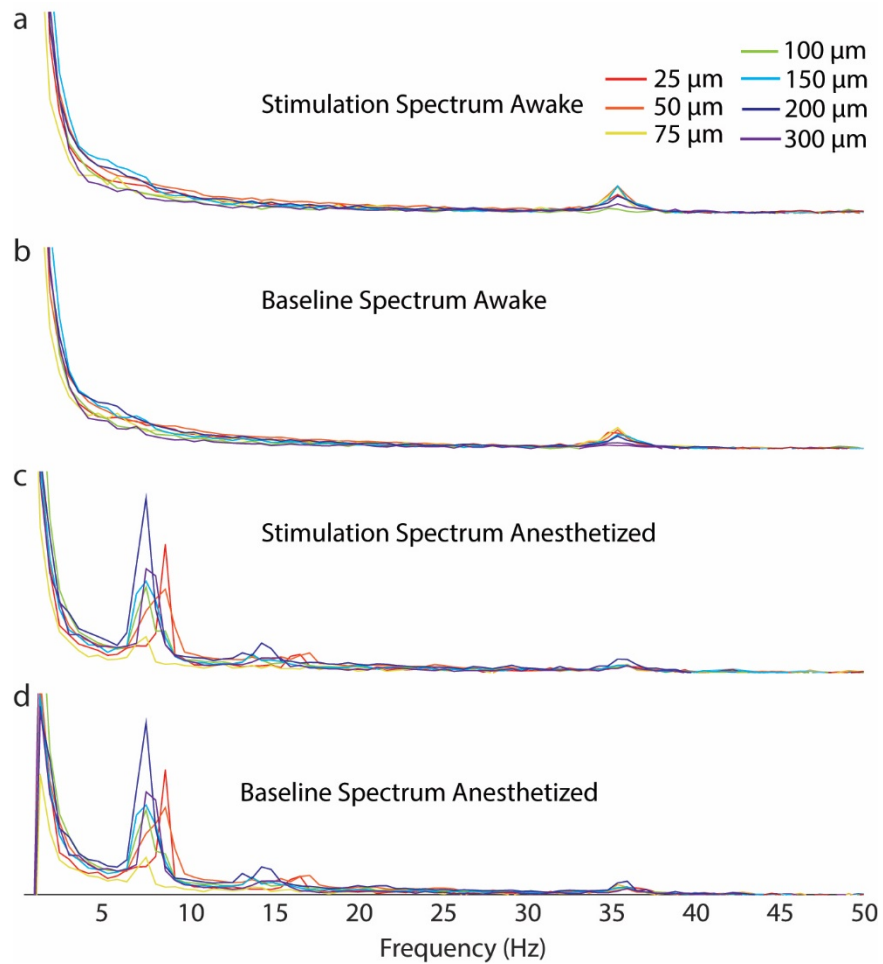
Figure 2.6. Frequency spectra for stimulation (a, and b), and baseline (c, and d) periods (stimulation period is 0.25 seconds before stimulation, 1.5 seconds following stimulation, baseline is 1.75 seconds with no stimulation period overlap), for awake (a, and b), and light anesthesia (c, and d). Colors indicate cortical depth. Notable differences between stimulation and anesthetized spectra show in the theta peaks (4-10Hz), beta activity (10-20Hz), and gamma (30+ Hz). The gamma peak also becomes more prominent during awake periods, compared to light anesthesia. These spectra contain fewer time points than the full spectra in figure 4, as these are generated from 3,500 time points, rather than the 22,000 in the previous spectra.

The next analysis I looked at was whether separating the time series recorded into times around air-puff delivery (stimulation), or times further from air-puff delivery (baseline) produced different oscillation powers (Stimulation periods defined as 0.25 seconds before stimulation, and 1.5 seconds following stimulation. Baseline defined by three periods of 1.75
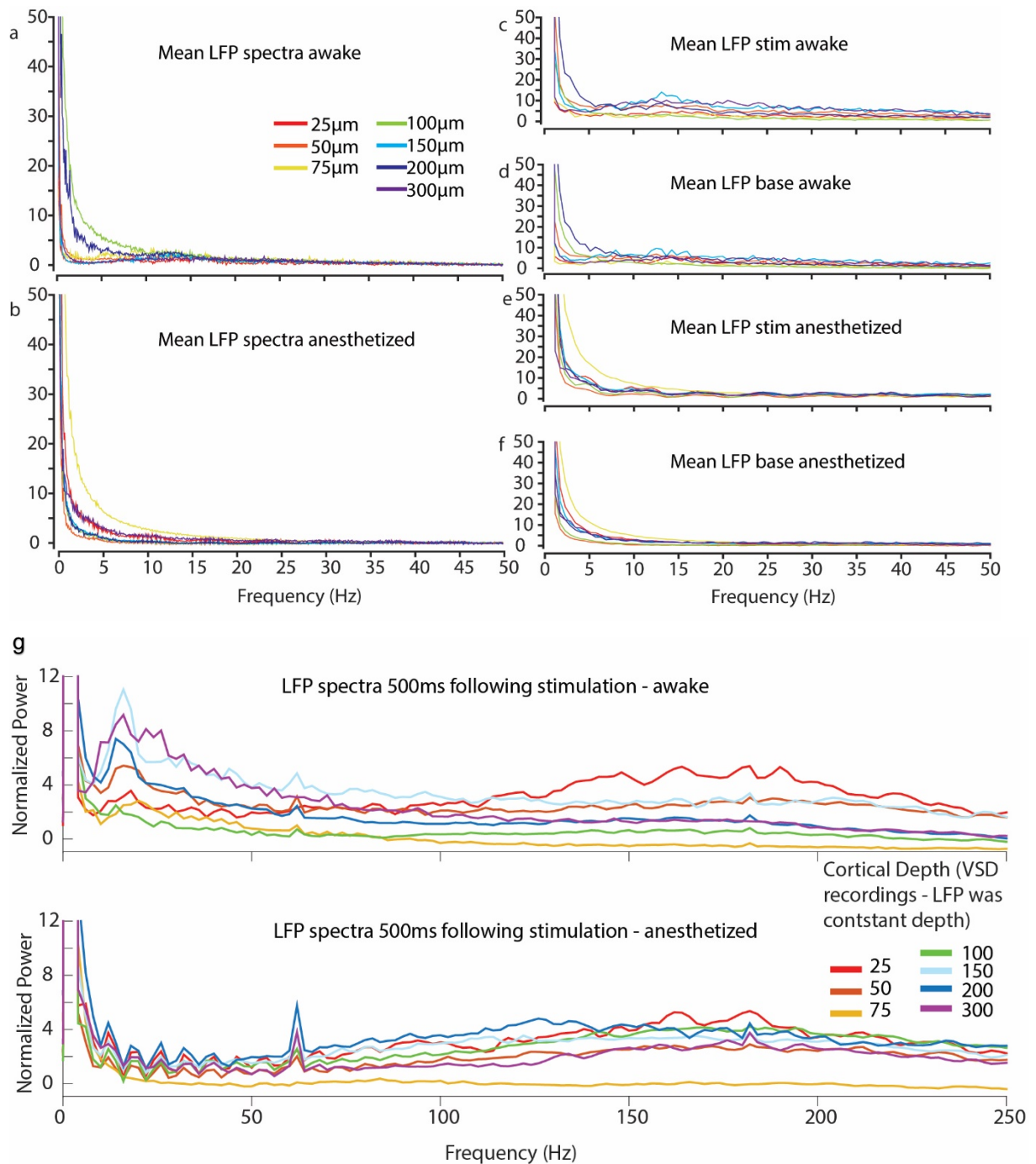
Figure 2.7. LFP frequency spectra averages for the same periods as figures 3.5 and 3.6. Total averages including stimulation and baseline periods (**a,** and **b**) are separated by 'depth' of where the VSD activity was recorded. The LFP was not moved however, so changes are from shifting cortical state. Graphs **c** through **f** are separated into stimulation and baseline periods, using the same time blocks as figure 3.6. Again, the LFP was kept at a constant depth, so changes with cortical depth (set by where the VSD recording was made) are due to a change in cortical state.

Figure 2.7. (Continued). The LFP following stimulation was isolated down to 500 ms and spectra were plotted (**g**). These show a noticeable increase in beta and gamma following stimulation, especially in the awake case. Note that 60 Hz is included, where an artifact can be detected.

seconds, one at the start of each trial, one following the first air-puff by 3 seconds, and the third following the second air-puff by 2.25 seconds). The averaged frequency spectra for these periods can be seen in Figure 2.6. The most noticeable change in powers can be seen
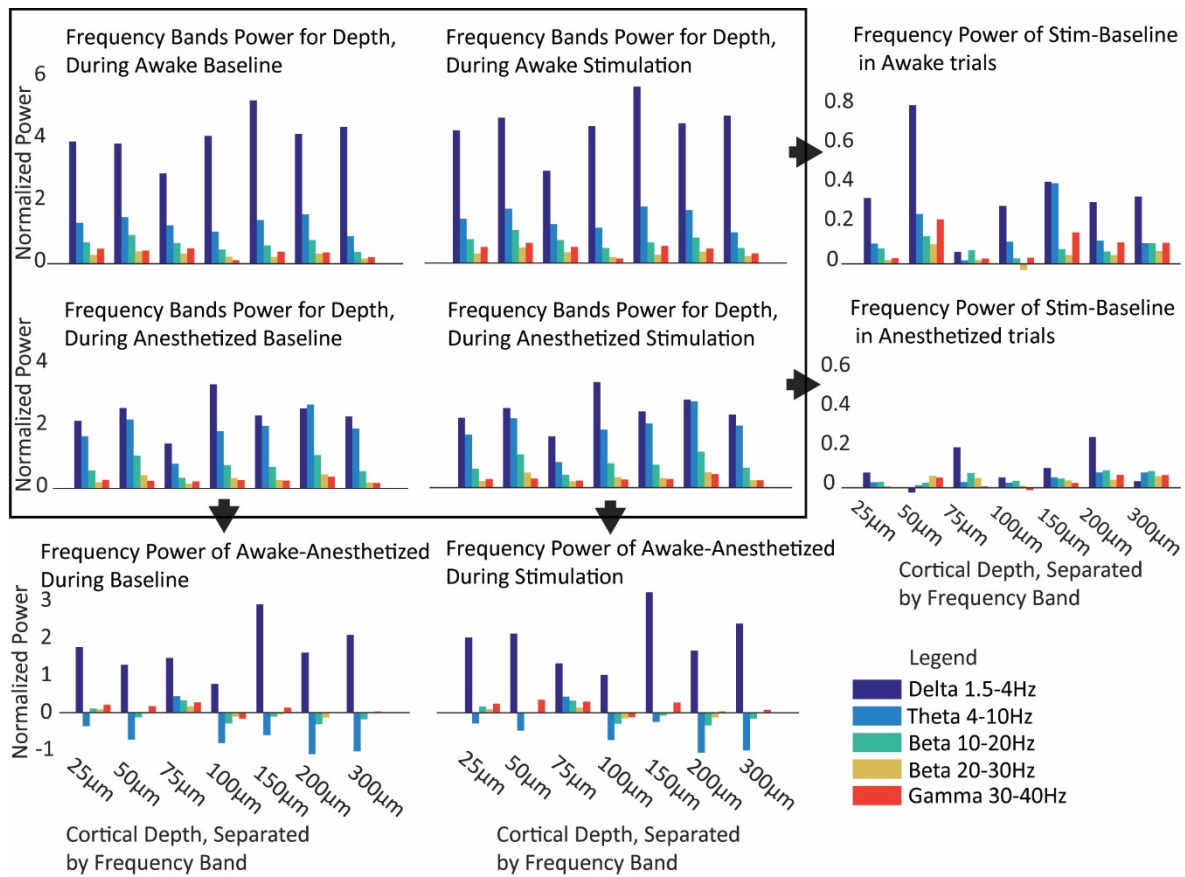
Figure 2.8. Bar graphs of frequency band power, for depths. Band power was calculated by the integral of the spectra, over the frequency band. The first four graphs (inside the box) are from the spectra presented in figure 3.6 – awake, and anesthetized stimulation, and baseline periods. The graphs on the outside of the box are the subtractions of either baseline periods from stimulation periods, in awake and anesthetized conditions (graphs on the right), or anesthetized from awake conditions, in stimulation or baseline periods (bottom graphs). Colors indicate the frequency band. It is worth remembering that power of each band decreases with frequency (see figures 3.5 and 3.6), so the gamma response being of the same magnitude as beta and theta changes, suggests a larger relative gamma response than the relative theta and beta responses.

in the awake conditions, in the 35Hz peak, which becomes more pronounced during stimulation.

To further look into power changes during stimulation, frequency bands were defined – delta 0.5 to 4Hz, theta 4 to 10Hz, low beta 10 to 20Hz, high beta 20 to 30Hz, low gamma 30 to 40 Hz, and higher gamma 40 to 50 Hz (high gamma in literature is higher than this. These terms only apply to the splits I am making in our data, not to previous studies of 'high gamma'), and the average power of each of these bands was calculated (integral of the frequency band).

These are displayed in bar graphs in Figure 2.8. Additionally, the differences between states were also calculated, as stimulation-baseline periods in awake and anesthetized conditions, and awake-anesthetized conditions in stimulation and baseline periods. Of note, delta is larger in every single subtraction, meaning it is stronger in awake, and stimulation periods.

Lower gamma (higher gamma not displayed in Fig. 2.8) shows a robust response to stimulation in the awake condition that is nearly wiped out under light anesthesia. Theta shows the only consistent decrease in power in the awake conditions, compared with anesthesia. This is consistent across stimulation and baseline periods, but perhaps slightly stronger during baseline. There again does not appear to be a strong trend in any band strength with cortical depth in this data.

Comparing the spectral data taken with VSD with the LFP, during the same time periods, reveals some important differences (Fig. 2.7). The LFP was kept in the same location for each recording, while the VSD recordings were made at different cortical depths. Thus, changes in LFP recordings at different cortical depth periods (as recorded by VSD) indicate that the cortical state was varying. This is obvious in the awake recordings for the LFP (Fig. 2.7**a**), where the delta range of frequencies are very different for each cortical depth period. The LFP also shows only one major frequency response to whisker stimulation (Fig. 2.7 **c**), which occurs during wakefulness, but not anesthesia. The beta range (10 – 30 Hz) shows a wide band increase in power, following stimulation, compared with the awake baseline periods. No noticeable peak in gamma is present, nor does it noticeably increase following stimulation, unlike the VSD recordings. Delta power also looks more consistent between stimulation and baseline, in contrast with the increases seen in the VSD recordings (Fig. 2.6, fig. 2.8). When the LFP is isolated down to 500 ms following the air-puff stimulation, there

is a stronger beta, and gamma power increase detected. The beta activity in the awake cases is much stronger than during baseline, or the 1.5 second period used for the other LFP spectra. The gamma power increases in a broad band, in particular with some very high frequency components above 100 Hz, in both the anesthetized and awake conditions.

To quantify crossover from GCaMP6f into the VSD channel, a two-photon image was recorded in a mouse with only GCaMP6f in its layer 2/3 cells, and no red dyes present (Fig. 2.9.). The same recording procedures were used as when recording the functional data presented here (SEMROCK filter used, PMTs set to 650, laser power adjusted for intensity of image). The GCaMP6f channel was approximately four times larger in intensity than the recorded cross-over into the red channel. All the structures seen in the green (GCaMP6f) channel were present, just dimmer, in the red channel.

In summary, layer 1 and deeper areas show differences in calcium activity (Fig. 2.2, **a**), but the average membrane potential of these areas does not show the same difference (Fig. 2.2, **b** and **d**). Calcium activity reduces to almost nothing during anesthesia (Fig. 2.2, c), but the membrane potential of the same areas show the largest recorded depolarization (Fig. 2.2, **d**). The average membrane potential also shows a biphasic response, with a fast and slow component (Fig. 2.2, **b** and **d**). In terms of oscillations, gamma (35Hz) is detected in all depths recorded, including layer 1 (Fig. 2.5, and 2.6 **a**, and **b**). Gamma, delta, and theta all show some responsiveness to whisker stimulation (Fig. 2.6, **a**, and **b**, Fig. 6). Power tends to decrease with frequency (Fig. 2.5 and 2.6), so similar magnitude changes in gamma, compared to theta, and beta, suggest a larger relative change in gamma than theta or beta.

Discussion

Comparing the LFP signal (Fig. 2.4) to the VSD response (both awake and anesthetized), differences are obvious. The LFP signal starts very sharply, has a uniform depolarization for about 150ms and then quickly switches off. As an LFP records changes in current (or voltage), it is effectively a first-derivative of the average membrane potential. A sharp negative, followed by a positive current indicates ion flow accelerating and then decelerating, but always flowing. In this way, following the LFP shape (Fig. 2.4), it compares well to the recorded VSD shape and timing (Fig, 2.2). The LFP however starts approximately 10 ms before the first depolarization starts in the VSD, which could be conduction time, but more

likely represents an artifact from the air-puff. The air-puff is likely moving the pipette very slightly, causing the sharp edge of the signal in figure 2.4, and then switching off, causing the other sharp edge at end of the signal in figure 2.4. The actual start of current flow in the LFP is likely masked by this artifact and of a very similar timing to the VSD (Fig. 2.2). The resulting LFP signal shape would be similar to those shown in (Cauller, 1995), with an N1 and P1 component. These shapes can be seen between the two sharp edges in figure 2.4. Considering these responses, it is important to consider the anatomy and physiology of the upper cortical layers, in barrel cortex. Input into barrel cortex comes in two separate pathways from the thalamus (Bruno and Sakmann, 2006; Clascá et al., 2012; Constantinople and Bruno, 2013; Zhang and Bruno, 2019), and then also from neighboring cortical areas (Rubio-Garrido et al., 2009). The mixing of a direct signal, and an indirect slower signal, may explain the bi-phasic peak seen in the voltage response (Fig. 2.2, **b** and **d**). The fast component is similar in latency to the fast responses recorded previously by electrodes in barrel cortex (Constantinople and Bruno, 2013), while from previous voltage imaging studies, we know that depolarization of the cortex spreads dramatically from within a barrel, to neighboring barrels quickly after whisker stimulation (Petersen et al., 2003). The reason that the bi-phasic peak has not been seen before, to the best of our knowledge, may be that optical sectioning is required in order to detect it. If an electrode was used, any signal from larger depolarization further away may mix into the recording, smearing the early peak into the late. Similarly, with previous voltage imaging studies, two-photon microscopy has rarely been used, and when it has, whisker responses have not been extensively averaged. Another explanation for the bi-phasic peak is that there is an axonal component, and then a dendritic component to the signal, similar to what has been seen historically in LFP recordings (Kublik et al., 2001). I do not believe this to be the case however, as the latencies are too long in this study to be explained by for example, thalamic axons as an early peak, and then a 10ms delay before the pyramidal cell dendrites begin to depolarize. Another reason I feel this explanation is not appropriate is that VSDs have been previously theorized to mainly show dendritic activity (Petersen et al., 2003; Kuhn et al., 2008), with axonal activity needing to be extraordinarily strong before it is detected by a VSD. Finally, that there is an increase in the size of the early peak in the awake condition, compared with light anesthesia, suggests that some signal at least comes from the secondary thalamus, if not the cortex, as these areas are more affected

by isoflurane than the primary thalamic nucleus – ventral posteromedial nucleus (Trageser et al., 2006; Zhang and Bruno, 2019).
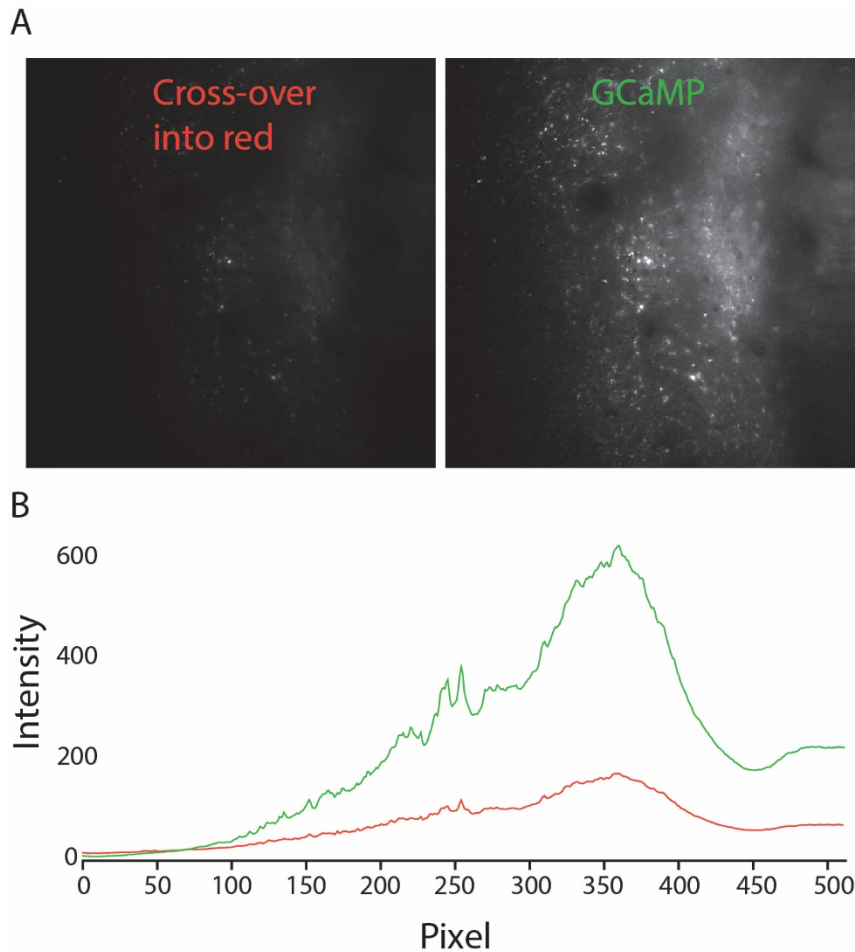
Figure 2.9. Cross-over of GCaMP6f into the red channel. GCaMP6f was recorded in a mouse' cortex, with no other dyes present (credit to Dr Claudia Cecchetto for the mouse). This is seen in **A**. Plots of these intensities across baseline pixels (x axis) are shown in **B**. GCaMP6f is approximately 4x higher in the dedicated green channel than the crossover into the red channel.

Seeing how the intracellular calcium activity shows very little response while under anesthesia, but the VSD shows a very large voltage change in the cells of that region, suggests anesthesia blocks the mechanism of layer 2/3 cells having a major calcium influx. This is consistent with previous work. Calcium influx into a pyramidal cell requires coincidence of somatic depolarization, leading to a back-propagating potential in the apical dendrite, meeting distal depolarization coming from layer 1 input (Schiller et al., 1998; Schiller et al., 2000; Larkum et al., 2004). This distal input in barrel cortex is strongest from the secondary thalamic nucleus – posterior medial nucleus (Zhang and Bruno, 2019), which is highly affected during anesthesia (Trageser et al., 2006; Zhang and Bruno, 2019). Together this would mean that cells in layers 1, 2, and 3 are all experiencing large depolarization, and are

possibly firing action potentials, but will not receive the distal input required to activate NMDA channels, and have a large calcium influx, under anesthesia.

Possible confounders of this theory, given the data presented here are that I cannot be certain that it is a thalamic input reduction that leads to the lack of calcium influx in anesthesia. It is possible that distant cortical areas feeding onto local cells are instead turned down during anesthesia. Additionally, this is based on the assumption that calcium influx in a pyramidal cell is caused by NMDA channel opening (Schiller et al., 1998; Schiller et al., 2000; Schiller and Schiller, 2001), however many distant neuromodulators reach the cortex, and they may also play a role, or isoflurane may directly affect pyramidal cells in some as yet unknown way.

A potential design limitation of the combined voltage and calcium imaging is that even though the VSD and GCaMP6f do not share a peak output wavelength, with enough brightness from one or the other, signals can leak across into the other channel (figure 2.9). Even using a very high quality filter set, with no overlap between channels, some brightness especially from the GCaMP6f signal, may have leaked into the VSD channel. I tried to get around this problem by excluding data that showed obvious leak, but given that the two depths that showed the least calcium activity while awake (25 and 100µm – Fig. 2.2a) also show the largest VSD depolarization (Fig. 2.2b), suggests some contamination still exists in the late VSD peak. Part of this problem is that depolarization in GCaMP6f leads to an increase in fluorescence, but leads to a decrease in extracellular ANNINE-6, so the two signals move in opposition to each other. Some computational deconvolution of the signals may be possible to further remove the GCaMP6f from the VSD, but I did not want to introduce any artifacts, or present an artificially high VSD signal.

Potential cross-talk contamination can be examined in Figure 2.3, during the awake responses. As calcium response increases with cortical depth, the late VSD response mirrors it, which results in a decreased recorded voltage response. This is unlikely to be a physiological response, as higher calcium influx recorded would suggest a stronger, or more coherent depolarization across recorded cells. The early response however is too fast to be influenced by the slower-rising GCaMP signal. In this case, the awake response still shows a very large response at 100µm, but in general the responses from 100µm and deeper are

larger than those before. This trend is very weak however, and not necessarily present in the anesthetized early responses. Together, this suggests that voltage depolarization, as a measurement of average membrane potential, is less depth dependent than calcium influx. As the VSD measurement records the averaged depolarization of all cells being scanned, this suggests that the coherence of the depolarization does not massively change within the supra-granular layers.

Looking at the LFP spectral analysis, it is evident that the cortical state of the animals were varying beyond just anesthetized and awake, even after removing files with excessive movement. Qualitatively, there appears to be less variation in spectra during anesthesia (Fig, 2.7 **b**), than during wakefulness (Fig. 2.7 **a**), which is understandable. The anesthesia controls and limits the cortical states that can occur, while wakefulness means the animal could be experiencing anything from quite restfulness, to being fully alert. The LFP data also shows a simple increase in beta (10 – 30 Hz) band power (Fig. 2.7 **c**), primarily during wakefulness. This is in line with previous recordings made in barrel cortex during whisker stimulation, in layer 2/3 (Deneux and Grinvald, 2016). Others have reported beta increases in deeper areas and delta increases in the upper cortex (Sun and Dan, 2009), although this was using rats and looking at visual cortex and visual stimulation, rather than barrel cortex and whisker stimulation. The LFP in my work was consistently placed around 400μm deep into the cortex, so may be picking up a mix of layer 2, 3, 4, and 5. Despite this, I do not detect a gamma peak, or large delta shift following stimulation, suggesting these are either only in the upper cortical areas, or more likely, require some more local recording technique, like two-photon recordings.

To the best of my knowledge, this is the first published case of neural oscillations being recorded with a voltage dye and two-photon scanning. To this end, comparisons need to be made from this data to previous data recorded using either electrodes, encephalograms, or wide-field voltage imaging. Because our technique is new, I cannot be certain exactly how results from previous work relate to the recordings made here.

Of note, I recorded oscillations in cortical layer 1, which I do not believe has been done before. I have found noticeable peaks in the delta (0 - 4Hz), theta (4 – 10Hz), beta (10 – 30Hz), and low gamma (30 – 40Hz). I believe further oscillations should exist at higher

frequencies, but our recording method was not optimized enough to collect signals at such a small signal to noise ratio. While some of the lower frequency oscillations are less surprising, as they have large power and cover larger areas (Buzsáki and Draguhn, 2004), the presence of even low gamma was not a given. Gamma is thought to be generated by interactions between excitatory neurons, primarily pyramidal, and fast spiking interneurons (Bartos et al., 2007; Buzsáki and Wang, 2012). It is theoretically possible to generate it with a network of fast spiking interneurons by themselves (Dumont et al., 2017), but areas of the brain were it has been found are areas with mixed populations (hippocampus, and cortex are primary areas of gamma research - (Buzsáki, 2009)). Layer 1 of the cortex is mainly a mix of axons and dendrites, with distant cells projecting and connecting there (Cauller et al., 1998; Rubio-Garrido et al., 2009; Narayanan et al., 2015). There are interneurons present, although relatively few of them (Gabbott and Somogyi, 1986), and none are thought to be fast-spiking (Rudy et al., 2011; Jiang et al., 2015). Work looking at all interneurons of the cortex, and reconstructing their projections (Jiang et al., 2015) show some fast-spiking basket cells project partly into layer 1. Their survey of all interneurons does not present how far up these cells project, or how frequently these cells were found. This does need to be taken into consideration though, that some fast-spiking interneuron axons exist in at least some depths of layer 1. Dendrites are primarily what a VSD signals (Petersen et al., 2003; Kuhn et al., 2008), so two possibilities emerge. Either the dendrites of deeper cells are coherent enough in their activity to show a slow gamma signal, or gamma is being generated locally by basket cells of layer 2 projecting onto the primary dendritic trunk of pyramidal cells from deeper layers. Dendrites in layer 1 barrel cortex are a mix of dendrites from layer 2/3 pyramidal cells, layer 4 stellate cells, layers 5 and 6 pyramidal cells, and more layer 2/3 pyramidal cells in neighboring barrels, and cortical areas. I cannot say what percentage of these cells need to be coherent for us to detect a 35Hz peak, but the fact that at least some are is very interesting.

Additionally, gamma increases in power in layer 1 when stimulation is given to the whiskers. This increase indicates that coherence in the gamma band is increasing during stimulation. I know from previous research that stimulation of whiskers recruits many cells in barrel cortex, starting within a column and then moving to neighboring areas (Petersen et al., 2003). Many of the cells recruited are pyramidal cells and their interneurons, so an increase in gamma during stimulation would be in line with this. An increase in gamma in layer 1 however,

suggests that the apical dendrites of the pyramidal cells carry the gamma frequency as well. This is potentially then shared with neighboring barrels which also received stimulation (the stimulation is an air-puff on all whiskers), and passed to more distant cortical areas also sharing this layer 1 area. The theory of communication through coherence by Pascal Fries (Fries, 2005; Bastos et al., 2015) posits that coherence in certain frequency bands can help pass neural information. This has been backed up by computational modeling (Dumont et al., 2017; Dumont and Gutkin, 2018), as well as some experimental data with induced oscillations (Sohal, 2012). The presence of gamma oscillations in layer 1, that also increase in power following stimulation may be further evidence of communication through coherence in neighboring cortical areas.

Supplemental Tables

Table 1. Stimulation – Baseline while awake and anesthetized. 95% confidence intervals are also presented, based on the baseline noise (defined at 50+Hz where there are no detectable peaks).

Table 2. Stimulation and Baseline band power, while awake. 95% confidence intervals are presented, based on standard deviation of the band power in each recorded trial.

Table 2. Stimulation and Baseline band power, while under light anesthesia. 95% confidence intervals are presented, based on standard deviation of the band power in each recorded trial.

Table 2.1. Cortical Depth and Frequency Band	Mean Integral of Frequency Power, While Awake, Stim - Baseline	± 95% C.I. Based on Baseline Noise	Mean Integral of Frequency Power, While Anesthetized, Stim - Baseline	± 95% C.I. Based on Baseline Noise
25μm				
Delta	0.3346	0.0033	0.0774	0.0010
Theta	0.1026		0.0275	
Beta Low	0.0795		0.0297	
Beta High	0.0186		0.0082	
Gamma Low	0.0297		0.0031	
Gamma High	0.0634		0.0081	
50μm				
Delta	0.8079	0.0060	-0.0238	0.0028
Theta	0.2538		0.0129	
Beta Low	0.1399		0.0247	
Beta High	0.0996		0.0605	
Gamma Low	0.2267		0.0514	
Gamma High	0.0479		0.0357	
75μm				
Delta	0.0602	0.0023	0.2057	0.0039
Theta	0.0175		0.0289	
Beta Low	0.0696		0.0750	
Beta High	0.0195		0.0494	
Gamma Low	0.0268		0.0067	
Gamma High	0.0015		0.0027	
100μm				
Delta	0.2946	0.0072	0.0521	0.0033
Theta	0.1128		0.0244	
Beta Low	0.0280		0.0347	
Beta High	-0.0318		0.0105	
Gamma Low	0.0312		-0.0119	
Gamma High	-0.0203		-0.0150	
150μm				
Delta	0.4184	0.0059	0.0999	0.0046
Theta	0.4104		0.0524	
Beta Low	0.0748		0.0470	
Beta High	0.0448		0.0367	
Gamma Low	0.1606		0.0238	
Gamma High	0.0415		0.0361	
200μm				
Delta	0.3149	0.0020	0.2585	0.0072
Theta	0.1177		0.0779	
Beta Low	0.0627		0.0889	
Beta High	0.0449		0.0407	
Gamma Low	0.1092		0.0652	
Gamma High	0.0633		0.0726	

| Table 2.1. Cortical Depth and Frequency Band	Mean Integral of Frequency Power, While Awake, Stim - Baseline	± 95% C.I. Based on Baseline Noise	Mean Integral of Frequency Power, While Anesthetized, Stim – Baseline	± 95% C.I. Based on Baseline Noise
300μm				
Delta	0.3420	0.0086	0.0328	0.0056
Theta	0.1047		0.0781	
Beta Low	0.1053		0.0852	
Beta High	0.0646		0.0588	
Gamma Low	0.1065		0.0646	
Gamma High	0.1229		0.0438	

Table 2.2 Cortical Depth and Frequency Band	Mean Integral of Band Power, During Stim, Awake	± 95% CI	Mean Integral of Band Power During Baseline, Awake	± 95% CI
25µm				
Delta	4.2652	0.1846	3.9306	0.1655
Theta	1.4203	0.0094	1.3178	0.0087
Beta Low	0.7662	0.0039	0.6868	0.0034
Beta High	0.3042	0.0023	0.2856	0.0013
Gamma Low	0.5152	0.0076	0.4856	0.0077
Gamma High	0.0604	0.0015	-0.0030	0.0013
50µm				
Delta	4.6751	0.1501	3.8671	0.1224
Theta	1.7503	0.0094	1.4966	0.0085
Beta Low	1.0621	0.0034	0.9222	0.0033
Beta High	0.4976	0.0019	0.3979	0.0017
Gamma Low	0.6461	0.0081	0.4195	0.0056
Gamma High	0.0466	0.0018	-0.0014	0.0013
75µm				
Delta	2.9681	0.1620	2.9079	0.1539
Theta	1.2510	0.0145	1.2335	0.0145
Beta Low	0.7369	0.0052	0.6674	0.0032
Beta High	0.3438	0.0030	0.3243	0.0021
Gamma Low	0.5227	0.0118	0.4958	0.0096
Gamma High	-0.0131	0.0021	-0.0146	0.0019
100µm				
Delta	4.4074	0.1798	4.1128	0.1761
Theta	1.1390	0.0113	1.0262	0.0106
Beta Low	0.4858	0.0028	0.4578	0.0025
Beta High	0.1954	0.0017	0.2272	0.0016
Gamma Low	0.1427	0.0022	0.1115	0.0019
Gamma High	-0.0210	0.0015	-0.0007	0.0009
150µm				
Delta	5.6744	0.1904	5.2560	0.1907
Theta	1.8168	0.0175	1.4064	0.0128
Beta Low	0.6649	0.0032	0.5901	0.0029
Beta High	0.2654	0.0014	0.2206	0.0012
Gamma Low	0.5487	0.0083	0.3881	0.0052
Gamma High	0.0446	0.0019	0.0031	0.0016
200µm				
Delta	4.4953	0.1197	4.1804	0.1094
Theta	1.7041	0.0112	1.5864	0.0119
Beta Low	0.8221	0.0032	0.7594	0.0032
Beta High	0.3682	0.0015	0.3233	0.0013
Gamma Low	0.4729	0.0045	0.3637	0.0032
Gamma High	0.0583	0.0012	-0.0050	0.0011

Table 2.2

Cortical Depth and Frequency Band	Mean Integral of Band Power, During Stim, Awake	± 95% CI	Mean Integral of Band Power During Baseline, Awake	± 95% CI
300μm				
Delta	4.7399	0.2223	4.3979	0.2059
Theta	0.9873	0.0087	0.8827	0.0102
Beta Low	0.4828	0.0023	0.3776	0.0021
Beta High	0.2270	0.0015	0.1624	0.0013
Gamma Low	0.3124	0.0034	0.2059	0.0027
Gamma High	0.1187	0.0020	-0.0042	0.0012

Table 2.3.

Cortical Depth and Frequency Band	Mean Integral of Band Power, During Stim, Anesthetized	± 95% CI	Mean Integral of Band Power During Baseline, Anesthetized	± 95% CI
25μm				
Delta	2.2467	0.0967	2.1693	0.0976
Theta	1.7045	0.0612	1.6770	0.0734
Beta Low	0.6070	0.0077	0.5774	0.0694
Beta High	0.2063	0.0019	0.1982	0.1496
Gamma Low	0.2769	0.0032	0.2737	0.0715
Gamma High	-0.0009	0.0015	-0.0090	0.0529
50μm				
Delta	2.5572	0.0758	2.5810	0.0602
Theta	2.2299	0.0453	2.2170	0.0461
Beta Low	1.0721	0.0070	1.0474	0.0172
Beta High	0.4825	0.0023	0.4220	0.0441
Gamma Low	0.2954	0.0018	0.2440	0.0404
Gamma High	0.0331	0.0012	-0.0025	0.0617
75μm				
Delta	1.6481	0.0872	1.4424	0.0072
Theta	0.8190	0.0168	0.7901	0.0072
Beta Low	0.4124	0.0033	0.3374	0.0033
Beta High	0.2025	0.0021	0.1531	0.0060
Gamma Low	0.2284	0.0039	0.2217	0.0056
Gamma High	0.0047	0.0022	0.0019	0.0075
100μm				
Delta	3.3959	0.1446	3.3437	0.0019
Theta	1.8692	0.0436	1.8447	0.0026
Beta Low	0.7807	0.0059	0.7459	0.0023
Beta High	0.3416	0.0021	0.3311	0.0018
Gamma Low	0.2580	0.0032	0.2699	0.0014
Gamma High	-0.0186	0.0017	-0.0036	0.0017
150μm				
Delta	2.4479	0.0743	2.3479	0.0034
Theta	2.0620	0.0408	2.0095	0.0019
Beta Low	0.7382	0.0057	0.6912	0.0046
Beta High	0.3037	0.0018	0.2670	0.0025
Gamma Low	0.2749	0.0025	0.2511	0.0023
Gamma High	0.0360	0.0015	-0.0001	0.0030

Table 2.3. Cortical Depth and Frequency Band	Mean Integral of Band Power, During Stim, Anesthetized	± 95% CI	Mean Integral of Band Power During Baseline, Anesthetized	± 95% CI
200μm				
Delta	2.8313	0.0628	2.5728	0.0014
Theta	2.7753	0.0618	2.6974	0.0014
Beta Low	1.1597	0.0072	1.0709	0.0022
Beta High	0.4972	0.0017	0.4565	0.0015
Gamma Low	0.4406	0.0035	0.3754	0.0010
Gamma High	0.0699	0.0014	-0.0028	0.0010
300μm				
Delta	2.3494	0.0825	2.3167	0.0821
Theta	1.9960	0.0483	1.9180	0.0487
Beta Low	0.6412	0.0066	0.5560	0.0062
Beta High	0.2412	0.0022	0.1824	0.0018
Gamma Low	0.2403	0.0032	0.1757	0.003
Gamma High	0.0444	0.0018	0.0005	0.0012

Supplemental figures 2.1 Average stimulation response from each recording session selected for further averaging – 25 to 50 µm cortical depth
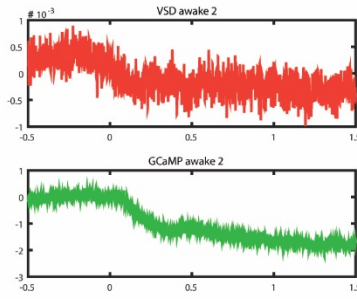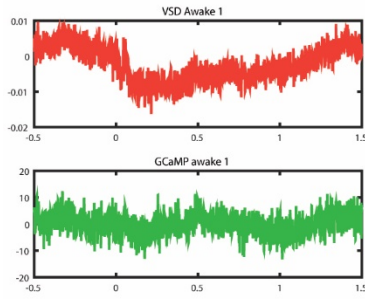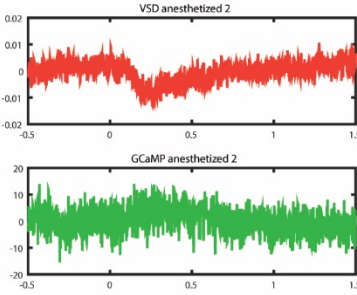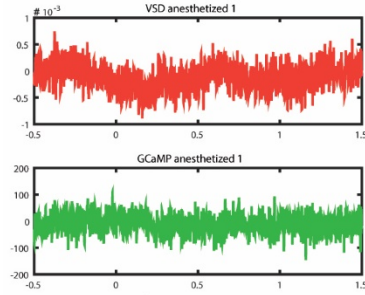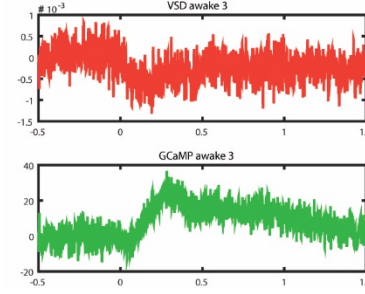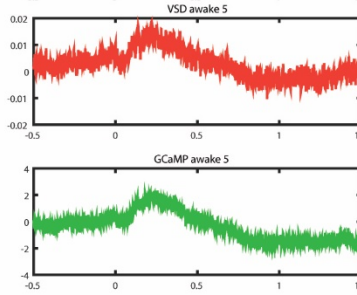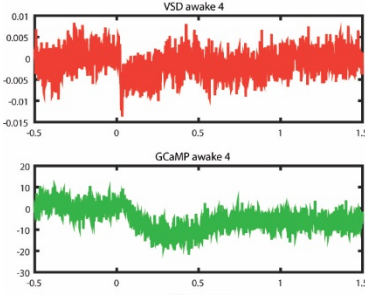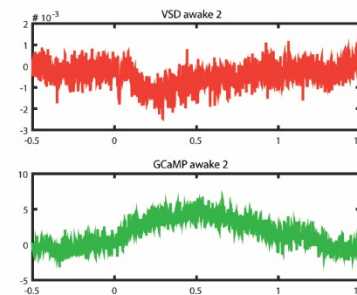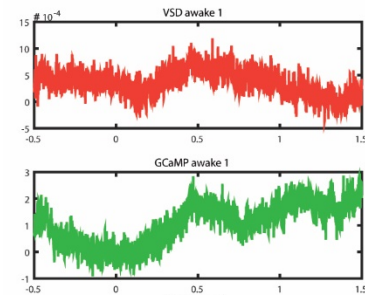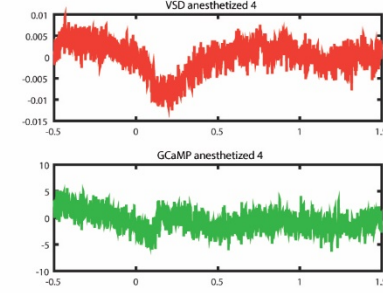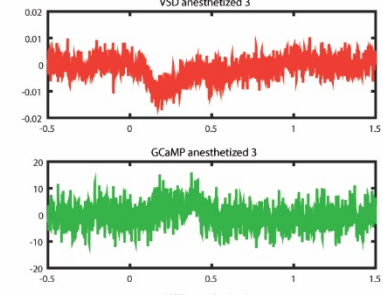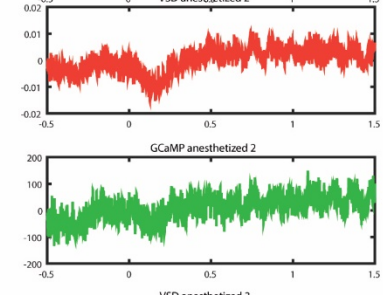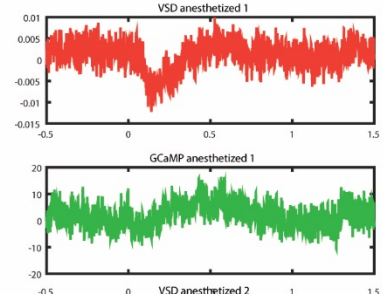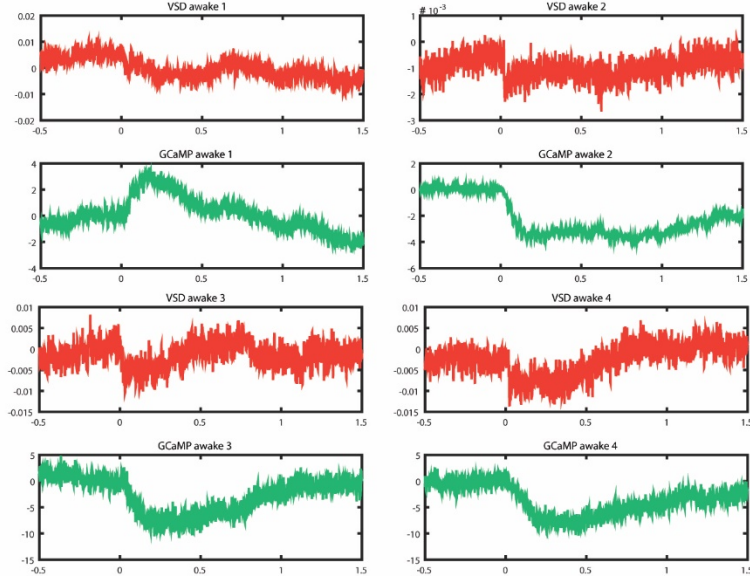
Supplemental figures 2.2 Average stimulation response from each recording session selected for further averaging – 75 to 150 µm cortical depth
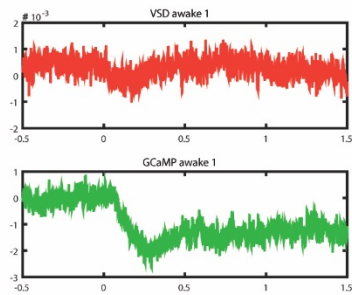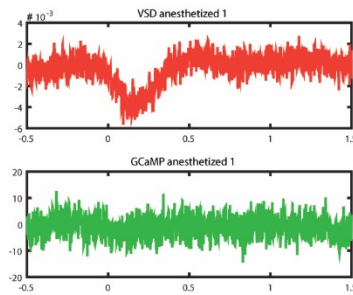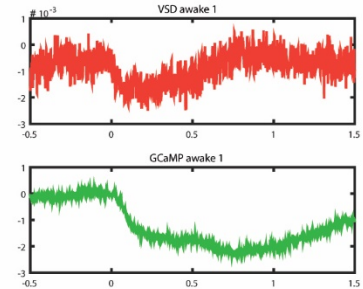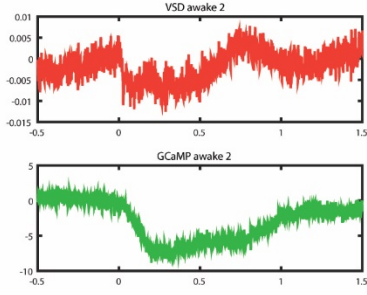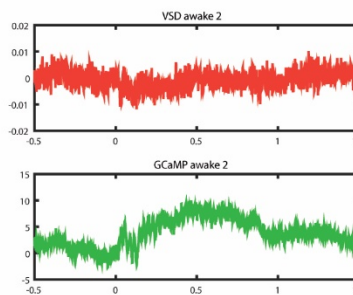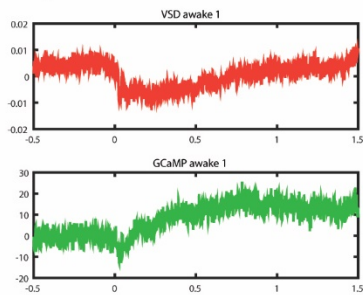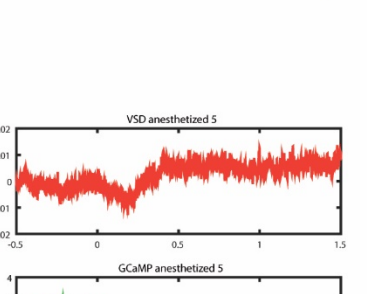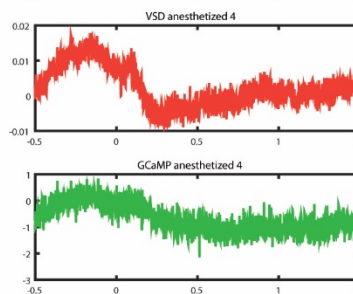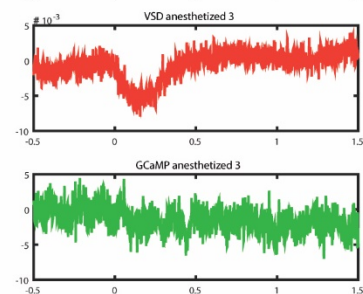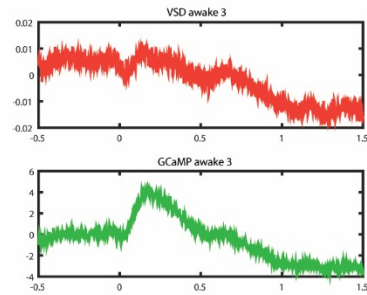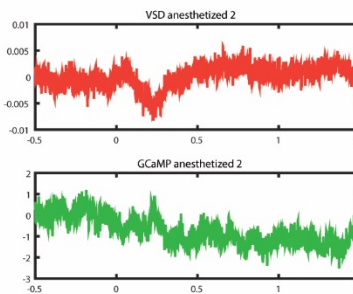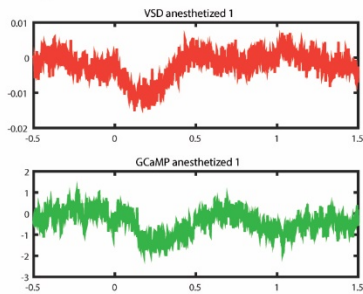
Supplemental figures 2.3 Average stimulation response from each recording session selected for further averaging – 150 to 200 µm cortical depth
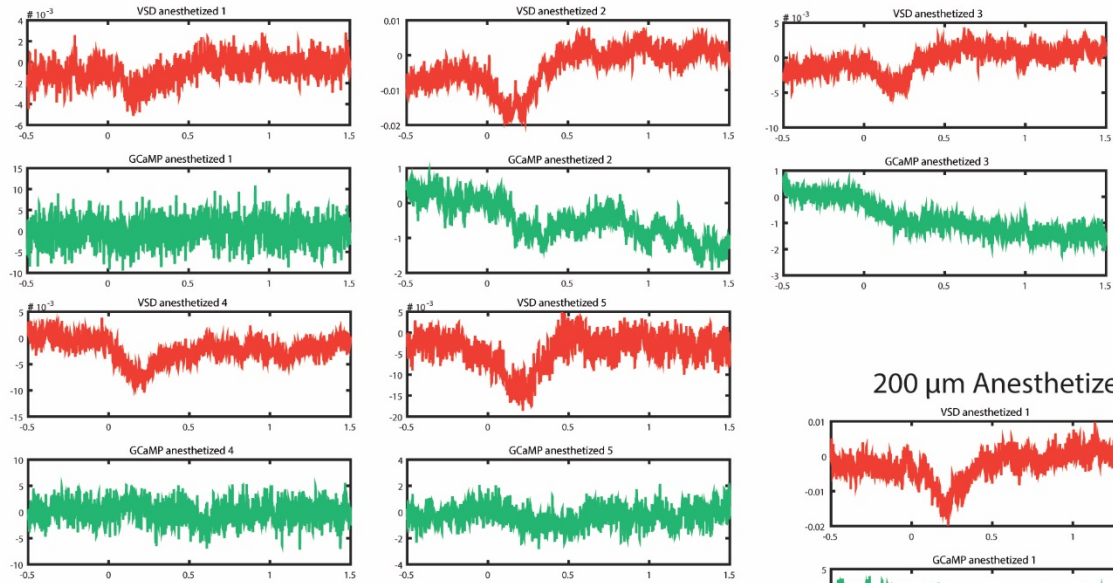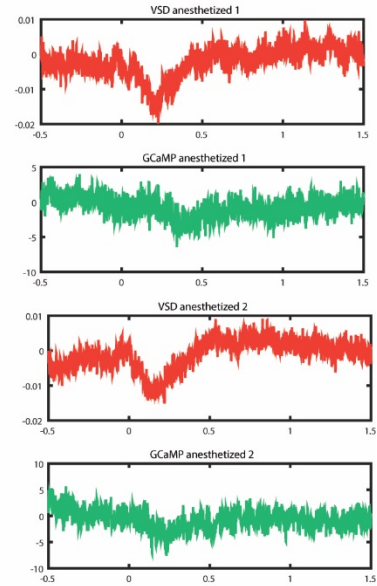
Supplemental figures 2.1 Average stimulation response from each recording session selected for further averaging – 300 μm cortical depth

300 μm Awake
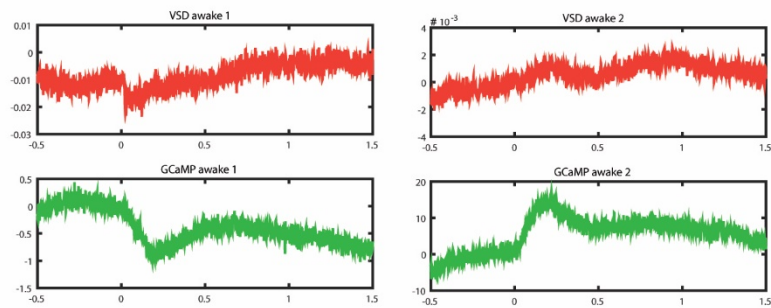
300 μm Anesthetized
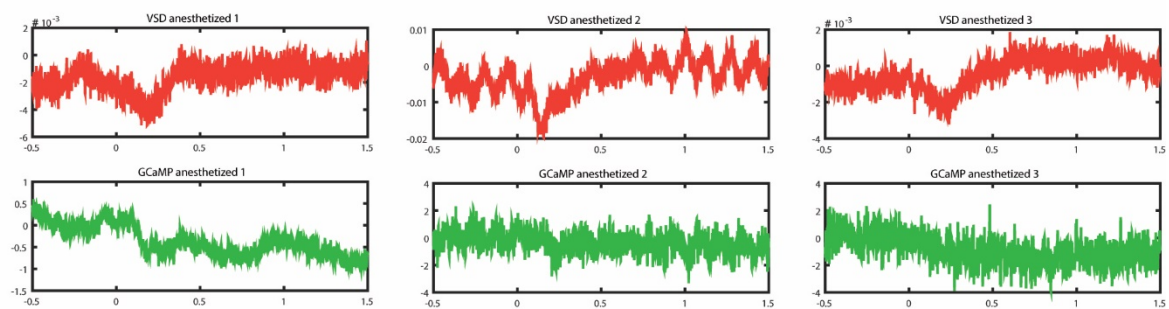
Chapter 3

Layer 1 Investigation: New Voltage Sensitive Dye and Application Method, for Highest Resolution of Neural Oscillations

Brief Outline

Understanding the role the upper cortex plays in sensory signal processing was the primary driving motivation for my research. In this way, researching the signal profile of whisker stimulation through layers 1, 2, and 3, was important. However, without understanding more about layer 1 activity, it is difficult to interpret the oscillation data collected. Voltage signals were slightly mixed with calcium signals, and the whisker stimulation added potential oscillations to the signals collected.

As recordings in layer 1 especially were still somewhat weak, I wished to increase the scope of layer 1 research here. Primarily, more oscillation data were needed, and at the highest fidelity I could possibly create. This involved removing the GCaMP6f from the experiment, as well as the whisker stimulation. Instead, layer 1 could be probed in its simplest state with just voltage dye, generating an uncomplicated data set of layer 1 activity, separated by depth and cortical state. This not only gave results without contamination from green GCaMP6f signals, but also allowed a conversion of fluorescence percentage change to millivolts (mV), giving the first (to my knowledge) voltage recording of dendritic potentials undergoing gamma oscillations.

Membrane voltage oscillations in layer 1 of primary sensory cortices might be important indicators of cortical gain control, attentional focusing, and signal integration. However, electric field recordings are hampered by the low seal resistance of electrodes close to the brain surface. To better investigate cortical Layer 1 function, we developed a new voltage sensitive dye, and surgery to apply it. DiMethyl ANNINE-6plus is derived from previous ANNINE family dyes, particularly ANNINE-6plus, but is more hydrophilic and thus easier to diffuse through cortical tissue. The bubble surgery lifts the dura from the cortex, in an open craniotomy, but leaves the dura intact. DiMethyl ANNINE-6plus can then be injected via micropipette into the space between the dura and cortex, so it can diffuse through the

upper cortical layers. This new dye, and surgical application provide an interesting approach to capturing cortical Layer 1 activity, which is inaccessible to calcium sensors, electrodes, and genetically targeted voltage indicators.

Introduction

Cortical Layer 1 is theorized to play a role in many important cortical functions, like attentional focusing (Noudoost et al., 2010), gain control (Larkum et al., 2004), and signal integration (Larkum et al., 2004). Recording from Layer 1 using traditional neuroscience approaches has been difficult so it follows that studying these functions is also difficult. Recording from layer 1 using traditional neuroscience approaches has been difficult, although some advances have been made with genetic fluorescent markers (Takata and Hirase, 2008; Lacefield et al., 2019), synthetic calcium dye (Helmchen et al., 1999), and electrode recordings plus pharmacology on the few cells that exist in layer 1 (Jiang et al., 2013; Egger et al., 2015; Jiang et al., 2015). Dendritic tufts in layer 1 have been recorded with an electrode in slice preparations, but the thinness of the dendrites limit how much of the cell can be probed (Larkum et al., 2009). Layer 1 has also been modulated and the effect on other cortical areas has been measured (Ibrahim et al., 2016; Mease et al., 2016). These current probes leave some activity uncollected, with genetic targeting only affecting certain cell populations in any given experiment, calcium reporting only a subset of neural activity, electrode recordings targeting only large enough structures to record from (and extracellular recordings in layer 1 being drowned out by signals from layer 2), and any manipulation in layer 1 has to be measured by downstream effects on the rest of the brain.

Synthetic VSDs have long been used for neural recording (Tasaki et al., 1968; Cohen et al., 1974; Grinvald and Hildesheim, 2004; Peterka et al., 2011), but a major issue surrounding them is the difficulty of application, especially for *in vivo* work. Additionally, camera imaging of VSDs lacks depth resolution, but two-photon microscopy can overcome this (Kuhn et al., 2008; Acker et al., 2016; Roome and Kuhn, 2018). The ANNINE family dyes (Hübener et al., 2003; Kuhn et al., 2004; Fromherz et al., 2008; Mennerick et al., 2010) are among the most sensitive, and reliable synthetic voltage dyes available, and are particularly sensitive under two-photon imaging (Kuhn et al., 2004; Fromherz et al., 2008), but remain very difficult to introduce into neural tissue. So far injection via micropipette into the brain,

or electroporation into a single cell (Kuhn et al., 2008; Roome and Kuhn, 2018) have been the methods of application for these dyes. Other voltage dyes have been topically applied to the brain (Orbach et al., 1985; Kleinfeld and Delaney, 1996; Petersen et al., 2003), or directly to the dura (Lippert et al., 2007), and then left to diffuse into the upper cortical layers, thereby staining tissue. However, after removal of the topically applied dye, the dye washes out quickly from layer 1 (typically 100 μm thick in mice) leaving the voltage signal coming from layer 2 and 3 (Kleinfeld and Delaney, 1996; Petersen et al., 2003; Lippert et al., 2007). This is a major disadvantage for those wishing to study Layer 1 of the cortex, which in mice
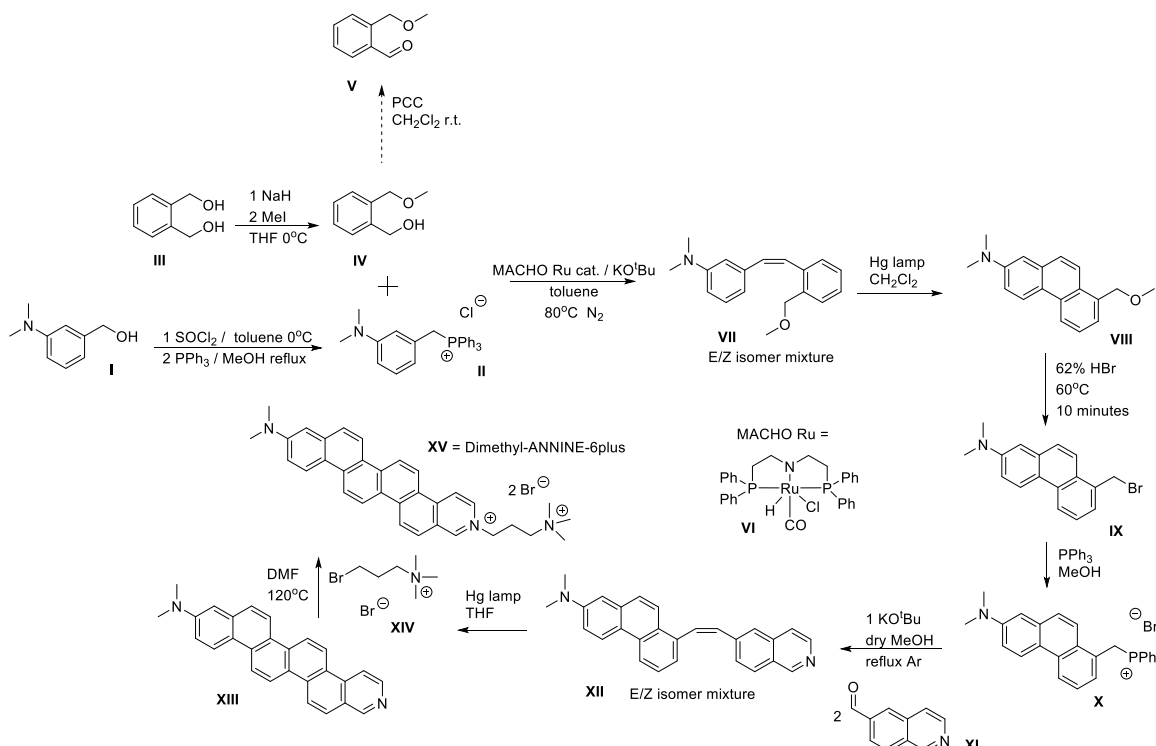

Figure 3.1. Compounds **I** (3-*N,N*-Dimethylaminobenzyl Alcohol), **III** (1,2-Bis(hydroxymethyl)-Benzene), **VI** (Ru-MACHO), and **XI** (5-formylisoquinoline), were purchased from Combi-Blocks, BLD Pharmatech, TCI, and Aldrich respectively and used without further purification. The synthesis was adopted from Hubner et. Al 2003 (Hübener et al., 2003). Figure created by Dr Eugene Kashkin.

is only around 100μm thick (dye injected at this depth or shallower tends to leak out of the brain). For researchers wanting to study large scale brain dynamics, using voltage dyes, it is necessary to bathe a large area of the brain in the dye to achieve adequate staining. This either means removing a large piece of dura (or doing the study in acute brain slices – for example (Tominaga et al., 2000; Suh et al., 2011), or using a dye that penetrates easily through the dura and then settles deeper in the cortex (Kleinfeld and Delaney, 1996; Petersen et al., 2003).

As such, large scale neural activity, when measured this way, excludes a lot of the smaller Layer 1 components.

To get around these problems, our group synthetized a new, more hydrophilic dye in the ANNINE family – Di1-ANNINE-6plus (Fig. 3.1). This new dye follows from ANNINE-6plus (Fromherz et al., 2008), in that the ANNINE-6 backbone is kept intact so the resulting fluorescent properties are unaffected, but changes the tail of the dye, to be more readily dissolved in saline. I also developed a surgery in which the dye can be applied directly to the brain surface without removing the dura. Dye then diffuses throughout Layer 1, and the upper section of Layer 2, so successful functional imaging can be undertaken in Layer 1 without damaging Layer 1 in the process.

Methods

DiMethyl ANNINE-6plus was prepared for me by a chemist at OIST (Dr Eugene Khaskin). All the experiments that follow used this dye (chemical structure can be seen in Fig. 3.1.).

Surgery and Dye Application

All animal experiments were performed in accordance with guidelines approved by the Okinawa Institute of Science and Technology Graduate University Institutional Animal Care and Use Committee (IACUC) in an Association for Assessment and Accreditation of Laboratory Animal Care (AAALAC International) accredited facility.

The surgeries conducted here were an alteration of the standard chronic cranial window surgeries, described in (Holtmaat et al., 2009; Roome and Kuhn, 2014). Seven male C57/BL6 mice, between 31 and 180 days old were used – through experience, mice around 60 days old provided the cleanest surgeries.

Mice were head-fixed and anesthetized with isoflurane at 0.5-2% during the surgery. First the mouse's eyes were protected from debris and drying with an eye ointment, and then the hair on the scalp was removed with an electric shaver, and hair removal cream. Carprofen (5μg/g body weight) and Buprenorphine (0.1μg/g body weight) were injected subcutaneously, and Dexamethasone (2μg/g body weight) was injected intra-muscularly, into the hind limb. The scalp was then cleaned with iodine solution, and numbed with a Lignacaine gel, before being opened with a scalpel. A pair of surgical scissors was then used

to remove a triangular flap of skin, exposing the skull from above bregma, to just beyond lambda, going slightly right of the midline, and exposing the entire parietal bone on the left. The bone was then dried and cleaned with a combination of compressed air, and scrubbed with sterile cotton swabs, soaked in Lidocaine. The craniotomy was then marked out (3.5-4mm diameter round section, AP-1.5mm, L-3mm), and bone surrounding it was carefully thinned and smoothed. Finally a channel around the craniotomy was made, allowing the bone above the craniotomy to float freely from the rest of the skull. Following Roome, & Kuhn 2014 (Roome and Kuhn, 2014), a wooden toothpick was glued vertically onto this free floating bone, using superglue.
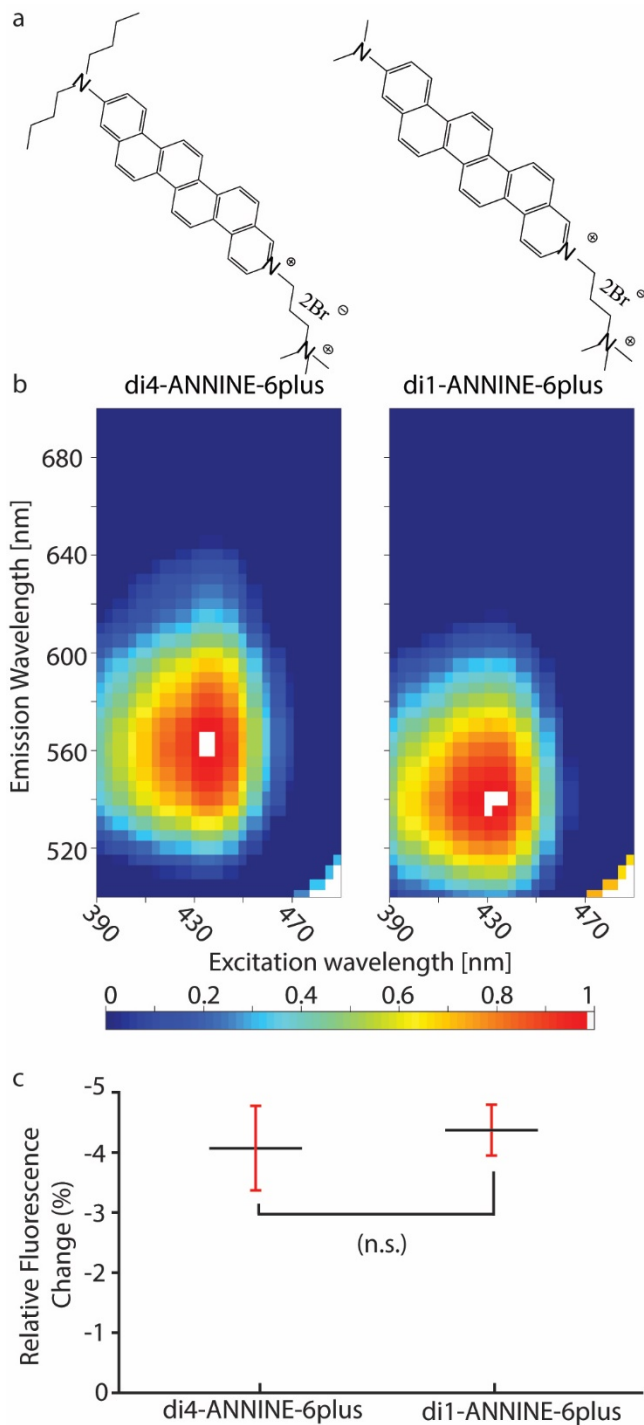
Figure 3.2. Dye molecular structure and corresponding 2D spectra of excitation, and emission wavelength. The difference between the chemical structures (**a**) of these two dyes can be seen in the tail group (left hand edge), where ANNINE-6plus has much longer tail groups than DiMethyl ANNINE-6plus. The resulting fluorescence spectra (**b,** captured with the dye in homogenized cortex, in saline) are very similar. To test the dyes' sensitivity, HEK-293 cells were stained with each dye, and then depolarized with gramicidin. The resulting change in fluorescence (**c**) shows the similarity in sensitivity of the two dyes.

If a reference electrode, or electro-encephalogram wires were needed for further experiments, they would be implanted at this point. For electro-encephalogram wires, during the time it takes for the superglue to set, two simple silver wire electrode leads were inserted under the skull, one lateral to the craniotomy, and the other on the opposite hemisphere, symmetrically opposed to the craniotomy. These electrodes were made from silver wire (0.404mm thick, cut to approximate 2-3cm long), with the last 5mm of them hammered flat. A small hole would then be drilled mostly through the skull, where the wire should be placed, and then the hole would be finished with a small cut from a 26-guage beveled needle, so that the brain under the hole would be undamaged. The wire was placed into the hole, with the flat side facing the brain, so it could sit on the brain surface (or on the dura), without digging into the cortex. After sliding 3-5mm of wire parallel with the brain surface, into the hole, it was then superglued in place, ensuring the wire lead also lay fairly flat on the skull. After both wires were glued in place, preparation to open the craniotomy could begin.

For a reference electrode, the steps are similar, but only one electrode is required, and instead of sliding it under the skull, keep the skull intact, but thinned, and place the flattened wire into the divot made on the skull. This divot will prevent the wire from sticking up and tilting the headplate later on, and also ensure good contact of the wire with the skull.

As the craniotomy needed to hold dye, dental acrylic was applied around the edges of the craniotomy, being careful not to let it leak into the channel between the skull and the free bone. This acrylic built up to create a flat surface that would later be used to mount the head-plate. If electrodes were present, some acrylic at this point was also applied to the base of the electrode leads, helping to cement them in place, and making them more robust, in case the mouse plays with them in the future. Buildup of acrylic was limited to less than 1mm however, so that the eventual mounting of the head-plate would not prevent the microscope objective from reaching its required depth. An image of the surgery at this step can be seen in Figure 3.3, **a**.

After the acrylic dried, the craniotomy bone could be removed, carefully cracking all the edges of the channel by rocking the toothpick slowly back and forwards, before slowly peeling the bone away, using the toothpick as a handle. If done gently, the dura will remain intact, and there should be little to no bleeding (small blood vessels under the skull can be

damaged at this point
and the surgery is still
salvageable, but with
care and practice, this
can be avoided, or at
least minimized –
Fig. 3.3, **b**).
Gelfoam which had
been soaking in a mix
of saline and
Carprofen solution
was gently packed
against the edges of
the craniotomy, so
that the hard bone
would not damage
the dura during this
extended opening of
the skull. Next, dilute
hydrogen peroxide
(10% H2O2, diluted
in saline 1:6 –
protocol inspired by
Sheroziya, &
Timofeev 2014
(Sheroziya and
Timofeev, 2014))

Figure 3.3. Progression of cranial window during surgery (**a, b, c**), and resulting window under a microscope (**c**). The surgery progression shows the separation of the bone over the cranial window, by drilling a channel through most of the bone around the window, and then gluing a wooden toothpick to the floating cap of bone (**a**). Dental cement covers the bone beyond the window area, and is pink. The blue ink marks where the window is planned. Next, using the toothpick as a handle, the bone cap is gently removed, and saline is added to wash away any blood that comes up in the process (**b**). Hydrogen peroxide is added, causing the dura to bubble up, which can be seen in (**c**). Note that gelfoam was excluded in these photos, so the dura and craniotomy could be seen clearer. Finally, after injecting dye into air space created, and then covering with a glass coverslip, the window can be imaged in a microscope. The result is shown in (**d**), using a green filter to raise contrast of the blood vessels against the brain.

was dripped onto the open dura, using an eyedropper. Drips were added until the dura had puffed up, and separated from the brain below. Saline was then used to wash away the peroxide, but leave the dura bubbled away from the brain. The dura bubble was continuously kept covered with saline (the dura could poke out the top of this saline lake, but the edges of

the craniotomy should be covered in saline), to make sure any puncture to the dura that might happen from rubbing on the edge of the bone was sealed away. The gelfoam was also repacked against the edges of the bone, to help maintain the air pocket in the dura (Fig. 3.3, **c**).

Once this dura bubble was stabilized, a micropipette (quartz glass, 20μm tip, 300μm bore) was filled with 200-1000nl of the voltage dye, Di1-ANNINE-6plus, using suction. The stereotaxic frame was used to position this pipette above the dura bubble and then slowly enter it, being careful not to touch the brain itself. Once the tip was inside the bubble, the contents of the pipette were pushed out, using positive pressure, but making sure that the final few nanoliters of dye remained in the pipette, as pushing air into the bubble tends to create bleeding, or smaller bubbles within the overall dura bubble, which are inconvenient for dye loading. After this, the pipette was carefully removed along the same path that it entered, so that the dura would not deflate. The pipette could then be reloaded with dye, and deliver it inside the dura bubble, until several microliters of dye had been delivered, and there was a visible layer of dye on the brain surface. From here, a short rest of 5-10 minutes was given, to let the dye diffuse, and for the bubble to deflate as much as it could passively, before putting a 5mm diameter glass window (170μm thick) onto the dura bubble, and slowly pressing it down. The window was then glued in place to the bone edges of the craniotomy, using thin superglue, applied with a transfer pipette. Dental acrylic was then applied to cover all remaining bone, and then some more to the already dried acrylic, and a metal headplate was cemented onto the skull. The headplate opening was positioned to show the craniotomy, and the edges of the window were then sealed with dental acrylic, making a well that could hold water for our water immersion microscope objective. From here the surgery was complete, and the mouse was transferred without waking from anesthesia, to the microscope for functional imaging.

Imaging Setup

Imaging was performed with a custom wide-field and two-photon microscope (MOM, Sutter, designed by Winfried Denk). A 2.5x air objective (Zeiss A-Plan 2.5x/0.006) was used for wide-field imaging to inspect the window (Fig. 3.3, **d**), and then swapped out for a 25x water immersion objective (Olympus XLPlan N 25x/1.05 W MP) for two-photon imaging. The tuning collar for the 25x objective was purposefully de-focused, so the excitation focal point

would be slightly spread out, and slightly more voltage dye would be excited with each scan. This meant that our resolution was slightly worse than optimal resolution for the microscope, but was still fine enough for optical sectioning (resolution was approximately $\sim 5\mu m$ in the z axis). The dye was excited with 1020nm laser light, from a pulsed Ti:sapphire laser (Chameleon Vision II, Coherent), and collected with a single GaAsP photomultiplier tube (Hamamatsu), without passing through any filters. For functional scans, a line scan was used to collect fluorescent images of the same line (512 pixels, approximately 250μm long) at 2 kHz.

Functional images were taken after dye was shown to have diffused through Layer 1, approximately 30-45minutes post-surgery. Anesthetized recordings were done first, with gaseous isoflurane delivered to the mouse (0.5-1%), and a heating pad, combined with rectal temperature probe were used to keep the mouse above 36 degrees C. Awake recordings were made after all the anesthetized recordings were finished. The heating pad and temperature probe were removed, the isoflurane was turned off, and the mouse was allowed 15-20 minutes to wake up. Once the heating pad was removed, the treadmill wheel that the mouse was sitting on would become free, so the awake mouse could run if it chose to.

Data Analysis

All functional images were imported into Matlab (Mathworks) and were processed using custom, in house scripts. Each line scan file was processed separately, before its data was pooled for averaging. Through trial and error I found that creating a time series for fluorescence changes for four pixel blocks, and then creating a frequency spectrum for that time series, resulted in the highest signal to noise spectra, so these were calculated for all pixels in all files. Spectra were the averaged based on cortical depth (25, 50, 75, and 100 μm deep), and cortical state (awake, and anesthetized). These averaged spectra were normalized by calculating $S(f) = \frac{s(f) - s_0}{s_0}$, where s_0 is the average power in the frequency range between 40 Hz and 50 Hz, where I noticed no peaks or activity in individual spectra (Fig. 5c). Some artifacts were detected, indicated by sharp frequency peaks. All artifacts were above 50 Hz, where we could not detect any noticeable oscillation peaks, so the spectra were trimmed to 50 Hz. No filters were applied to the raw voltage data, or frequency spectra. Artifacts due to breathing (typical frequency ~ 2.5 Hz) and heart beat (typical frequency $\sim 8 - 10$ Hz) were not observed.

Dye Spectral Analysis

To determine how the dye compares as a fluorescent probe, to the previously published ANNINE-6plus (Fromherz et al., 2008), I homogenized freshly removed mouse cortical brain tissue and labeled it with di1-ANNINE-6plus or di4-ANNINE-6plus (both, stock solution 2.3 mM in DMSO, then diluted to 20µM in 0.9% NaCl saline). I used a TIDAS S 700 UV/NIR 2098 diode array spectrometer coupled to a TIDAS S Monochromator-VIS with 75 W Xenon light source (J&M Analytik AG, www.j-m.de). Excitation wavelength was varied from 390 nm to 500 nm, in 5 nm steps, while the emitted light was collected with a diode array from 200nm to 980nm with 5 nm resolution. Data were exported to Matlab (Mathworks) to create 2D spectra graphs, normalized to the global peak intensity (Fig. 3.2).

Sensitivity of di1-ANNINE-6plus compared to di4-ANNINE-6plus

Human embryonic kidney (HEK) 293T cells were cultured in 24 well plates, in Dulbecco's modified Eagle's medium, with high glucose, pyruvate, supplemented with 10% fetal bovine serum (Biowest), and 1% penicillin streptomycin (Sigma). This cell growth step was performed by Soumen Jana of the Optical Neuroimaging Unit, at the Okinawa Institute of Science and Technology. Once cells were mature and a monolayer had formed, the medium was replaced with either di1-ANNINE-6plus or di4 ANNINE-6plus (both, stock solution 2.3 mM in DMSO. di1-ANNINE-6plus stock was diluted 1:10 in phosphate buffer solution, 7.4 Gibco (PBS), and di4-ANNINE-6plus was diluted 1:100 in PBS). After waiting for 20 minutes for the dye to penetrate the cells, a single well was chosen, and the dye solution was replaced with gramicidin solution (1mg/ml stock in DMSO, diluted 1:71 in PBS for di4-ANNINE-6plus, and 1:21 in PBS for di1-ANNINE-6plus). The fluorescence of the cell population was imaged with a confocal microscope, at 488nm excitation (Nikon N-SIM/N-STORM, emitted light collected from 570 to 620nm), in a time series starting from when the gramicidin was added, an image was taken every 10 seconds (1 image created from 4 averaged images), for 10 minutes. Gramicidin applied in this way depolarized the cells within $6 - 7$ minutes, so the time series captures the initial and end fluorescence, leading to a measure of sensitivity ($\frac{F\ initial - F\ final}{F\ initial}$). The sensitivity measurement was averaged across five wells for di1-ANNINE-6plus, and five wells for di4-ANNINE-6plus. As di4-ANNINE-6plus sensitivity is already well established (Fromherz et al., 2008), a simple comparison between the two dyes is possible.
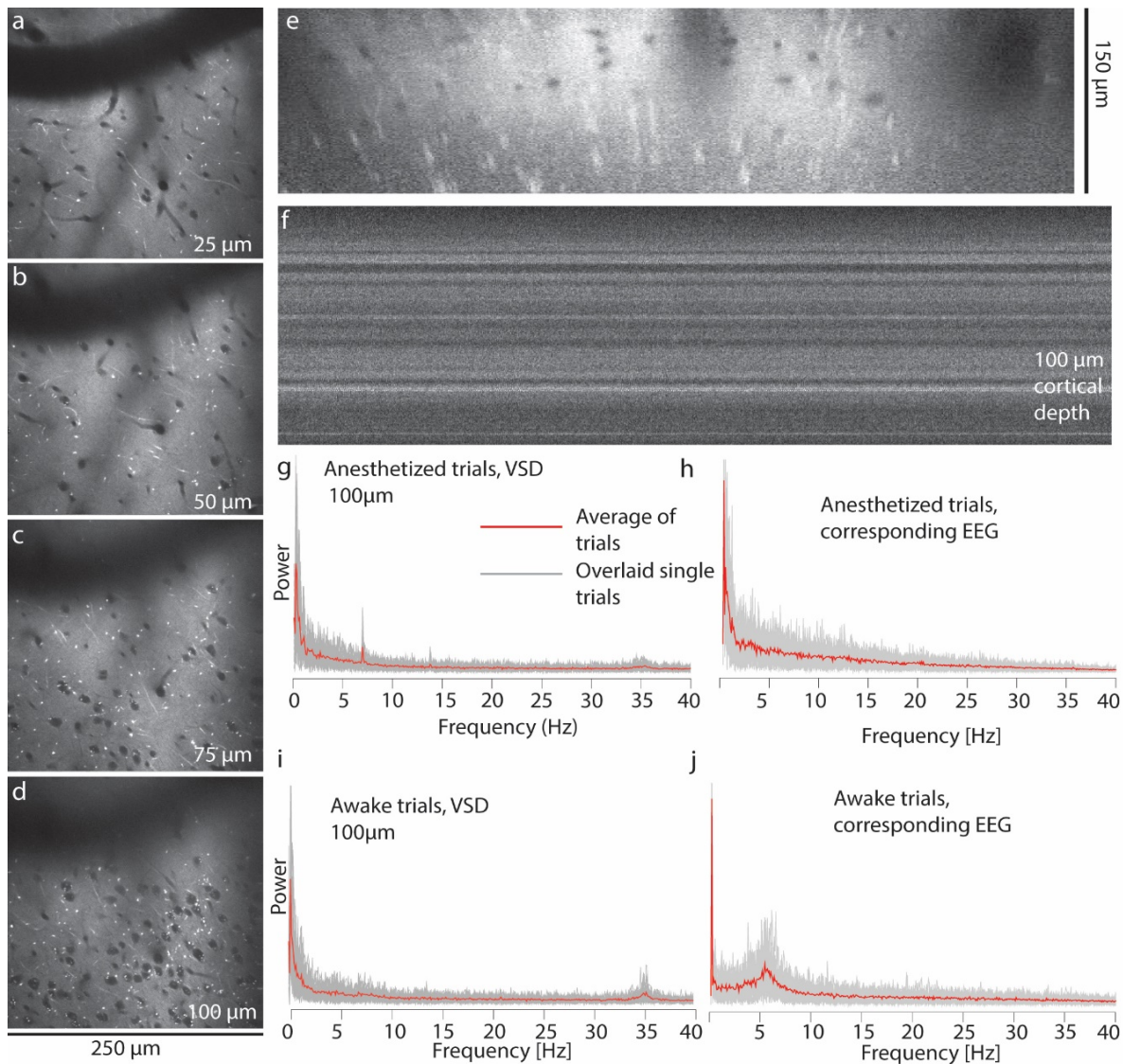
Figure 3.4. In vivo labeling of di1-ANNINE-6plus. (**a-d**) Penetration of di1-ANNINE-6plus *in vivo* in different depth, (**e**) x-z reconstruction, (**f**) line-scan, and (**g-j**) corresponding frequency spectra of membrane voltage and EEG recording calculated from 30 recordings (11 s each, gray background: overlay of single trials, red line: average) in an awake and anesthetized mouse.

Results

di1-ANNINE-6plus fluorescence

Comparing di1-ANNINE-6plus with the previously published di4-ANNINE-6plus (ANNINE-6plus, (Fromherz et al., 2008)), the spectra are similar (Fig. 3.2). The excitation peak appears unmoved, while the emission peak is slightly shifted from 560nm (di4-

ANNINE-6plus) to 540nm (di1-ANNINE-6plus). This suggests some change has occurred to the chromophore of the dye, but the change is not dramatic, and does not affect its excitation characteristics.

Sensitivity of di1-ANNINE-6plus

In cultured HEK 293T cells, when depolarized with gramicidin, di1-ANNINE-6plus recorded a mean fluorescence change of 4.32% (0.4% standard deviation). In the same preparation, di4-ANNINE-6plus recorded a 4.02% change (0.7% standard deviation). A t-test (unpaired, two-tailed) showed no significant difference between these two dyes (p = 0.44, Fig. 3.2).

di-1-ANNINE-6plus *in Vivo*

Dye penetration and recordings can be seen in Figure 3.4 (**a** through **e**). Using this novel dye application method, dye reliably penetrates down 150µm, while depths beyond this have also been seen but are less reliably achieved. Staining becomes useable for functional imaging 45-60 minutes after application, and can last strongly for up to 48 hours.

After recording a single 11 second line scan, a frequency spectrum can be calculated up to a frequency of 1 kHz with a signal-to-noise ratio of approximately 1.5 : 1. Further averaging reduces noise following the square root of the number of averages. Example spectra after averaging 30 line scan files, each 11 seconds long can be seen in Figure 3.4 (**g, i**), along with the simultaneously recorded EEG spectra (Fig. 3.4 **h, j**). These were recorded at 25, 50, 75, and 100 µm below the dura. During light anesthesia, theta produces a sharp, reliable peak.

Averaging spectra across all seven animals, average spectra were calculated for each recorded cortical depth in Layer 1 (25, 50, 75, and 100µm below the dura), and for the corresponding trial's EEG recording. These average spectra can be seen in Figure 3.5 (**a-f**). Notable activity is seen in the VSD is seen in delta (0-4 Hz), theta (4-10 Hz), and gamma (30+ Hz), with slight differences in depth, but larger differences from light anesthesia to wakefulness. The EEG recordings show no large theta activity during anesthesia, but does show the theta peak during wakefulness. The beta and gamma peaks were not detected in the EEG.

Measurements of the spectra over depths and cortical state were calculated in two ways – by either taking the maximum power, or the integral of the power, over small frequency bands. The maximum power over small frequency bands can be seen in Figure 3.5 (**c**), while the
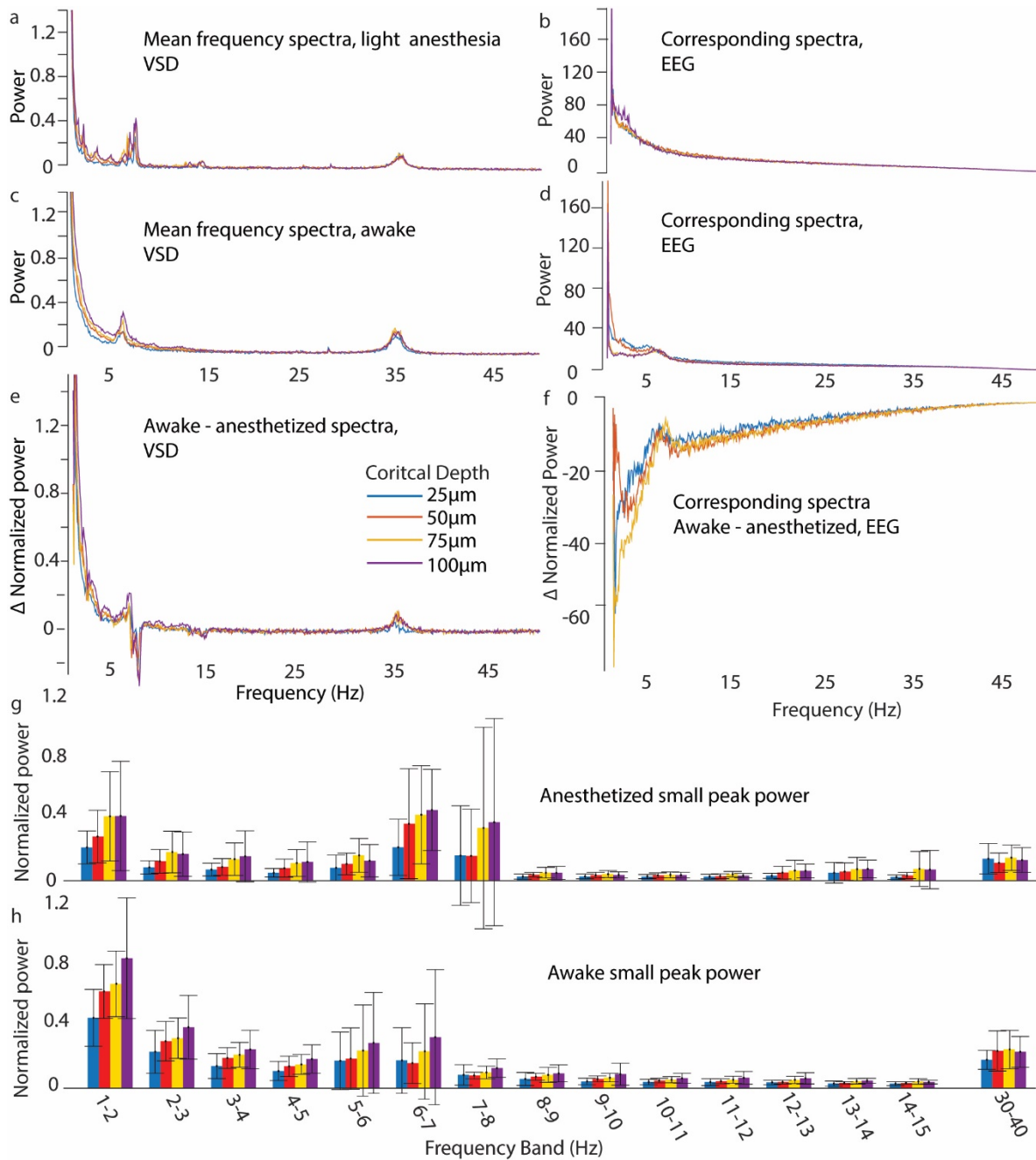
Figure 3.5. Average frequency spectra (**a, c**), for anesthetized and awake conditions, separated by cortical depth (210 averages, 7 mice), and the difference between the spectra (**e**). Corresponding frequency spectra for each set of trials in **a, b, c** calculated from simultaneously recorded ECoG. Small frequency bands were examined, and the maximum power was plotted (**d**). Error-bars represent standard deviation.
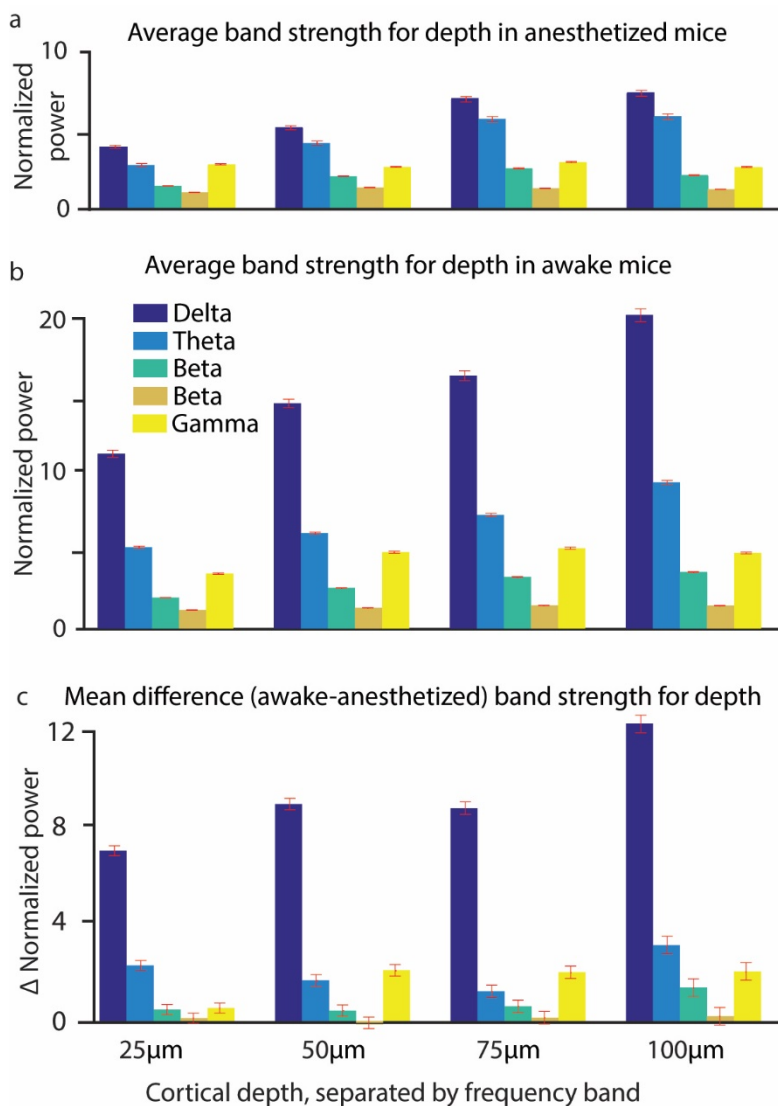
integral of powers over a band can be seen in Figure 3.6. Lower delta power below 1 Hz

was excluded, as the 11 second recording did not provide a robust enough measurement of the extremely slow oscillations. The power of every band was higher in integral and maximum for awake conditions, except for the theta peak (6-8 Hz). There is a general increase in power with depth as well. Finally the presence of a clear low gamma (approximately 35 Hz) peak is very interesting, and to the best of our knowledge, never reported before in cortical Layer 1. Larger frequency bands following traditionally defined frequencies were also examined using the integral of power over the measured band. These bar graphs can be seen in Figure 3.6, showing awake (**a**), anesthetized (**b**), and

Figure 3.6. Normalized power of major frequency bands (Delta 0.5 – 4Hz, Theta 4 – 10Hz, Beta lower 10 – 20Hz, Beta upper 20 – 30Hz, Gamma 30 – 40Hz). (**a**) Shows the bands during light anesthesia, while (**b**) are the same bands and depths during wakefulness. A difference between wakefulness and light anesthesia was calculated within each mouse, and then averaged across mice, and this is shown in (**c**). Error bars show standard deviation.

the difference between awake and anesthetized, calculated within mice and then averaged across them (**c**). The low gamma band is consistently larger in awake mice than anesthetized,

but relatively consistent in power (with 25µm being exceptionally low). Delta also shows much larger responses in awake than anesthetized, plus it consistently increases with cortical depth. The integral of theta power is higher consistently during wakefulness than light anesthesia, but the maximum peak power, generally around 6-8Hz does not follow this rule (see Fig. 5**c** for smaller frequency bands, showing sharper peaks).

Gamma was isolated for each cortical depth and brain state, using an inverse fast-Fourier transform, over the 30-40Hz band, with phase removed. This calculates the highest $\Delta F/F$ for the averaged gamma band. These numbers were between 0.039% and 0.058% change in fluorescence. From previous research, this can be converted to mV, based on a dendritic density of the upper cortex (Kuhn et al., 2008). Dendrites in the upper cortex make up 23% of cortical volume (Williams et al., 1980; Braitenberg and Schüz, 1998), and previous ANNINE dyes have a reported sensitivity of -0.49% change per mV, when excited at 1020nm (Kuhn et al., 2004). This gives a conversion of -0.11% fluorescence change per mV. This results in the following gamma fluctuations in mV (Table 3.1). These recordings are in line with previously reported gamma oscillation magnitudes (Penttonen et al., 1998). A baseline period between 45 and 55Hz was also defined, and subtracted from the gamma frequency power band. This baseline adjustment should remove noise fluctuations, giving a more conservative and accurate conversion.

Table 3.1. Gamma Oscillation Peak in in $\Delta F/F$, corresponding average voltage change if a conversion factor of 0.47%/mV (Kuhn et al., 2004) is applied, and the voltage change under the assumption that only dendrites participate and that 23% of the membrane surface is contributed by dendrites (Braitenberg and Schüz, 1998).

Cortical Depth	Light Anesthesia			Awake		
	$\Delta F/F$ [%] ± S.D.	Average voltage change [mV]	Dendritic voltage change [mV]	$\Delta F/F$ [%] ± S.D.	Average voltage change [mV]	Dendritic voltage change [mV]
25µm	0.048 ± 0.012	0.10	0.44	0.053 ± 0.017	0.11	0.49
50µm	0.044 ± 0.015	0.092	0.40	0.067 ± 0.018	0.14	0.62
75µm	0.045 ± 0.011	0.097	0.2	0.057 ± 0.016	0.12	0.53
100µm	0.045 ± 0.012	0.095	0.41	0.061 ± 0.016	0.13	0.56

As theta also makes a considerable peak, it was also isolated and converted into mV changes (Table 3.2). The baseline period (45-55Hz) was used as a noise measurement, as with the gamma recordings, and subtracted from the frequency peak before converting from frequency power to mV. This leads the mV value to be lower than the gamma values for some depths. The anesthetized theta peaks are higher than the gamma peaks in general, while awake theta and gamma peaks appear roughly the same magnitude.

To confirm that the spectra are showing biological signals rather than noise, a sample set of line scans were selected from a single mouse, from a close time period (all were collected within 5 minutes of each other). A single spectrum was compared with 4 spectra averaged, and 9 spectra averaged. These traces are overlaid and can be seen in Figure 3.7 (**a**). In doing this, it is possible to see the sections of an individual trace that are noise, compared to the underlying signal.

Table 3.2. Theta Oscillation peak dendritic voltage change, calculated in the same manner as Table 3.1.

Cortical Depth	Light Anesthesia	Awake
25μm	0.28mV ± 0.07	0.43mV ± 0.13
50μm	0.38mV ± 0.10	0.44mV ± 0.09
75μm	0.47mV ± 0.08	0.47mV ± 0.11
100μm	0.52mV ± 0.11	0.62mV ± 0.14

 Additionally, the size of the noise reduces as expected with the number of averages. Another control was performed by taking recordings during constant anesthesia, and in blocks of five files. Five files were recorded with 1020nm excitation, which has been shown previously (Kuhn et al., 2004) to be the peak excitation for ANNINE family dyes. Next, the laser was quickly switched to 970nm, and another set of files were recorded, and then finally the laser was turned to 920nm for a final five files. This order was also reversed, going 920, 970, 1020nm. This was repeated 30 times. To test the dye's voltage sensitivity to a biological signal, recordings were made in blocks of 5 files (each 12 seconds long), at 1020nm, 970nm, and 920nm excitation by the scanning laser. Theta peaks were averaged across these 5 block trials 30 times (Fig. 3.7 **b**). 1020nm produced the largest peak (3.434 normalized power ±0.176 95% C.I.), the 970nm (2.439 normalized power ±0.136 95% C.I.), and then 920nm (1.368 normalized power ±0.074 95% C.I.). None of these confidence intervals overlap,

indicating a significant difference between each excitation wavelength. This is in line with previous ANNINE dyes (Kuhn et al., 2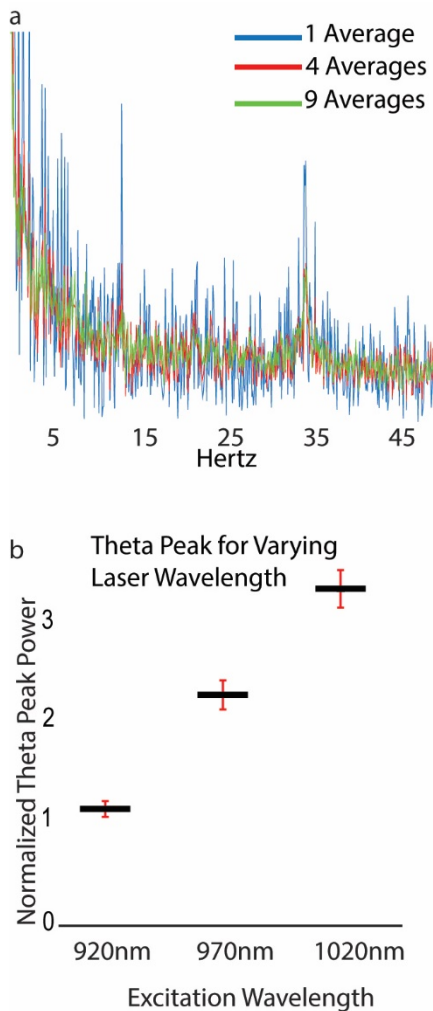008), where larger wavelengths of excitation produce larger voltage sensitivities. This shows that the dye was truly detecting a voltage signal originating in the biological sample (the theta peak), confirming the newly synthesized voltage dye worked.

Discussion

Di1-ANNINE-6+ is a new formulation of an old dye, and shows great promise for use in Layer 1.

Bubble surgeries are ideal for applying dye to the surface of the brain, and achieving a good Layer 1 stain, with minimal damage to the cortex. This surgery makes sense for combination with dyes that are too viscous or lipophilic to penetrate through the dura, and so cannot be applied directly to an open craniotomy. It should be noted that although I have not quantified the damage or lack-of, to the cortex with this surgery, in the original work (Sheroziya and Timofeev, 2014) peroxide based dura removal was shown to be gentler than mechanical dura removal. Given the lack of damage to the cortical surface, I recommend this surgery over any dye application where the dura would instead be removed entirely, as the process of removing the dura can be quite difficult without causing damage and bleeding.

Di1-ANNINE-6+ applied to the cortical surface provides an interesting new approach to cortical Layer 1 research. Previously, Layer 1 has been extremely difficult to reach with our available tools, and even with voltage dyes, labelling within the cortex tends to focus around layers 2 and 3 (Kleinfeld and Delaney,

Figure 3.7. Control tests for di1-ANNINE-6plus VSD. Averaging spectra shows decreasing noise with the square of the number of averages (**a**). Theta peaks were very consistent during light anesthesia. Voltage sensitivity was increased as the more optimal laser excitation was used (**b**). Black bars represent the mean theta peak, and red error-bars show the 95% confidence interval.

1996; Petersen et al., 2003). To have a dye and application method that works best for Layer 1 study can be very useful in studying Layer 1 activity, like neural oscillations. During testing of the dye, using this staining method, it was possible to record line scans in Layer 1 from multiple points inside the cranial window, up to 3mm away from each other. This means large spatial scale recordings are possible using this dye and application method, and these would be a particularly interesting way to probe Layer 1 activity.

It is worth pointing out that two-photon imaging, which was used in our experiments, optically sections images, so that areas stained that are out of focus do not influence the recording made at a particular focal depth. This is different from traditional light microscopy, where any light collected is a mix of in and out of focus areas. This optical sectioning means any recorded signal within Layer 1, is a real measurement of voltage, within Layer 1, and not contaminated by larger sinks or sources from deeper layers.

Additionally, data presented here (Fig. 3.5 and 3.6) show changes in oscillations with depth, through Layer 1, recordings which have previously been impossible (recordings made in the previous chapter were very difficult to reliably get all layers in layer 1 stained to an acceptable level). Of particular note is the 35Hz oscillation peak, making it a low gamma oscillation. Gamma is thought to be created from an interaction between pyramidal neurons and fast spiking interneurons, when in the cortex (Buhl et al., 1998; Bartos et al., 2007; Merker, 2016). Layer 1 is not thought to contain fast spiking interneurons, and the pyramidal cell fibers that are present come from diverse areas (Cauller et al., 1998). For them to be coherent enough to make a detectable oscillation peak is surprising.

One considerable difference between data here, and data in the previous chapter is that here more animals were used in each recording, and oscillations were the aim of these recordings, rather than capturing a combined voltage and calcium activity, during whisker stimulation. This let me focus solely on how the oscillations change due to depth and state, and gave the highest signal to noise ratio of these oscillation peaks. In this way, it is possible to see the increase in all measured frequency bands, except for higher beta, and gamma, with cortical depth (Fig. 3.5, 3.6, and 3.7). This was the expected result of recordings in layer 1, as signals become more consolidated within a local region. Layer 1 anatomy shows a lot of diverse branching, especially in the very upper areas (Cauller et al., 1998; Porrero et al., 2009; Narayanan et al., 2015), and dendrites also tend to narrow as they branch further, so signals

in the upper reaches of layer 1 are smaller and more diverse. This should lead to a reduction in oscillation strength and coherence, and thus can explain the increase in power with depth. Why gamma does not experience this same trend is unknown. Gamma forms a noticeable peak, (Fig. 3.4, and 3.5) so it would be expected that it too increases in power as you follow the dendrites down towards the cell body, and remove extra signals from less local areas. This suggests that the entire local area is oscillating in gamma coherently, and that the entire dendritic arbor of the local cells are experiencing gamma oscillations.

Converting the recorded neural oscillations into dendritic mV values relies on several assumptions. First, dendritic density is assumed to be relatively constant through layer 1, as the same density for conversion is used for all the calculations. Secondly, the baseline fluctuation removal, by subtracting the 45-55 Hz power from the frequency band being converted, I avoid converting noise fluctuations to mV. If 45-55 Hz does not reflect the true noise level, which is instead at some higher frequency, the subtracted power would be less and the resulting oscillation mV value would be higher. Lastly, if fewer than all the dendrites in the region are experiencing the oscillation, then the mV within the oscillating dendrites will be higher. VSDs selectively report dendritic activity, but bulk loaded like this report all dendritic activity in the area. If an oscillation is occurring in only a subset of the dendrites recorded, it will just appear as a smaller fluctuation in the recorded voltage, as it will be averaged across oscillating and non-oscillating dendrites. This will not make a large change if only a small subset of dendrites are not oscillating, but if a significant portion are not, then the recorded mV may be much higher.

Looking at the mV values however, they are in the same range as recorded values in intracellular recordings in the hippocampus (Penttonen et al., 1998). The values are expected to be slightly higher, as it is unlikely that every single dendrite recorded was experiencing the same coherent oscillations, however values would still be within the $0.2 - 2$ mV range, as long as greater than about $1/8^{th}$ of all dendrites are experiencing the same oscillations.

In summary, this work has created a novel surgery that has the possibility to be useful for more than just voltage dye loading. Any case where bulk liquid is best applied to the brain surface, this surgery could be useful. Removing the dura is a difficult procedure that can also destabilize the local cortex. In contrast, creating a bubble that can be loaded with solution which then collapses over some time is potentially less disruptive to the brain and is easier

to achieve. Additionally, oscillations faster than any previously captured by *in vivo* VSD recording have been detected, in cortical layer 1, where voltage recordings are extremely rarely made. The data aside, these technical breakthroughs in VSD loading, layer 1 labeling,

layer 1 voltage recording, and VSD oscillation recording have the potential to impact select fields in the neurosciences.
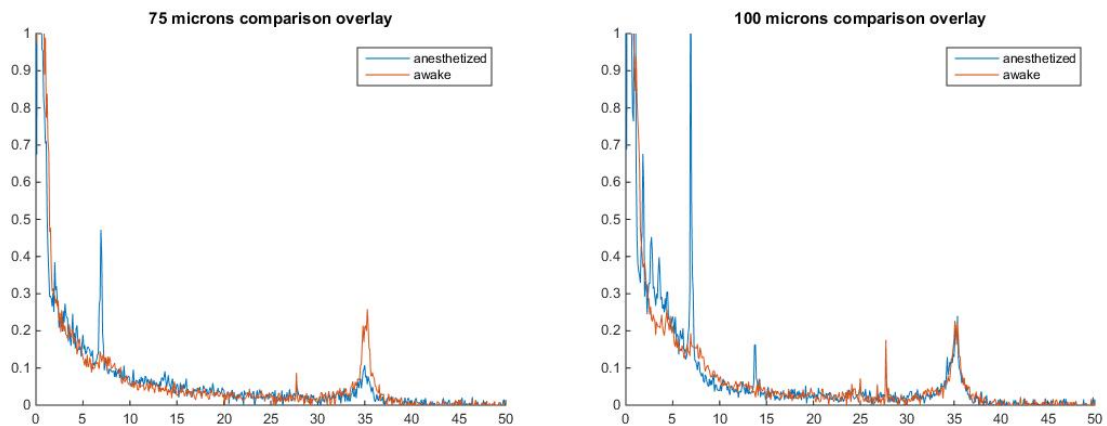
Supplemental Figures

Supplemental figure 3.1. Average spectra of each mouse for 25 and 50 µm cortical depth. Red shows awake recording, and blue shows the anesthetized recording from the same session. Each graph is paired 25 and 50 µm from the same recording session.
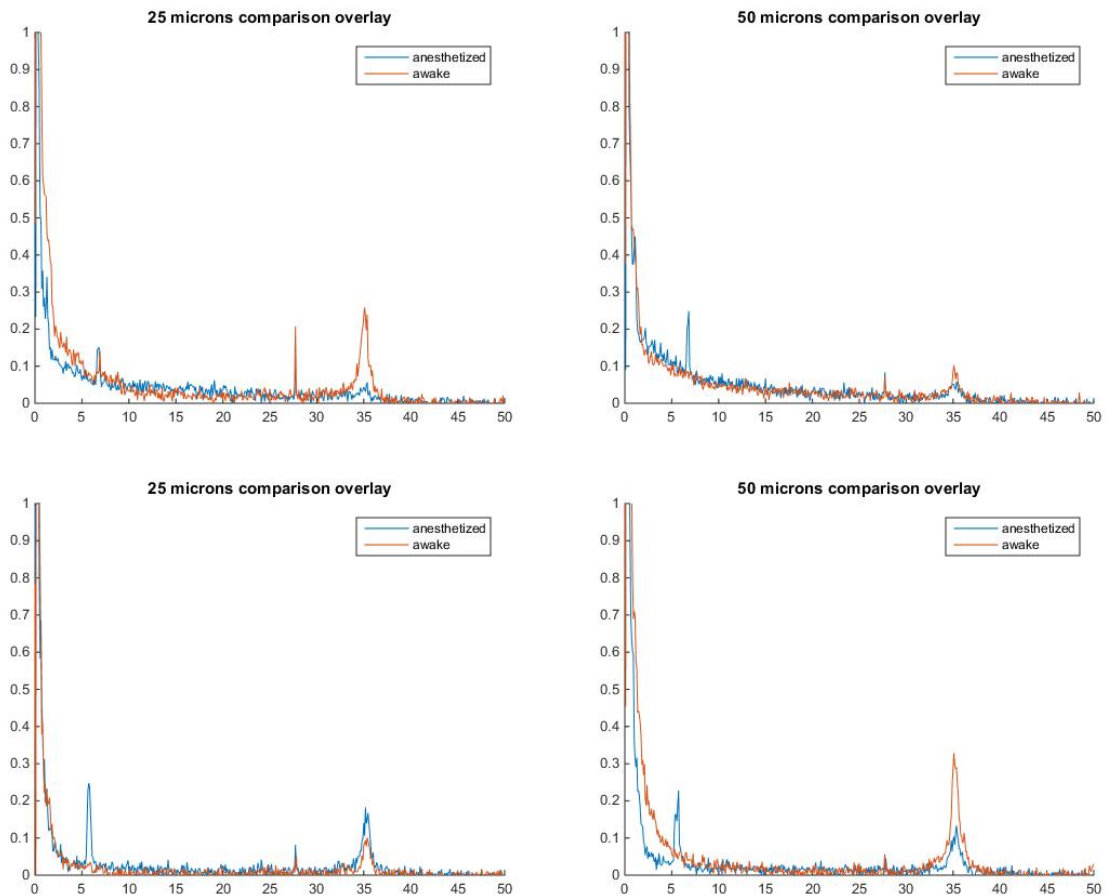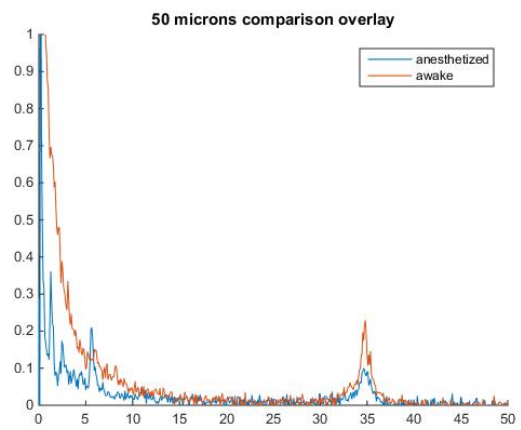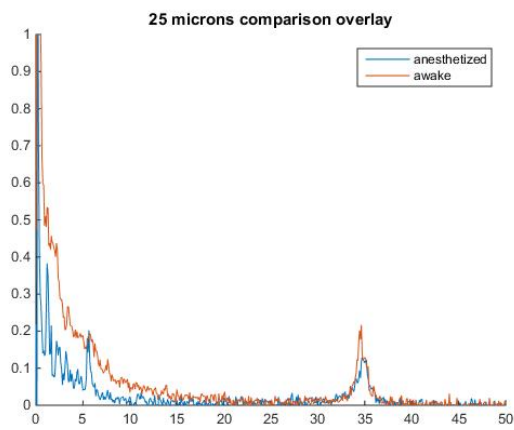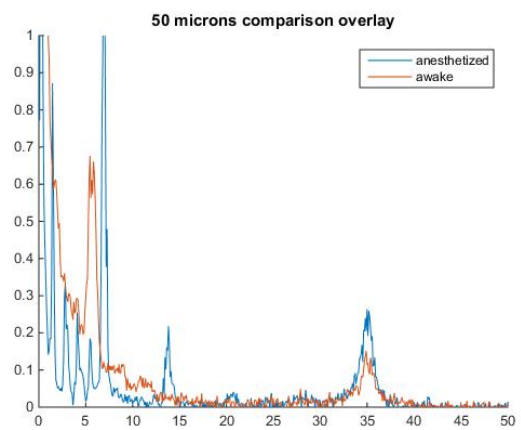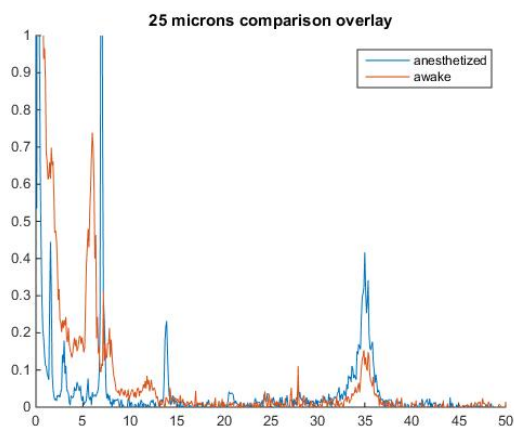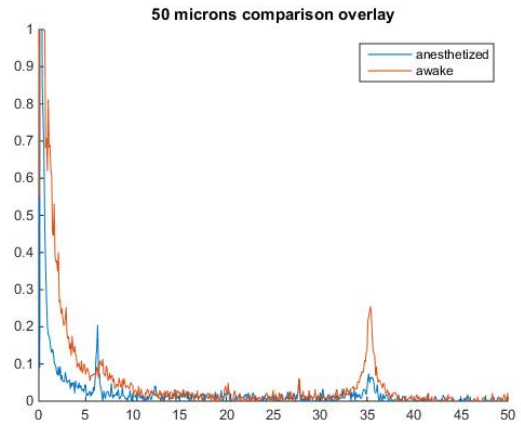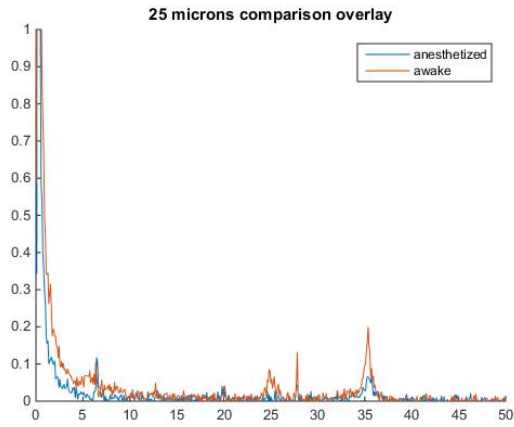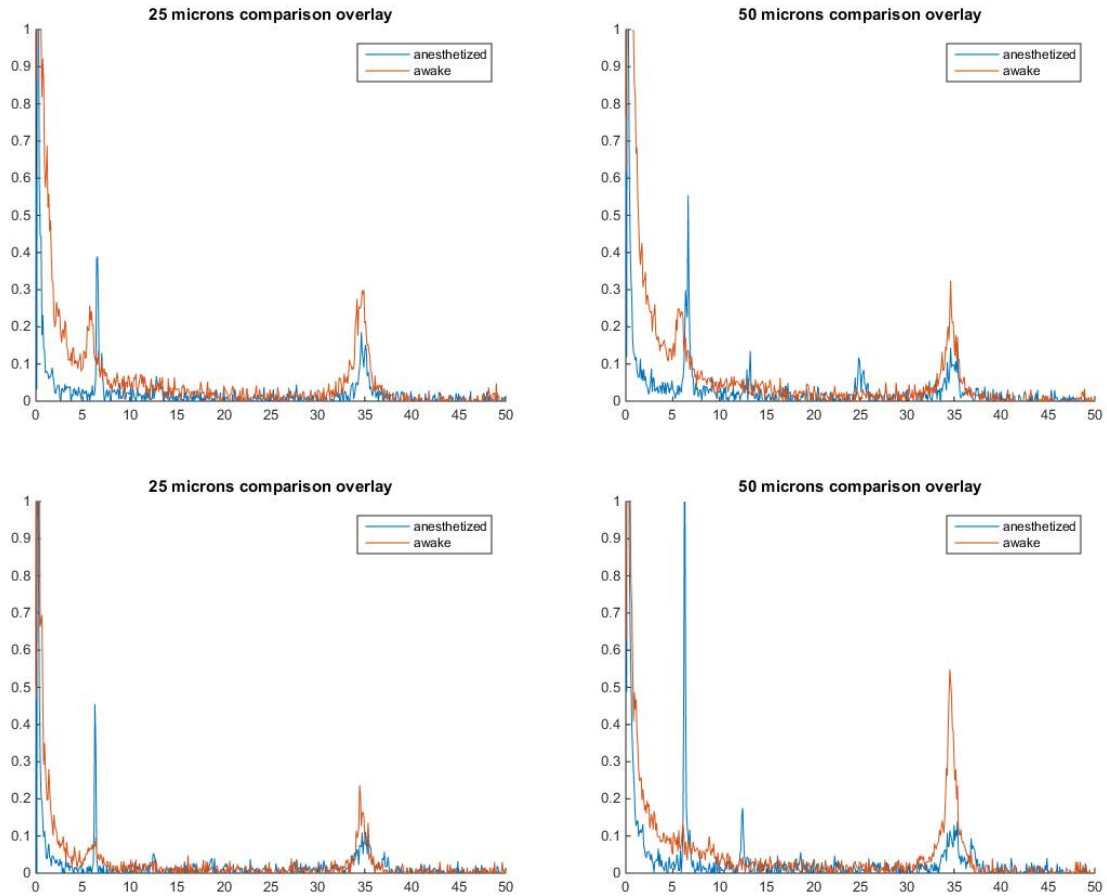
Supplemental figure 3.2 Average spectra of each mouse for 75 and 100 μm cortical depth. Red shows awake recording, and blue shows the anesthetized recording from the same session. Each graph is paired 75 and 100 μm from the same recording session.
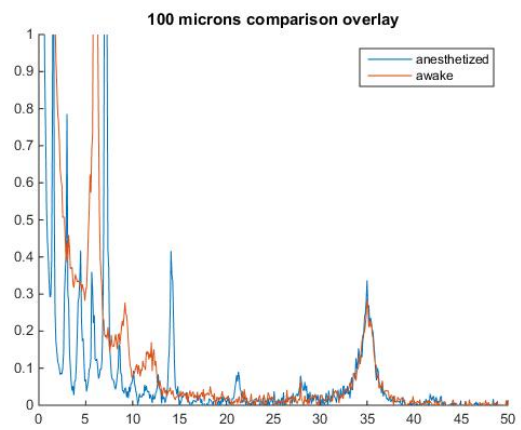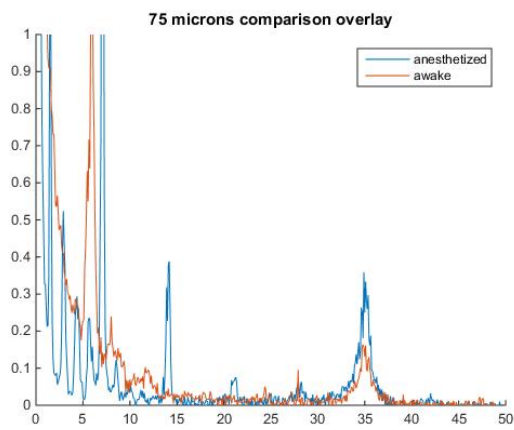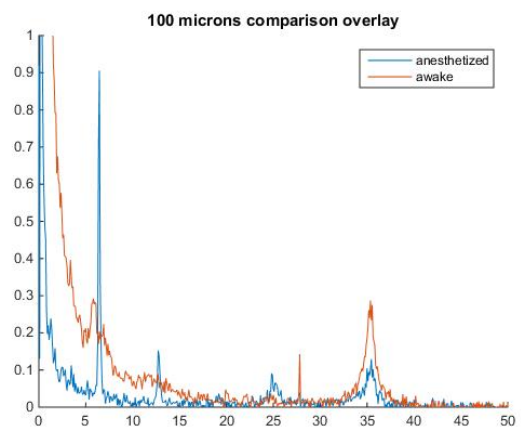
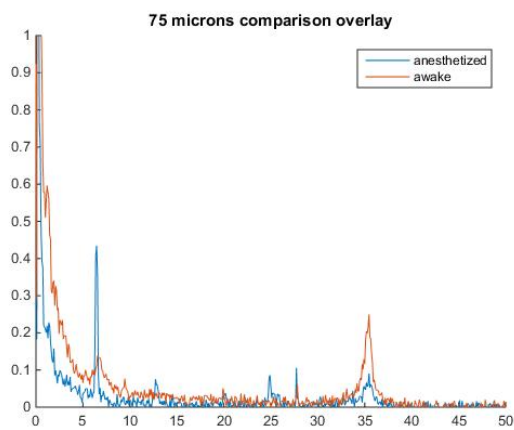75 microns comparison overlay

100 microns comparison overlay

75 microns comparison overlay

100 microns comparison overlay
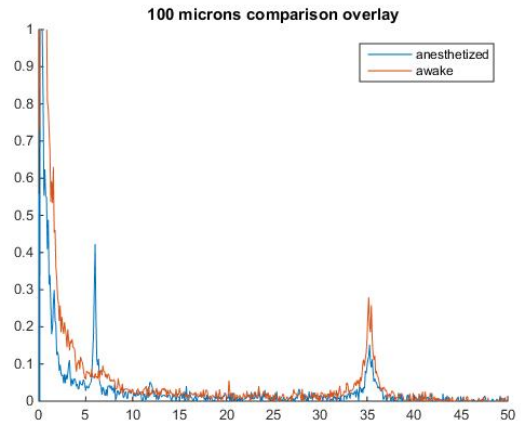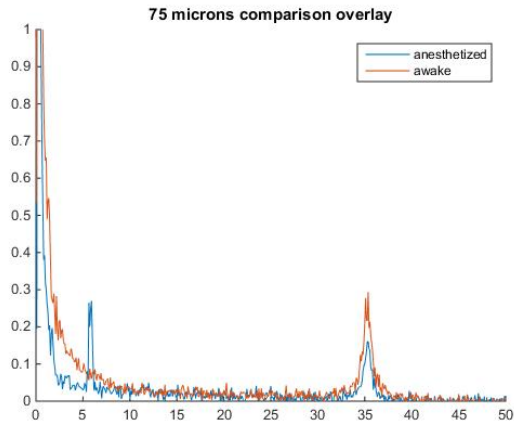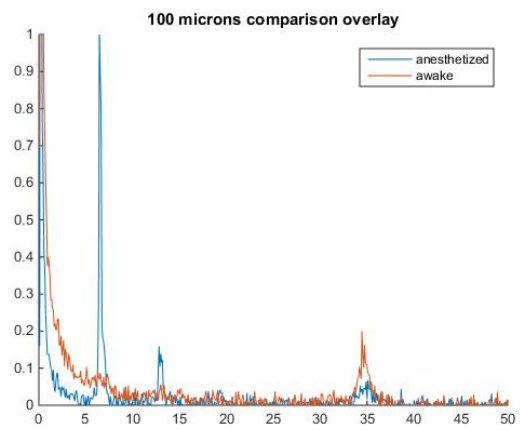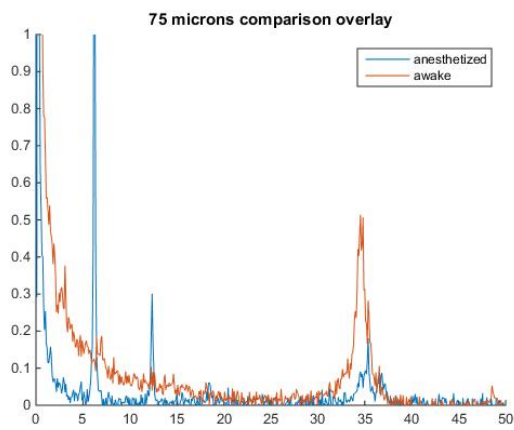
Chapter 4

General Discussion

Together these data show how the upper cortical layers are active and responsive to sensory stimuli. Neural oscillations are present all the way up to 25μm below the dura, and include a strong gamma peak. Gamma is shown to be responsive to sensory stimuli, as previously demonstrated, but delta and theta also show changes. Light anesthesia dampens many of these oscillations, except for a theta peak which gets markedly higher. When taken in the highest care possible, some oscillations increase power with cortical depth (delta, theta), while others show less depth preference (beta, gamma). Stimulation by whisker deflection produces a large depolarization, with bi-phasic peaks when recording voltage. The calcium activity associated with NMDA receptor activation however is almost entirely gone during anesthesia, suggesting that afferents from the PoM are no longer delivering top-down input. Depth changes these responses slightly, by increasing calcium change after leaving layer 1. Voltage on the 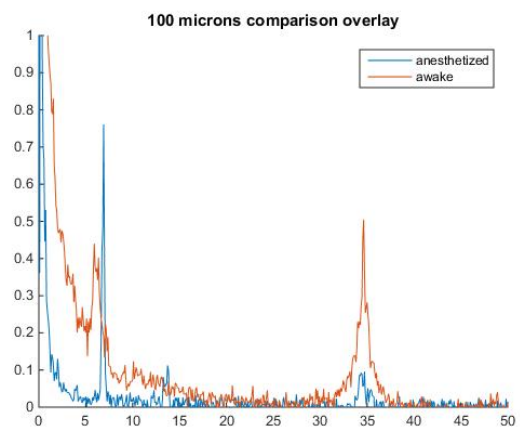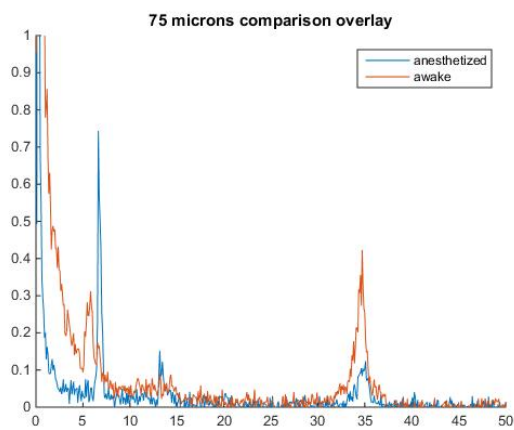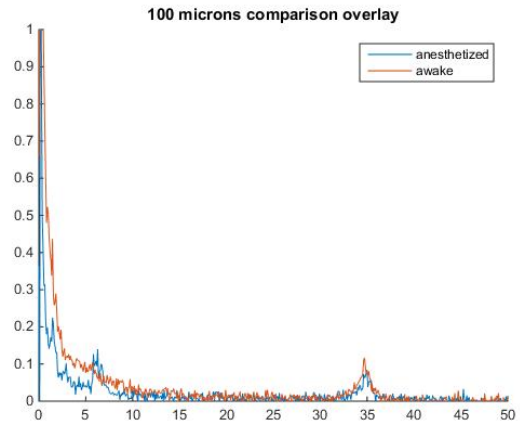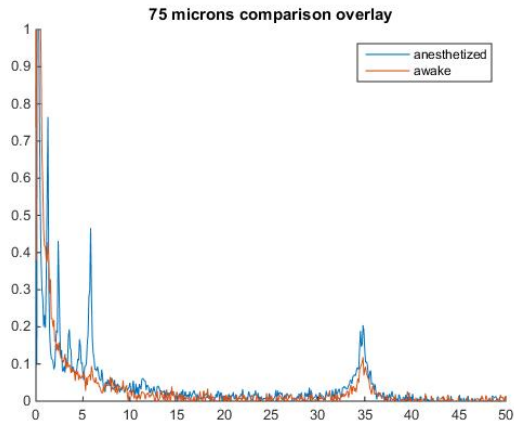other hand shows an increase between the first and second half of layer 1, similar to where gamma oscillations also show and increase in power.

Separation of top-down/bottom-up processing

Top-down and bottom-up processing can be separated functionally, but also to an extent anatomically. Signals coming directly to barrel cortex from the POm carry more top-down information, while VPM inputs carry bottom-up information. Comparing the recorded VSD responses to whisker stimulation with the bi-phasic peak, to previous work with somatosensory touch recorded with LFPs (Cauller, 1995) there are some notable similarities. The N1 and P1 touch responses appear in similar times to the early and late peaks in the VSD recording. N1 arrives first and is graded by the stimulation strength, but is not affected by attention or habituation. P1 on the other hand is graded by these properties, and less by the strength of stimulation. This suggests P1 is a representation of top-down processing and N1 is created from bottom-up processing. The VSD recordings show a slow response that corresponds very well with the timescale of GCaMP6f in the same area, suggesting it is produced simultaneously. GCaMP6f activity is detected when there is simultaneous input between layer 1 and deeper areas, in the specific cells I recorded, with the layer 1 input being mainly from POm (Zhang and Bruno, 2019). POm is also believed to be involved in top-

down processing, and thus the P1 response. The GCaMP6f signal reliant on the POm lines up with the late response recorded in the VSD, suggesting the late VSD response shows a top-down signal, just like P1. The early VSD response has no calcium component, and the response time is similar to the N1 component of LFP recordings (Cauller, 1995). One difference between N1 and the early VSD response however is the VSD early response is significantly larger while the animal is awake, than anesthetized. This suggests some grading of the early response due to cortical state, or in other words, some top-down information is encoded in the early VSD response. Due to its short latency, the triggering of depolarization leading to the early VSD response must arise from a direct pathway of excitation. In this way, it cannot be graded by many neighboring cortical areas, and so is still most encoding bottom-up information.

Considering the detected oscillations, and their changes due to cortical state, it is attractive to also bundle these changes into changes mediated by POm fibres coming into layer 1, however that would ignore a large number of other potential factors that can also explain the changes I recorded. Neuromodulators in general (of which acetyl-choline, which is acting to reduce POm activity) are generally quite affected by anesthesia and sleep, and several of them have also been tied to changing oscillation strengths. Particularly, dopamine, serotonin, and acetyl-choline work on the thalamus and change the regulation of calcium dynamics from wakefulness and sleep (Lőrincz and Adamantidis, 2017). These changes in calcium currents results in altered excitability in thalamic cells, and induces an increase in slow oscillations (delta and slow wave, i.e. below delta). Although I detect higher delta during wakefulness – possibly as anesthesia under isoflurane and sleep only share some similarities – some neuromodulator action acting on bodies outside the POm may be responsible.

Discussion of Detected Oscillations

Oscillation peaks are occurring where the recorded membrane voltage is synchronized enough that a peak forms above the baseline activity. In data recorded here, whisker stimulation increases gamma, theta, and delta power more in awake cases than anesthetized, despite the voltage change in both being very similar (potentially overall change is even smaller while awake). These seem at odds with each other, as increasing voltage change should mean more cells are recruited into a depolarization, measured by extracellular voltage

dye, which should increase synchronization. The only increase in voltage seen during stimulation, under awake conditions is the early peak response, so it might be that this component of the cortical response is the one responsible for increasing gamma power, and potentially the other frequency bands as well. An alternate view is that inhibitory neurons are more active during wakefulness, sharpening the cortical response. This might increase synchronization in other, deeper areas, without affecting the recorded voltage response, but in doing so, increase certain oscillation synchronies. One further explanation is that calcium influx from NMDA channels has some role in modulating neural oscillations, as this was present during wakefulness but not anesthesia.

Sensory activity in awake animals has been investigated before (Haider et al., 2013), showing that inhibitory activity dominates during wakefulness, and that these help to sharpen the sensory responses (Wehr and Zador, 2003; Isaacson and Scanziani, 2011; Liu et al., 2011), as well as increase the robustness of the sensory response (Egger et al., 2015). In the work by Egger et al, (2015), they looked at layer 1 inhibitory cells connecting to layer 2/3 pyramidal cell dendritic tufts. Inhibiting the layer 1 inhibitory cells increased the variability in sensory responses, so would also likely effect the synchronization of local neurons. It is possible that this could be leading to the increases I recorded in the oscillatory activity, even though the layer 1 interneurons are not fast-spiking parvalbumin expressing. Inhibition is tightly tied to oscillations (Bartos et al., 2007; Sohal, 2012), and these oscillations are increasing in wakefulness, and sensory response (especially gamma). The question then is whether this increase is due to inhibitory activity increasing, and whether it is tied to the sensory response sharpening (which may also explain the change in how the voltage response looks in Fig. 2.2).

Looking at the current theory of layer 1 as an integration area (Larkum, 2013), with top-down input into distal dendritic tufts coordinating binding of information into pyramidal neurons, and gamma as a mediator of communication through coherence (Fries, 2005; Bastos et al., 2015; Dumont et al., 2017; Dumont and Gutkin, 2018), it is natural to speculate about the nature of the gamma detected in my data set. Especially as there was an increase in power of delta, theta, and lower beta bands with cortical depth, but not gamma. Increasing power with depth was the expected result of optical voltage recordings in layer 1 (Kuhn et al., 2008), as

anatomy shows a lot of branching, (Cauller et al., 1998; Porrero et al., 2009; Narayanan et al., 2015). More diverse processes should carry more different information. Thus, the power of oscillations should decrease closer to the brain surface as signals de-correlate. As gamma does not follow this trend, it suggests gamma is more coherent through layer 1 than expected, especially compared with other detected neural oscillations. Whether this is enhancing specific communications and integration of top-down inputs however is at this point only speculation.

Looking for the origin of gamma in layer 1 is also important to consider. If multiple deeper neural populations project into layer 1 and are experiencing coherent gamma oscillations, it tells us that a large local circuit exists and is coherent. There is a chance however that gamma is generated, in some part, in layer 1. Surveys of interneurons within cortex show no fast-spiking cells originating in layer 1 (Packer and Yuste, 2011; Jiang et al., 2015), however basket cells do appear to project axons into layer 1. Basket cells connect mainly to local neurons, however when they project further from their local network, they tend to project upwards (Packer and Yuste, 2011). Peri-somatic connections between basket cells and pyramidal cells are thought to be key for the generation of gamma (Buzsáki and Wang, 2012) and perhaps enough basket cells are projecting onto the primary dendrites of layer 2/3 pyramidal cells within layer 1 for me to detect a gamma peak. Pyramidal cells of layer 5 and 6 also project into layer 1, and experience gamma oscillations, but there is no current anatomical evidence that basket cells in the supragranular layers connect to them in any strong fashion. This could imply that the gamma oscillation peak presented here is mainly from layer 2/3 cells, with dendrites from layers 5 and 6 contributing to noise. This would raise the effective dendritic voltage of gamma oscillations (table 3.1), as a smaller proportion of dendrites would be contributing to the detected signals. Another possibility is that each layer of pyramidal cells and local interneurons have their own oscillation. These local circuits then compete to couple other layers when communication between them is required. This could explain how oscillation power, including gamma power, increase in layer 1 following whisker stimulation (table 2.1). Previous research has suggested each cortical layer works as a local oscillator, however the frequency of oscillation recorded was 25 Hz, rather than 35 Hz, as recorded here (Bai et al., 2006). The final interpretation is that all pyramidal cells in the local area have coherent gamma oscillations, in part entrained by basket cells projecting

into layer 1. Determining the correct hypothesis is not answerable given the current data set, but can be a topic of further research, given the developments in oscillation detection put forward here.

Future Directions

To follow this work, ideally more oscillation data will be recorded with two-photon microscopy and voltage dyes. More data into how these oscillations change with sensory inputs, but also interactions between regions would be very interesting.

Recording oscillations beyond 40 Hz with VSDs and two-photon microscopy should be possible, given that the temporal resolution of our microscope is 1 kHz. The noise level reached such a point however that signals beyond the 40 Hz point did not stand out. Improvements in collection, such as using a random-access microscope to lower mechanical noise, and select scanning points to increase the biological signal (Shafeghat et al., 2016) might let researchers record higher gamma oscillations *in vivo.* Using a larger numerical aperture lens, or higher magnification may also isolate the smaller local oscillations like high-gamma and boost their signal above the noise level.

In the course of my research, I attempted to gather gamma oscillation recordings using a wider lens, still rated for two-photon excitation. Unfortunately I could not achieve the resolution required to measure gamma over the 1mm scale of the scan, however with more time and calibration, this could be done. Finding the spatial scope of oscillations, and particularly gamma, within the cortex, and how it alters with state and sensory input, is a vital step in the communication through coherence theory (Fries, 2005; Bastos et al., 2015). Gamma is thought to be the local synchronizing code, so cortical areas performing tasks that require communication, should then synchronize oscillations, and particularly gamma, if communication through coherence is correct.

Top-down processing is believed to be carried through layer 1 of the cortex, which can now be probed. Through this I hoped to record top-down activity related to habituation and surprise, but I could not find a robust enough means to generate these signals. Given more time though, this should be achievable, so recording top-down signals in layer 1, and their origin is a goal for the future.

Final Remarks

These data have demonstrated that layer 1 physiology can be measured and examined. Sensory responses can be collected, and oscillations detected, leaving the path open for much more research. A lot of the techniques used were rarely used before, or entirely novel. Through this work, they will now be more firmly established.

This data also presents novel findings, especially in layer 1 oscillations. Although most signals increase with cortical depth, gamma does not, and thus suggests the spread of gamma within a local cortical area is much more coherent than perhaps previously thought. The best explanation for gamma being so strong, so far away from cell bodies and fast-spiking interneurons, within tightly-packed dendrites projecting from many areas, is that the gamma oscillations in all the dendrites present are coherent. If this is the case, it strongly supports the communication through coherence theory (Fries, 2005; Bastos et al., 2015).

References

Acker CD, Hoyos E, Loew LM (2016) EPSPs Measured in Proximal Dendritic Spines of Cortical Pyramidal Neurons. eNeuro 3:ENEURO.0050-0015.2016.

Akemann W, Mutoh H, Perron A, Park YK, Iwamoto Y, Knöpfel T (2012) Imaging neural circuit dynamics with a voltage-sensitive fluorescent protein. Journal of Neurophysiology 108:2323-2337.

Antic SD, Empson RM, Knöpfel T (2016) Voltage imaging to understand connections and functions of neuronal circuits. Journal of Neurophysiology 116:135-152.

Au - Golshani P, Au - Portera-Cailliau C (2008) In Vivo 2-Photon Calcium Imaging in Layer 2/3 of Mice. JoVE:e681.

Bai L, Huang X, Yang Q, Wu J-Y (2006) Spatiotemporal patterns of an evoked network oscillation in neocortical slices: coupled local oscillators. Journal of neurophysiology 96:2528-2538.

Bao W, Wu J-Y (2003) Propagating wave and irregular dynamics: spatiotemporal patterns of cholinergic theta oscillations in neocortex in vitro. Journal of neurophysiology 90:333-341.

Bartos M, Vida I, Jonas P (2007) Synaptic mechanisms of synchronized gamma oscillations in inhibitory interneuron networks. Nature Reviews Neuroscience 8:45.

Bastos AM, Vezoli J, Fries P (2015) Communication through coherence with inter-areal delays. Current Opinion in Neurobiology 31:173-180.

Berger T, Borgdorff A, Crochet S, Neubauer FB, Lefort S, Fauvet B, Ferezou I, Carleton A, Luscher HR, Petersen CC (2007) Combined voltage and calcium epifluorescence imaging in vitro and in vivo reveals subthreshold and suprathreshold dynamics of mouse barrel cortex. J Neurophysiol 97:3751-3762.

Bieler M, Xu X, Marquardt A, Hanganu-Opatz IL (2018) Multisensory integration in rodent tactile but not visual thalamus. Scientific Reports 8:15684.

Braitenberg V, Schüz A (1998) Cortex: Statistics and Geometry of Neuronal Connectivity, 2 Edition: Springer-Verlag Berlin Heidelberg.

Bruno RM, Sakmann B (2006) Cortex Is Driven by Weak but Synchronously Active Thalamocortical Synapses. Science 312:1622.

Buhl EH, Tamás G, Fisahn A (1998) Cholinergic activation and tonic excitation induce persistent gamma oscillations in mouse somatosensory cortex in vitro. The Journal of Physiology 513:117-126.

Buzsáki G (2009) Rhythms of The Brain. In, pp xiv, 448 p.

Buzsáki G, Draguhn A (2004) Neuronal Oscillations in Cortical Networks. Science 304:1926.

Buzsáki G, Wang X-J (2012) Mechanisms of Gamma Oscillations. Annual Review of Neuroscience 35:203-225.

Casas-Torremocha D, Porrero C, Rodriguez-Moreno J, García-Amado M, Lübke JHR, Núñez Á, Clascá F (2019) Posterior thalamic nucleus axon terminals have different structure and functional impact in the motor and somatosensory vibrissal cortices. Brain Structure and Function.

Cauller L (1995) Layer I of primary sensory neocortex: Where top-down converges upon bottom-up. Behavioural Brain Research 71:163-170.

Cauller LJ, Kulics AT (1988) A comparison of awake and sleeping cortical states by analysis of the somatosensory-evoked response of postcentral area 1 in rhesus monkey. Exp Brain Res 72:584-592.

Cauller LJ, Clancy B, Connors BW (1998) Backward cortical projections to primary somatosensory cortex in rats extend long horizontal axons in layer I. J Comp Neurol 390:297-310.

Clascá F, Rubio-Garrido P, Jabaudon D (2012) Unveiling the diversity of thalamocortical neuron subtypes. European Journal of Neuroscience 35:1524-1532.

Bibliography

Cohen LB, Salzberg BM, Davila HV, Ross WN, Landowne D, Waggoner AS, Wang CH (1974) Changes in axon fluorescence during activity: molecular probes of membrane potential. J Membr Biol 19:1-36.

Constantinople CM, Bruno RM (2013) Deep cortical layers are activated directly by thalamus. Science 340:1591-1594.

da Costa NM, Martin KA (2010) Whose Cortical Column Would that Be? Front Neuroanat 4:16.

Deneux T, Grinvald A (2016) Milliseconds of Sensory Input Abruptly Modulate the Dynamics of Cortical States for Seconds. Cerebral Cortex 27:4549-4563.

Denk W, Strickler JH, Webb WW (1990) Two-photon laser scanning fluorescence microscopy. Science 248:73-76.

Derdikman D, Hildesheim R, Ahissar E, Arieli A, Grinvald A (2003) Imaging Spatiotemporal Dynamics of Surround Inhibition in the Barrels Somatosensory Cortex. The Journal of Neuroscience 23:3100.

Diamond ME, von Heimendahl M, Knutsen PM, Kleinfeld D, Ahissar E (2008) 'Where' and 'what'; in the whisker sensorimotor system. Nature Reviews Neuroscience 9:601.

Douglas RJ, Martin KAC, Whitteridge D (1989) A Canonical Microcircuit for Neocortex. Neural Computation 1:480-488.

Dumont G, Gutkin B (2018) Macroscopic phase resetting-curves determine oscillatory coherence and signal transfer in inter-coupled neural circuits. eprint arXiv:181203455:arXiv:1812.03455.

Dumont G, Ermentrout GB, Gutkin B (2017) Macroscopic phase-resetting curves for spiking neural networks. Physical Review E 96:042311.

Egger R, Schmitt AC, Wallace DJ, Sakmann B, Oberlaender M, Kerr JND (2015) Robustness of sensory-evoked excitation is increased by inhibitory inputs to distal apical tuft dendrites. Proceedings of the National Academy of Sciences 112:14072.

Elston GN (2003) Cortex, Cognition and the Cell: New Insights into the Pyramidal Neuron and Prefrontal Function. Cerebral Cortex 13:1124-1138.

Fox K (2008) Barrel Cortex: Cambridge University Press.

Fries P (2005) A mechanism for cognitive dynamics: neuronal communication through neuronal coherence. Trends in Cognitive Sciences 9:474-480.

Fromherz P, Hubener G, Kuhn B, Hinner MJ (2008) ANNINE-6plus, a voltage-sensitive dye with good solubility, strong membrane binding and high sensitivity. Eur Biophys J 37:509-514.

Gabbott PL, Somogyi P (1986) Quantitative distribution of GABA-immunoreactive neurons in the visual cortex (area 17) of the cat. Exp Brain Res 61:323-331.

Grinvald A, Hildesheim R (2004) VSDI: a new era in functional imaging of cortical dynamics. Nat Rev Neurosci 5:874-885.

Grinvald A, Manker A, Segal M (1982) Visualization of the spread of electrical activity in rat hippocampal slices by voltage-sensitive optical probes. J Physiol 333:269-291.

Haider B, Hausser M, Carandini M (2013) Inhibition dominates sensory responses in the awake cortex. Nature 493:97-100.

Hanslick JL, Lau K, Noguchi KK, Olney JW, Zorumski CF, Mennerick S, Farber NB (2009) Dimethyl sulfoxide (DMSO) produces widespread apoptosis in the developing central nervous system. Neurobiology of Disease 34:1-10.

Helmchen F, Svoboda K, Denk W, Tank DW (1999) In vivo dendritic calcium dynamics in deep-layer cortical pyramidal neurons. Nature Neuroscience 2:989-996.

Herkenham M (1980) Laminar organization of thalamic projections to the rat neocortex. Science 207:532-535.

Bibliography

Holtmaat A, Bonhoeffer T, Chow DK, Chuckowree J, De Paola V, Hofer SB, Hubener M, Keck T, Knott G, Lee WC, Mostany R, Mrsic-Flogel TD, Nedivi E, Portera-Cailliau C, Svoboda K, Trachtenberg JT, Wilbrecht L (2009) Long-term, high-resolution imaging in the mouse neocortex through a chronic cranial window. Nature protocols 4:1128-1144.

Hübener G, Lambacher A, Fromherz P (2003) Anellated Hemicyanine Dyes with Large Symmetrical Solvatochromism of Absorption and Fluorescence. The Journal of Physical Chemistry B 107:7896-7902.

Ibrahim Leena A, Mesik L, Ji X-y, Fang Q, Li H-f, Li Y-t, Zingg B, Zhang Li I, Tao Huizhong W (2016) Cross-Modality Sharpening of Visual Cortical Processing through Layer-1-Mediated Inhibition and Disinhibition. Neuron 89:1031-1045.

Iijima T, Witter MP, Ichikawa M, Tominaga T, Kajiwara R, Matsumoto G (1996) Entorhinal-Hippocampal Interactions Revealed by Real-Time Imaging. Science 272:1176.

Isaacson Jeffry S, Scanziani M (2011) How Inhibition Shapes Cortical Activity. Neuron 72:231-243.

Jiang X, Wang G, Lee AJ, Stornetta RL, Zhu JJ (2013) The organization of two new cortical interneuronal circuits. Nature Neuroscience 16:210.

Jiang X, Shen S, Cadwell CR, Berens P, Sinz F, Ecker AS, Patel S, Tolias AS (2015) Principles of connectivity among morphologically defined cell types in adult neocortex. Science 350:aac9462.

Jin W, Zhang R-J, Wu J-y (2002) Voltage-sensitive dye imaging of population neuronal activity in cortical tissue. Journal of Neuroscience Methods 115:13-27.

Jouhanneau J-S, Kremkow J, Dorrn Anja L, Poulet James FA (2015) In Vivo Monosynaptic Excitatory Transmission between Layer 2 Cortical Pyramidal Neurons. Cell Reports 13:2098-2106.

Kajiwara R, Tominaga T, Takashima I (2007) Olfactory information converges in the amygdaloid cortex via the piriform and entorhinal cortices: observations in the guinea pig isolated whole-brain preparation. European Journal of Neuroscience 25:3648-3658.

Kajiwara R, Tominaga Y, Tominaga T (2019) Network Plasticity Involved in the Spread of Neural Activity Within the Rhinal Cortices as Revealed by Voltage-Sensitive Dye Imaging in Mouse Brain Slices. Frontiers in Cellular Neuroscience 13:20.

Kleinfeld D, Delaney KR (1996) Distributed representation of vibrissa movement in the upper layers of somatosensory cortex revealed with voltage-sensitive dyes. J Comp Neurol 375:89-108.

Konnerth A, Orkand RK (1986) Voltage-sensitive dyes measure potential changes in axons and glia of the frog optic nerve. Neurosci Lett 66:49-54.

Kublik E, Musiał P, Wróbel A (2001) Identification of principal components in cortical evoked potentials by brief surface cooling. Clinical Neurophysiology 112:1720-1725.

Kuhn B, Fromherz P (2003) Anellated hemicyanine dyes in a neuron membrane: Molecular Stark effect and optical voltage recording. Journal of Physical Chemistry B 107:7903-7913.

Kuhn B, Fromherz P, Denk W (2004) High sensitivity of Stark-shift voltage-sensing dyes by one- or two-photon excitation near the red spectral edge. Biophys J 87:631-639.

Kuhn B, Denk W, Bruno RM (2008) In vivo two-photon voltage-sensitive dye imaging reveals top-down control of cortical layers 1 and 2 during wakefulness. Proc Natl Acad Sci U S A 105:7588-7593.

Lacefield CO, Pnevmatikakis EA, Paninski L, Bruno RM (2019) Reinforcement Learning Recruits Somata and Apical Dendrites across Layers of Primary Sensory Cortex. Cell Reports 26:2000-2008.e2002.

Lam Y-W, Cohen LB, Wachowiak M, Zochowski MR (2000) Odors Elicit Three Different Oscillations in the Turtle Olfactory Bulb. The Journal of Neuroscience 20:749.

Larkum M (2013) A cellular mechanism for cortical associations: an organizing principle for the cerebral cortex. Trends in Neurosciences 36:141-151.

Bibliography

Larkum ME, Senn W, Luscher HR (2004) Top-down dendritic input increases the gain of layer 5 pyramidal neurons. Cereb Cortex 14:1059-1070.

Larkum ME, Nevian T, Sandler M, Polsky A, Schiller J (2009) Synaptic Integration in Tuft Dendrites of Layer 5 Pyramidal Neurons: A New Unifying Principle. Science 325:756.

Lev-Ram V, Grinvald A (1986) Ca2+- and K+-dependent communication between central nervous system myelinated axons and oligodendrocytes revealed by voltage-sensitive dyes. Proceedings of the National Academy of Sciences of the United States of America 83:6651-6655.

Leznik E, Makarenko V, Llinás R (2002) Electrotonically Mediated Oscillatory Patterns in Neuronal Ensembles: An In Vitro Voltage-Dependent Dye-Imaging Study in the Inferior Olive. The Journal of Neuroscience 22:2804.

Lippert MT, Takagaki K, Xu W, Huang X, Wu J-Y (2007) Methods for Voltage-Sensitive Dye Imaging of Rat Cortical Activity With High Signal-to-Noise Ratio. Journal of Neurophysiology 98:502-512.

Liu B-h, Li Y-t, Ma W-p, Pan C-j, Zhang Li I, Tao Huizhong W (2011) Broad Inhibition Sharpens Orientation Selectivity by Expanding Input Dynamic Range in Mouse Simple Cells. Neuron 71:542-554.

Llinás RR, Leznik E, Urbano FJ (2002) Temporal binding via cortical coincidence detection of specific and nonspecific thalamocortical inputs: A voltage-dependent dye-imaging study in mouse brain slices. Proceedings of the National Academy of Sciences 99:449.

Lőrincz ML, Adamantidis AR (2017) Monoaminergic control of brain states and sensory processing: Existing knowledge and recent insights obtained with optogenetics. Progress in Neurobiology 151:237-253.

Lubke J, Feldmeyer D (2007) Excitatory signal flow and connectivity in a cortical column: focus on barrel cortex. Brain Struct Funct 212:3-17.

Masri R, Bezdudnaya T, Trageser JC, Keller A (2008) Encoding of Stimulus Frequency and Sensor Motion in the Posterior Medial Thalamic Nucleus. Journal of Neurophysiology 100:681-689.

Masri R, Trageser JC, Bezdudnaya T, Li Y, Keller A (2006) Cholinergic Regulation of the Posterior Medial Thalamic Nucleus. Journal of Neurophysiology 96:2265-2273.

Masri R, Quiton RL, Lucas JM, Murray PD, Thompson SM, Keller A (2009) Zona Incerta: A Role in Central Pain. Journal of Neurophysiology 102:181-191.

Mease RA, Metz M, Groh A (2016) Cortical Sensory Responses Are Enhanced by the Higher-Order Thalamus. Cell Reports 14:208-215.

Mennerick S, Chisari M, Shu H-J, Taylor A, Vasek M, Eisenman LN, Zorumski CF (2010) Diverse Voltage-Sensitive Dyes Modulate GABA_AReceptor Function. The Journal of Neuroscience 30:2871-2879.

Merker BH (2016) Cortical Gamma Oscillations: Details of Their Genesis Preclude a Role in Cognition. Frontiers in Computational Neuroscience 10.

Mohajerani MH, McVea DA, Fingas M, Murphy TH (2010) Mirrored Bilateral Slow-Wave Cortical Activity within Local Circuits Revealed by Fast Bihemispheric Voltage-Sensitive Dye Imaging in Anesthetized and Awake Mice. The Journal of Neuroscience 30:3745.

Musall S, Haiss F, Weber B, von der Behrens W (2015) Deviant Processing in the Primary Somatosensory Cortex. Cerebral Cortex 27:863-876.

Narayanan RT, Udvary D, Oberlaender M (2017) Cell Type-Specific Structural Organization of the Six Layers in Rat Barrel Cortex. Frontiers in Neuroanatomy 11.

Narayanan RT, Egger R, Johnson AS, Mansvelder HD, Sakmann B, de Kock CP, Oberlaender M (2015) Beyond Columnar Organization: Cell Type- and Target Layer-Specific Principles of Horizontal Axon Projection Patterns in Rat Vibrissal Cortex. Cereb Cortex.

Bibliography

Noudoost B, Chang MH, Steinmetz NA, Moore T (2010) Top-down control of visual attention. Current Opinion in Neurobiology 20:183-190.

Orbach HS, Cohen LB, Grinvald A (1985) Optical mapping of electrical activity in rat somatosensory and visual cortex. The Journal of neuroscience : the official journal of the Society for Neuroscience 5:1886-1895.

Packer AM, Yuste R (2011) Dense, Unspecific Connectivity of Neocortical Parvalbumin-Positive Interneurons: A Canonical Microcircuit for Inhibition? The Journal of Neuroscience 31:13260.

Pedroarena C, Llinás R (1997) Dendritic calcium conductances generate high-frequency oscillation in thalamocortical neurons. Proceedings of the National Academy of Sciences 94:724-728.

Penttonen M, Kamondi A, Acsády L, Buzsáki G (1998) Gamma frequency oscillation in the hippocampus of the rat: intracellular analysis in vivo. European Journal of Neuroscience 10:718-728.

Peterka DS, Takahashi H, Yuste R (2011) Imaging Voltage in Neurons. Neuron 69:9-21.

Petersen CC, Grinvald A, Sakmann B (2003) Spatiotemporal dynamics of sensory responses in layer 2/3 of rat barrel cortex measured in vivo by voltage-sensitive dye imaging combined with whole-cell voltage recordings and neuron reconstructions. The Journal of neuroscience : the official journal of the Society for Neuroscience 23:1298-1309.

Porrero C, Pérez-de-Manzo F, Clascá F, Galazo MJ, Rubio-Garrido P (2009) Thalamic Input to Distal Apical Dendrites in Neocortical Layer 1 Is Massive and Highly Convergent. Cerebral Cortex 19:2380-2395.

Roome CJ, Kuhn B (2014) Chronic cranial window with access port for repeated cellular manipulations, drug application, and electrophysiology. Front Cell Neurosci 8:379.

Roome CJ, Kuhn B (2018) Simultaneous dendritic voltage and calcium imaging and somatic recording from Purkinje neurons in awake mice. Nature Communications 9:3388.

Rubio-Garrido P, Perez-de-Manzo F, Porrero C, Galazo MJ, Clasca F (2009) Thalamic input to distal apical dendrites in neocortical layer 1 is massive and highly convergent. Cereb Cortex 19:2380-2395.

Rudy B, Fishell G, Lee S, Hjerling-Leffler J (2011) Three groups of interneurons account for nearly 100% of neocortical GABAergic neurons. Developmental Neurobiology 71:45-61.

Schiller J, Schiller Y (2001) NMDA receptor-mediated dendritic spikes and coincident signal amplification. Current Opinion in Neurobiology 11:343-348.

Schiller J, Schiller Y, Clapham DE (1998) NMDA receptors amplify calcium influx into dendritic spines during associative pre- and postsynaptic activation. Nature Neuroscience 1:114-118.

Schiller J, Major G, Koester HJ, Schiller Y (2000) NMDA spikes in basal dendrites of cortical pyramidal neurons. Nature 404:285-289.

Shafeghat N, Heidarinejad M, Murata N, Nakamura H, Inoue T (2016) Optical detection of neuron connectivity by random access two-photon microscopy. Journal of Neuroscience Methods 263:48-56.

Shepherd GM (2003) The Synaptic Organization of the Brain, 4th Edition: Oxford University Press. New York.

Sheroziya M, Timofeev I (2014) Global Intracellular Slow-Wave Dynamics of the Thalamocortical System. The Journal of Neuroscience 34:8875-8893.

Skinner FK, Kopell N, Marder E (1994) Mechanisms for oscillation and frequency control in reciprocally inhibitory model neural networks. Journal of Computational Neuroscience 1:69-87.

Sohal VS (2012) Insights into Cortical Oscillations Arising from Optogenetic Studies. Biological Psychiatry 71:1039-1045.

Bibliography

Stosiek C, Garaschuk O, Holthoff K, Konnerth A (2003) In vivo two-photon calcium imaging of neuronal networks. Proceedings of the National Academy of Sciences 100:7319.

Suh J, Rivest A, Nakashiba T, Tominaga T, Tonegawa S (2011) Entorhinal Cortex Layer III Input to the Hippocampus Is Crucial for Temporal Association Memory.

Sun W, Dan Y (2009) Layer-specific network oscillation and spatiotemporal receptive field in the visual cortex. Proceedings of the National Academy of Sciences 106:17986.

Takata N, Hirase H (2008) Cortical Layer 1 and Layer 2/3 Astrocytes Exhibit Distinct Calcium Dynamics In Vivo. PLOS ONE 3:e2525.

Tasaki I, Watanabe A, Sandlin R, Carnay L (1968) Changes in fluorescence, turbidity, and birefringence associated with nerve excitation. Proc Natl Acad Sci U S A 61:883-888.

Tominaga T, Tominaga Y, Yamada H, Matsumoto G, Ichikawa M (2000) Quantification of optical signals with electrophysiological signals in neural activities of Di-4-ANEPPS stained rat hippocampal slices. Journal of Neuroscience Methods 102:11-23.

Trageser JC, Burke KA, Masri R, Li Y, Sellers L, Keller A (2006) State-dependent gating of sensory inputs by zona incerta. J Neurophysiol 96:1456-1463.

Traub RD, Jefferys JGR, Whittington MA (1999) Fast oscillations in cortical circuits.

Tsvyetlynska NA, Hill RH, Grillner S (2005) Role of AMPA Receptor Desensitization and the Side Effects of a DMSO Vehicle on Reticulospinal EPSPs and Locomotor Activity. Journal of Neurophysiology 94:3951-3960.

Van Vreeswijk C, Abbott LF, Bard Ermentrout G (1994) When inhibition not excitation synchronizes neural firing. Journal of Computational Neuroscience 1:313-321.

Wehr M, Zador AM (2003) Balanced inhibition underlies tuning and sharpens spike timing in auditory cortex. Nature 426:442-446.

Williams V, Grossman RG, Edmunds SM (1980) Volume and surface area estimates of astrocytes in the sensorimotor cortex of the cat. Neuroscience 5:1151-1159.

Woolsey TA, Van der Loos H (1970) The structural organization of layer IV in the somatosensory region (S I) of mouse cerebral cortex: The description of a cortical field composed of discrete cytoarchitectonic units. Brain Research 17:205-242.

Wu J-y, Guan L, Tsau Y (1999) Propagating Activation during Oscillations and Evoked Responses in Neocortical Slices. The Journal of Neuroscience 19:5005.

Wu J-Y, Xiaoying H, Chuan Z (2007) Propagating Waves of Activity in the Neocortex: What They Are, What They Do. The Neuroscientist 14:487-502.

Yoshimura H, Sugai T, Kato N, Tominaga T, Tominaga Y, Hasegawa T, Yao C, Akamatsu T (2016) Interplay between non-NMDA and NMDA receptor activation during oscillatory wave propagation: Analyses of caffeine-induced oscillations in the visual cortex of rats. Neural Networks 79:141-149.

Zhang W, Bruno R (2019) High-order thalamic inputs to primary somatosensory cortex are stronger and longer lasting than cortical inputs.

Zochowski M, Wachowiak M, Falk CX, Cohen LB, Lam YW, Antic S, Zecevic D (2000) Imaging membrane potential with voltage-sensitive dyes. The Biological Bulletin 198:1-21.